NATIONAL TECHNICAL UNIVERSITY OF ATHENS

SCHOOL OF NAVAL ARCHITECTURE AND MARINE ENGINEERING

Andreas P. Kyriakongonas,

Dipl. Mechanical Engineer

A dissertation submitted for the

Degree of Master of Science in

Marine Science and Technology

"3D Numerical Modeling of Austenitic Stainless Steel 316L Multi-pass Butt Welding and Comparison with Experimental Results"

Supervisor

V. J. Papazoglou, Professor

to my parents for their love and support

Contents

Preface

Stainless steels are an important class of engineering materials that have been used widely in a variety of industries and environments. Welding is an important fabrication technique for stainless steels, and numerous specifications, handbooks, papers, and other guidelines have been published over the past 75 years that provide insight into the techniques and precautions needed to weld these materials successfully.

Being a thermo-mechanical process, welding can result into a number of mechanical effects, such as residual stresses and distortion, which are undesirable in welded constructions. In order to avoid such phenomena, many factors and parameters must be considered during the design process. The introduction of the Finite Element Method in the welding science, along with the continuous growth of Computer Science, was the onset of Computational Welding Mechanics (CWM). The usage of CMW during the design process of welded constructions provides the engineers predictive numerical models that save a lot of time and cost.

In this Master Thesis, the construction of a three-dimensional numerical model of austenitic stainless steel multi-pass butt welding is presented. The accuracy of the numerical model is discussed and evaluated. To evaluate the numerical model, experimental results from austenitic stainless steel multi-pass welding are presented and compared with the model's numerical results.

Acknowledgments

I would like to express my gratitude to Professor Vassilios J. Papazoglou for his trust and support at the whole time and his careful review of the Thesis. My special thanks go to Assistant Professor G.N. Labeas, of University of Patras, and Dipl. Mechanical Engineer G.A. Moraitis for their advice and assistance. I am also grateful to Stavros Chionopoulos for encouraging me to obtain the Master Degree.

3D Numerical Modeling of Austenitic Stainless Steel 316L Multi-pass Butt Welding and Comparison with Experimental Results

1st Chapter

Introduction to Stainless Steels

1. Introduction to Stainless Steels

Stainless steels are an important class of engineering metallic materials, which have been used widely in a variety of industries and environments. In addition, welding is an important fabrication technique for stainless steels. Numerous specifications, papers, handbooks and other guidelines have been published over the past 75 years that provide insight into the techniques and precautions needed to weld these metals successfully. Stainless steels are considered, in general, weldable metals, but there are many rules that must be followed to ensure that they can be readily fabricated and free of defects and that will perform in their service environment as expected. When the rules are not followed, problems are not uncommon during fabrication or in service. The problems that occur are often associated with improper control of the weld microstructure and other associated properties, or the use of welding procedures that are inappropriate for the metal and its microstructure.

Amongst the stainless steel grades, the austenitic ones represent a large variety of alloys and are the most widely used in service. Their implementation in high temperature environments, but also in cryogenic temperatures, distinguishes them from the other grades and makes them applicable in the petrochemical, shipping and other industries. This master thesis is written in order to study austenitic stainless steel grades, their weldability and their welding metallurgy. The thesis deals also with the mechanical effects, such as deflection and residual stresses, of the metal due to the welding process, by incorporating a numerical simulation model via finite element analysis and obtaining results that are compared with experimental measurements.

1.1 Definition of Stainless Steels

Stainless steels constitute a group of high-alloy steels based on the binary Fe-Cr and on the ternary Fe-Cr-C and Fe-Cr-Ni systems. In order a steel to be "stainless", it must contain a minimum amount of chromium. In the entire bibliography many numbers of the chromium's minimum weight percentage can be found that place it between 10.5 and 12 wt % [1]. This level of chromium allows the formation of a passive surface oxide that prevents oxidation and corrosion of the underlying metal under ambient, noncorrosive conditions.

The passive surface oxide does not provide complete and everlasting immunity to corrosion. Corrosive media can attack and remove the passive oxide causing corrosion of stainless steels. Corrosion can take many forms, including pitting, crevice corrosion and intergranural attack. These forms of corrosion are influenced by the corrosive environment, the metallurgical condition of the metal and the local stresses that are present, e.g. residual stresses. All the above indicate that engineers and designers must be very aware of the

service environments and the impact of fabrication practice on the metallurgical behavior when selecting stainless steels for use in corrosive conditions.

Stainless steels also have good resistance to oxidation, even at high temperatures, and they are often referred to as heat-resisting alloys. Resistance to elevated temperature oxidation is primarily a function of chromium content. Some high chromium stainless steel alloys (25 to 35 wt % Cr) can be used to temperatures as high as 1000 °C. Another form of resistance, at elevated temperatures, is resistance to carburization, for which stainless steel alloys of medium chromium content (about 16 wt %) but high nickel content (about 35 wt %) have been developed.

Stainless steels are used in a wide variety of applications, such as power generator, chemical and paper processing and in many commercial products, such as kitchen equipment and automobiles. Stainless steels also find extensive use for purity and sanitary applications in areas such as pharmaceutical, diary and food processing. At present excessive use of stainless steel is being observed in the shipbuilding industry, as well.

Most stainless steels are weldable, but many require special procedures. In almost all cases, welding results in a significant alteration of the weld metal and heat affected zone microstructure relative to the base metal. This can constitute a change in the desired phase balance, formation of intermetallic constituents, grain growth, segregation of alloy and impurity elements and other reactions. In general, these lead to some level of degradation of properties and performance and must be taken into account during the design and manufacture process.

1.2 History of Stainless Steel

The addition of chromium to steels and its apparent beneficial effect on corrosion resistance is generally attributed to Pierre Berthier, who in 1821 developed a 1.5 wt% Cr alloy that he recommended for cutlery applications. However, experiments with these steels revealed, that with increased Cr, the formability of the steel deteriorated dramatically, so interest in them waned until the early 20th century. We now can attribute this behavior to the high carbon content of these early alloys.

Interest in corrosion-resistant steels reemerged between 1900 and 1915 and a number of metallurgist are credited with developing corrosion-resistant alloys. The onset of this renewed activity was made in 1897 by Goldschmidt in Germany with the development of a technique for producing low-carbon Cr-bearing alloys. Shortly thereafter, Guillet, in 1904, Portevin and Giesen, in 1909, published papers describing the microstructure and properties of 13 wt% Cr martensitic and 17 wt% Cr ferritic stainless steels. In 1909, Guillet also published a study of chromium-nickel steels that were the precursors of the austenitic grades of stainless steels. Another

development that would boost the stainless steel production up was the introduction of the direct-arc electric furnace by Heroult in 1899.

All the above laboratory studies sparked considerable interest in corrosion-resistant steels for industrial applications and from 1910 to 1915 there was considerable effort to commercialize these alloys. The first reported commercial "stainless steel" alloys are attributed to Harry Brearly, who was a metallurgist at Thomas Firth & Sons in Sheffield, England. Brearly was investigating the failure of rifle gun barrels made of 5 wt% chromium and in August 1913, an acceptable ingot was cast of the following composition (wt%): 12.86% Cr, 0.24% C, 0.20% Si and 0.44% Mn. Out of this ingot, 12 experimental gun barrels were made, but did not show the expected improvement. Some of the ingot was used to produce cutlery blades and the age of stainless steel had begun.

The first stainless steel ingot was cast in the United States by Firth Sterling Ltd. in Pittsburg on March 3, 1915. This eventually led to a U.S. patent, assigned to Brearly for cutlery grade steel. It covered the composition range from 9 to 16 wt% chromium and less than 0.7 wt% carbon. Steels made under this patent soon came to be called Firth Stainless.

1.3 Types of Stainless Steel and their application

Stainless steels are the most widely used steels, next to plain carbon and C-Mn steels. This is due to the fact that there are so many varieties of stainless steels available offering a wide range of properties suitable for use in many applications.

Unlike other materials, where classification is usually by composition, stainless steel are categorized based on the metallurgical phase or phases, which is predominant. There are three phases possible in stainless steels. These three phases are martensite, ferrite and austenite. Stainless steels with two metallurgical phases are termed Duplex, containing approximately 50% ferrite and 50% austenite, taking advantage of the desirable properties of each phase. Precipitation-hardenable (PH) grades are termed such, because they form strengthening precipitates and are hardenable by an aging heat treatment. PH stainless steels are further grouped by the phase or matrix, in which the precipitates are formed, to martensitic, semi-austenitic or austenitic types.

The American Iron and Steel Institute (AISI) in order to designate stainless steels uses, a system with three numbers (Table 1.1), sometimes followed by a letter, for example, 304, 316, 316L, 410 [2].

Table 1.1 Types of Stainless Steels (AISI)

Martensitic	4XX
Ferritic	4XX
Austenitic	2XX, 3XX
Duplex	Austenite and Ferrite
Precipitation hardened	PH

In order to identify some stainless steels, magnetic properties can be used. The austenitic types are essentially nonmagnetic. A small amount of residual ferrite or cold working may introduce a slight ferromagnetic condition, but it is notably weaker than a magnetic material. The ferritic and martensitic types are ferromagnetic. Duplex stainless steels are relatively strongly magnetic due to their high ferrite content.

Physical properties, such as thermal conductivity, thermal expansion and mechanical properties vary widely for the different types and influence their welding characteristics. For example, austenitic stainless steels exhibit low thermal conductivity and high thermal expansion, resulting in higher distortion due to welding than other grades that are primarily ferritic or martensitic.

1.4 Corrosion Resistance

In most engineering applications, stainless steels are selected for their corrosion- or heat-resisting properties. By nature of the passive, Cr-rich oxide that forms on their surface, stainless steels are virtually immune to the general corrosion that plagues C-Mn and low-alloy structural steels. Stainless steels are, however, susceptible to other forms of corrosion and their selection and application must be considered carefully based on the service environment.

There are two forms of localized corrosion that may occur in stainless steels. These are pitting corrosion and crevice corrosion, which mechanistically are similar and result in highly localized attack.

As the term implies, pitting corrosion results from the local breakdown of the passive film and it is normally associated with some metallurgical feature, such as a grain boundary or intermetallic constituent. Once this breakdown takes place, corrosive attack of the underlying material occurs and a small pit forms on the surface. With time, the solution chemistry within the pit changes and becomes progressively more aggressive (i.e. acidic), which results in rapid subsurface attack and a linking of adjacent pits that ultimately leads to failure.

Crevice corrosion is similar mechanistically, but does not require the presence of a metallurgical feature to initiate. Rather, as the term implies, a crevice consisting of a confined space must exist where a similar change in solution chemistry can occur. Crevice corrosion is common in bolted structures, where the space between the bolt head and the bolting surface can provide such a crevice.

Both pitting and crevice corrosion occur readily in solutions containing chloride ions, such as seawater. Welding may result in the formation of microstructures that accelerate pitting attack or create crevices (lack of penetration, slag inclusions etc.) that promote localized corrosion. Failure to remove oxides that form due to welding procedures may also reduce corrosion resistance of stainless steels in certain media.

The most serious of all corrosion mechanism in welded stainless steels, and the subject of many papers and reviews [3] is *intergranular attack* (IGA) and the associated phenomenon known as *intergranular stress corrosion cracking* (IGSCC). This form of corrosion is common in the heat-affected zone (HAZ) of austenitic stainless steels and results from a metallurgical condition called *sensitization* [4]. Sensitization occurs when grain boundary precipitation of Cr-rich carbides result in depletion of Cr in the region just adjacent to the grain boundary, making the microstructure sensitive to corrosive attack if the Cr content drops below 12 wt%. A similar phenomenon occurs in the HAZ of ferritic stainless steels.

Transgranular stress corrosion cracking (TGSCC) is also a serious problem, especially with common austenitic stainless steels such as 304L and 316L. As the term implies, transgranular SCC has little or nothing to do with grain boundaries. It progresses along certain planes of atoms in each grain, often changing direction from one grain to another, branching as it progresses. The presence of chloride ions along with residual or applied stress promotes this form of cracking.

1.5   Phase Diagrams

The purpose of equilibrium phase diagrams is to describe phase transformations and phase stability in stainless steels. The phase diagrams that refer to stainless steels are the Fe-Cr binary system, and the Fe-Cr-C and Fe-Cr-Ni ternary systems. These diagrams can only approximate the actual microstructure that develops in the weld, for two reasons:

1st: stainless steel base and filler metals contain even up to 10 alloying elements, which can not be accommodated in one phase diagram.

2nd: phase diagrams are built based on equilibrium conditions, while the rapid heating and cooling conditions associated with welding, result in non-equilibrium conditions.

Some of the limitations of classical phase diagrams have been overcome by powerful computer programs, like ThermoCalc™, which use thermodynamic information in order to construct phase diagrams for alloy systems.

1.5.1 Iron-Chromium System

The iron-chromium phase diagram, presented in Figure 1.1, is the primary diagram to describe stainless steels, since chromium is the primary alloying element. It is important to note that there is complete solubility of Cr in iron at elevated temperatures and solidification of all Fe-Cr alloys occurs as ferrite. Ferrite is indicated in phase diagrams by the symbols α and δ, based on the Fe-C system, where δ-ferrite is considered high-temperature ferrite and α-ferrite is low temperature ferrite that forms from austenite.

At low chromium concentrations a "loop" of austenite exists in the temperature range 912 to 1394°C. This loop is known as the "*gamma loop*". Alloys with more than 12.7 wt% Cr will be fully ferritic at elevated temperatures, while alloys with less Cr will form at least some austenite within the gamma loop. Alloys with less than 12 wt% Cr will be completely austenitic and may transform austenite to martensite upon rapid cooling.
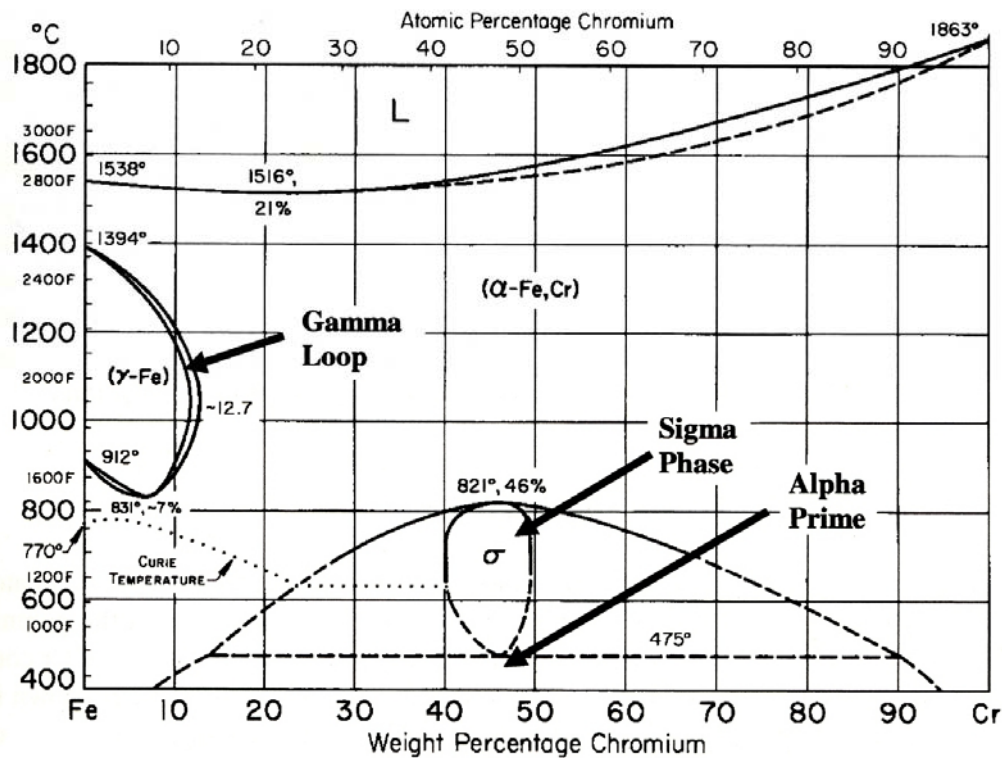
Figure 1.1 The Fe-Cr phase diagram [5]

In the Fe-Cr diagram, a low-temperature equilibrium phase, called sigma phase (σ), is also present, with (Fe,Cr) stoichiometry and a tetragonal crystal structure. This phase forms most readily in alloys exceeding 20 wt% Cr in their composition. Because sigma forms at low temperature, the kinetics, of formation, are quite sluggish and precipitation requires extended time in the temperature range 600 to 800°C. Sigma is a hard and brittle phase, hence its presence in stainless steels is usually undesirable.

In the Fe-Cr diagram, a dotted horizontal line can be seen within the σ+α phase field at the temperature of 475°C. This line designates a phenomenon called *475°C embrittlement*, resulting from the formation of coherent Cr-rich precipitates within the α-matrix. These precipitates are known as α' (alpha prime) and form within the temperature range 400 to 540°C. The presence of the above precipitates results in severe embrittling effect in alloys with higher than 14 wt% Cr [6]. The formation of α' can be also quite sluggish, but it can be accelerated with the addition of specific alloying elements.

1.5.2 Iron-Chromium-Carbon System

Adding carbon to the Fe-Cr system significantly alters the phase equilibrium, resulting in the Fe-Cr-C system. Carbon is an austenite-promoter and its addition will expand the gamma loop, allowing austenite to be stable at elevated temperatures and at much higher chromium contents. Even small amounts of carbon can dramatically expand the gamma loop. This can be observed in Figure 1.2, where the effect of carbon, mainly, and nitrogen on the gamma loop are shown.
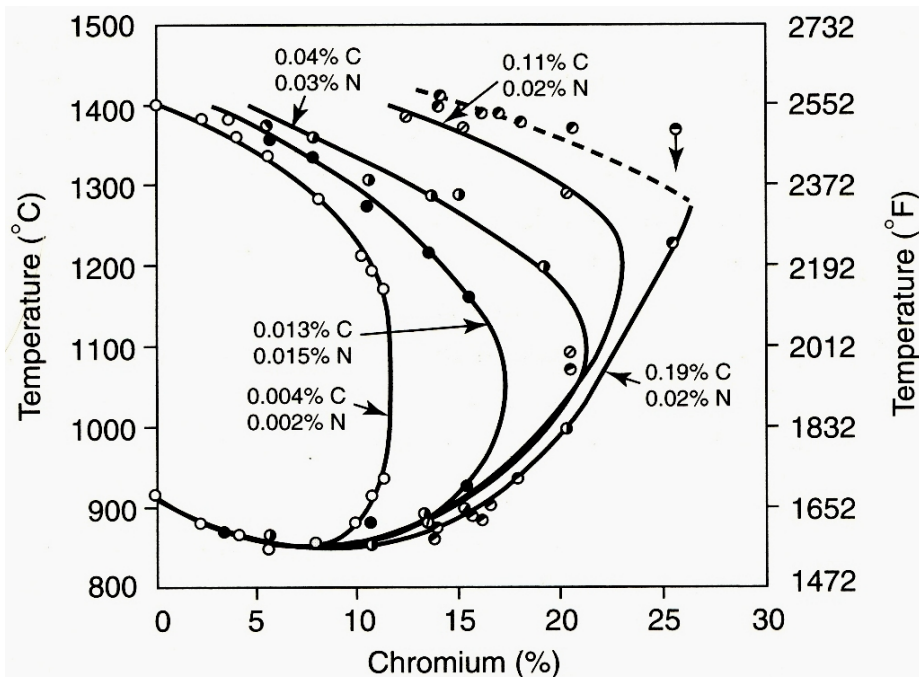
Figure 1.2 Effect of carbon on the expansion of austenite phase field

The importance of the austenite field expansion is significant for the martensitic grades, since austenite formed at elevated temperatures will transform to martensite upon cooling at ambient temperature. In addition, for the ferritic grades the size of the gamma loop must be controlled so that little or no austenite will form at elevated temperatures.

In order to view the Fe-Cr-C ternary system, as a function of temperature, it is necessary to set one of the elements content at a constant value. Thus, a *pseudobinary* diagram (or *isopleth*) is constructed, which represents a two-dimensional projection of a three-dimensional diagram. This kind of diagrams can not be used in the same manner as binary diagrams, but they are very useful in understanding phase equilibrium and phase transformation of the ternary systems. In Figure 1.3, two pseudo-binary diagrams are presented, based on 13 wt% and 17 wt% Cr with variable carbon content.
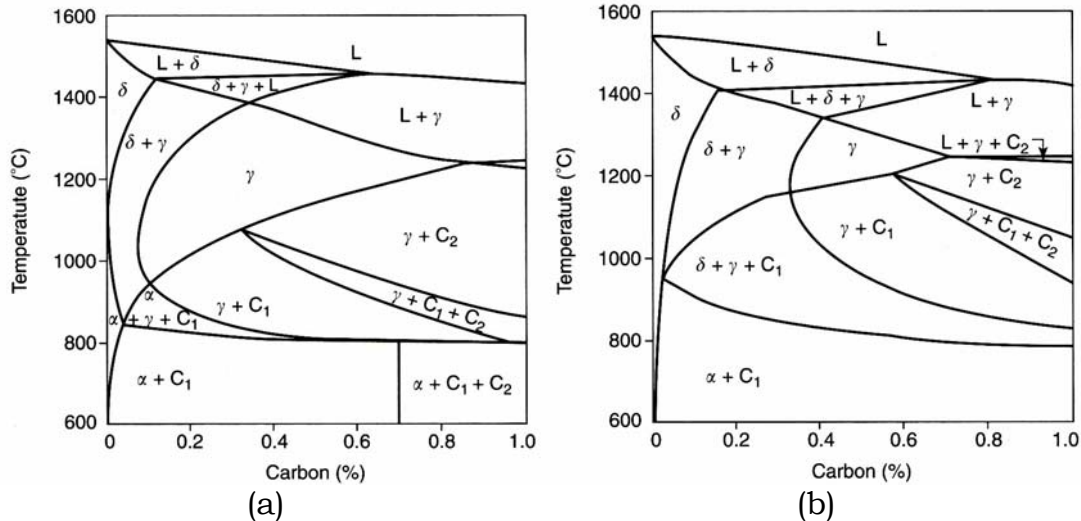
Figure 1.3 Fe-Cr-C pseudo-binary diagrams at a) 13% and b) 17% Cr [1]

In the above pseudo-binary diagrams, C_1 is a $(Cr,Fe)_{23}C_6$ carbide and C_2 a $(Cr,Fe)_7C_3$ carbide. The appearance of these two carbides is a result of the addition of carbon in the alloy which is also the reason for the increased complexity of the diagram in comparison with the Fe-Cr binary system.

1.5.3 Iron-Chromium-Nickel System

The addition of nickel to the Fe-Cr system also expands the gamma loop and promotes austenite, in such way that it can be a stable phase at ambient temperature. The ternary Fe-Cr-Ni system is the basis for the austenitic and duplex grades. The liquidus and solidus projections are shown in Figure 1.4 [5] and can be used to describe the solidification behavior of the alloys.
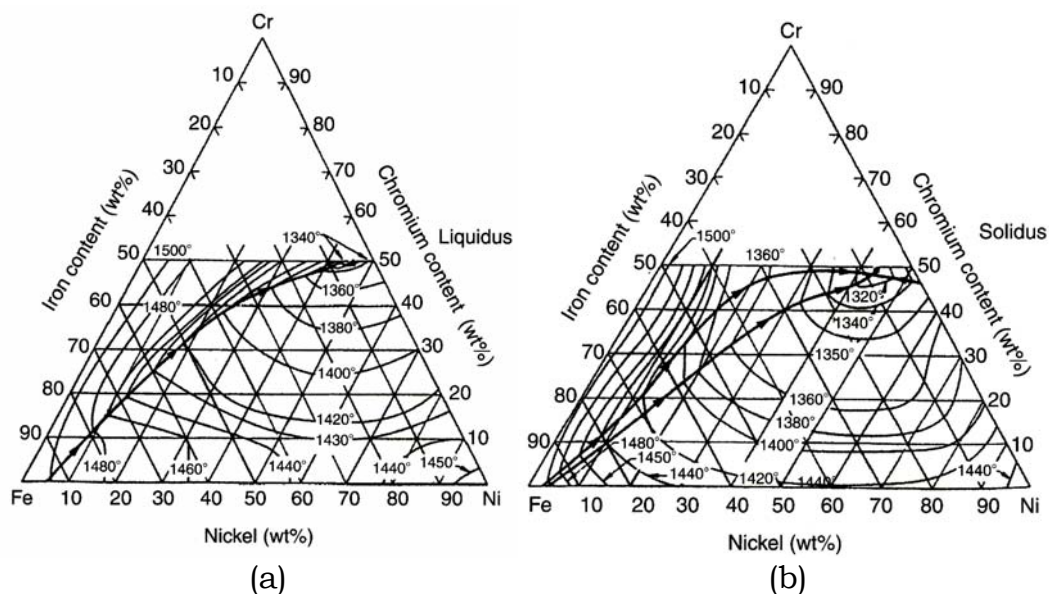
Figure 1.4 a)Liquidus and b)solidus projections of the Fe-Cr-Ni system [5]

9

In Figure 1.4 (a) on the liquidus surface, a dark line starting from the Fe-rich area and finishing at the Cr-Ni side, separates alloys that solidify as primary ferrite (on the left) and alloys that solidify as primary austenite (on the right). At approximately 48Cr-44Ni-8Fe a eutectic point exists.

The solidus surface exhibits two dark lines, which run from the Fe-rich apex to the Cr-Ni-rich side of the diagram. The arrows of the two dark lines point out the decrease of temperature. Between the two lines, and just above the solidus, austenite and ferrite coexist with liquid. Below the solidus, this region separates the ferrite and austenite single-phase fields. It is notable that these two lines terminate at the eutectic point.

By taking the Fe content constant, two pseudo-binary diagrams, at 70 and 60 wt% Fe, can be constructed [7] and presented both in Figure 1.5.

(a)   (b)
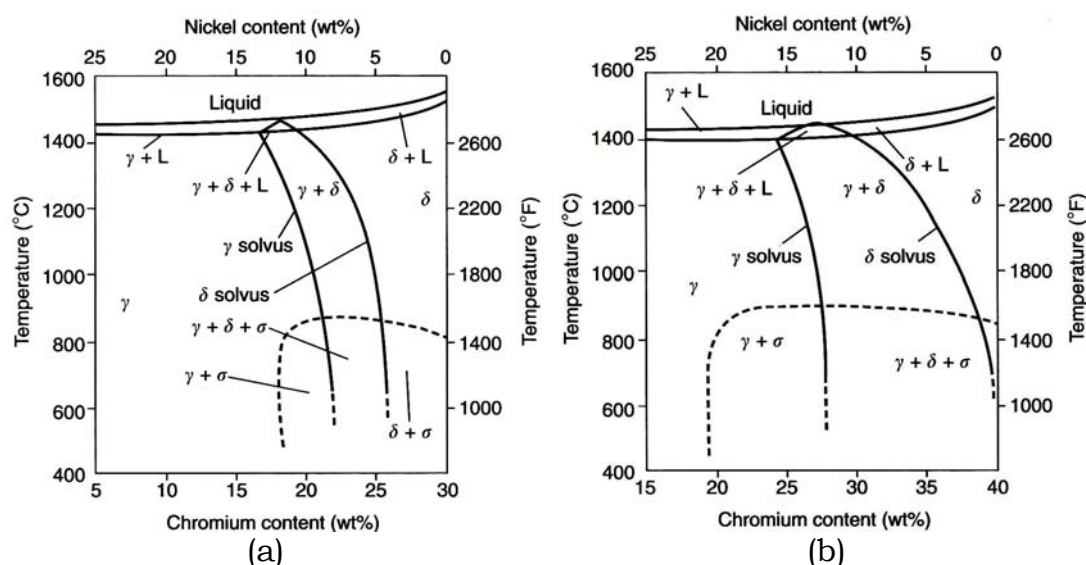
Figure 1.5 Pseudo-binary diagrams a) at 70 wt% Fe and b) at 60 wt% Fe [7]

The importance of this diagram lies on the small triangular region between the liquidus and solidus line, where the austenite, ferrite and liquid coexist. This triangular area separates the alloys that solidify as austenite (to the left) from those that solidify as ferrite. In the solid state ferrite is stable at elevated temperatures at chromium contents higher than 20 wt%, but as the temperature decreases, ferrite will transform partially to austenite in the range 20 to 25 wt%. Alloys that solidify as austenite remain as austenite upon cooling to room temperature, while alloys that solidify as ferrite, to the right of the triangular region, must cool through the two phase austenite + ferrite region, which results to the transformation of some of the ferrite to austenite. At chromium compositions farther to the right of the triangle, meaning higher Cr/Ni ratios, ferrite will become increasingly stable, until the existence of a fully ferritic microstructure in the alloy.

1.6   Constitution Diagrams

A matter of high importance is the prediction of the stainless steel weld metal constitution. Considerable effort has been done towards this direction for the past 75 years. Most of this research has dealt with the compositional effects on the welding microstructure of these alloys, yielding various diagrams and equations, which are based on the chemical composition of the alloys of interest. In this paragraph some of the most important constitution diagrams are presented.

1.6.1 Austenitic-Ferritic   Alloy   Systems: Early   Diagrams   and equivalency relationships

Regarding the prediction of stainless steel weld metal, the austenitic-ferritic alloy systems accumulate the most interest of all. This preference for the austenitic-ferritic systems began in 1920, when Strauss and Maurer [8] introduced a nickel-chromium diagram that allowed the prediction of various phases in the microstructure of wrought, slowly cooled steels. The design of the above diagram was used as a model for many diagrams to follow.

The Strauss-Maurer diagram was modified by Scherer et al. [9] in 1939 with the addition of austenite-ferrite stability lines. This revised diagram (Figure 1.6) uses the Strauss-Maurer axes that represent the actual chromium and nickel content. The left side of the diagram contains the lines proposed by Strauss and Maurer, while the right side of the diagram is the contribution of Scherer et al.
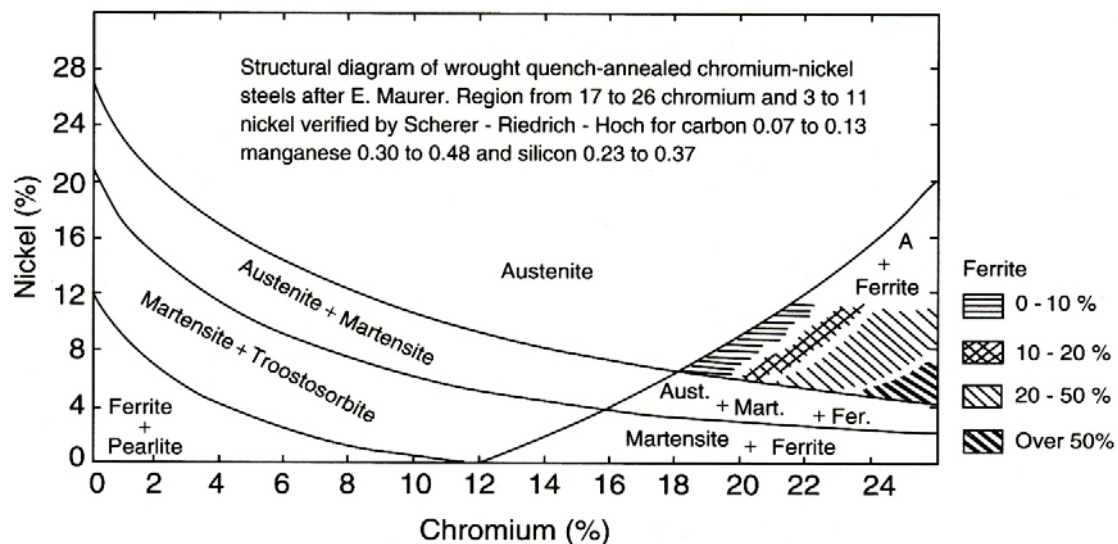

Figure 1.6 Strauss-Maurer nickel-chromium microstructure diagram as modified by Scherer et al. [9]

The use of curved lines, in the diagram, is significant and it became a pattern for the researchers for the next 30 years. The composition ranges of the diagram spanned 0 to 28 wt% nickel and 0 to 26 wt% chromium and within the nominal ranges of carbon, silicon

11

and manganese the diagram was useful for predicting various phases. The authors included phase regions of austenite, ferrite, martensite, pearlite, troostosorbite (an archaic term referring to tempered martensite and bainite) and mixtures of the above phases.

Newell and Fleischmann [10] recognizing that other elements besides chromium and nickel had an effect on the microstructure; hence, they developed an expression for austenite stability on the Strauss-Maurer diagram. The Newell-Fleischmann equation for the austenite/austenite + ferrite boundary is as follows:

$$Ni = \frac{(Cr + 2Mo - 16)^2}{12} - \frac{Mn}{2} + 30(0.10 - C) + 8 \qquad [1.1]$$

In the above equation the chemical symbols indicate the weight percentage of the element present. It can be noted from the coefficients which multiply the element weight percentage, that molybdenum is twice as effective in promoting ferrite as chromium, while manganese is one-half and carbon 30 times as effective as nickel in promoting austenite. With the appearance of the above coefficients, much of the research on the development and construction of constitution diagrams was centered on determining the coefficients of these formulas. In later years the formulas were termed *chromium-equivalent* and *nickel-equivalent equations*.

1.6.2 Schaeffler Diagram

Studying the Strauss-Maurer diagram and the equations of Newell-Fleischmann and other researchers, Anton Schaeffler [11] recognized that a combination of the above research could be applied to welding. His work focused on the construction of a constitution diagram for weld metals that would allow the prediction of weld metal microstructure based on the chemical composition.

The Schaeffler diagram contained chromium- and nickel-equivalent formulas for the axes, with ranges for the specific weld metal microstructural phases plotted in the diagram. Ferrite-promoting elements were included in the chromium-equivalent equation, while austenite-promoting elements were included in the nickel-equivalent. In Figure 1.7, one of the first Schaeffler constitution diagrams, with the Strauss-Maurer lines, is presented.

To determine the multiplying factors in the equivalent formulas, Schaeffler used formulas from previous research and his own experience. The original chromium- and nickel-equivalent equations of Schaeffler are shown in equations 1.2:

$$Ni_{eq} = Ni + 0.5Mn + 30C$$
$$Cr_{eq} = Cr + 2.5Si + 1.8Mo + 2Nb \qquad [1.2]$$

It is notable that Schaeffler did not include a nitrogen term in the nickel-equivalent equation, although nitrogen is known to be a strong austenite promoter. This was probably due to the difficulty in determining the nitrogen content in his time.
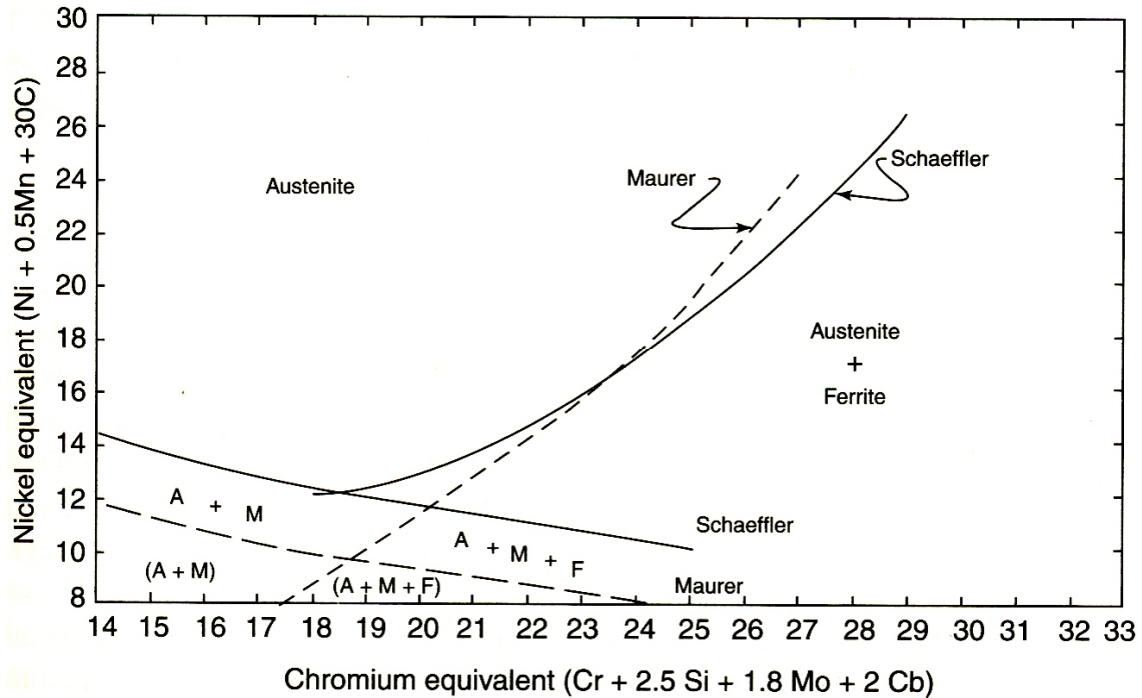
Figure 1.7 Schaeffler diagram of 1947, with the Maurer-Strauss curve [11]

The diagram was developed using the shielded metal arc welding (SMAW) process, where the nominal nitrogen content was estimated to be about 0.06 wt%. Because of this low value, nitrogen was not considered by Schaeffler as an alloying element; rather, it was incorporated into the diagram at a constant value. The diagram was considerably accurate for most of the 300 series alloys of that time, using conventional arc welding processes.

Along with the first diagram, Schaeffler reported a new equation for the phase boundary between fully austenitic alloys and alloys composed by austenite + ferrite:

$$Ni_{eq} = \frac{(Cr_{eq} - 16)^2}{12} + 12 \qquad [1.3]$$

Equation 1.3 that Schaeffler introduced differs from other formulas of other researchers, like Newell and Fleischmann, in the final constant term. It is notable, that this equation implies curvature, due to the quadratic term, and that the lines on the Schaeffler diagram are curved. In later studies in 1948, Schaeffler modified his

diagram (Figure 1.8) and the curved line of the austenite/austenite +ferrite boundary became a straight line [12].
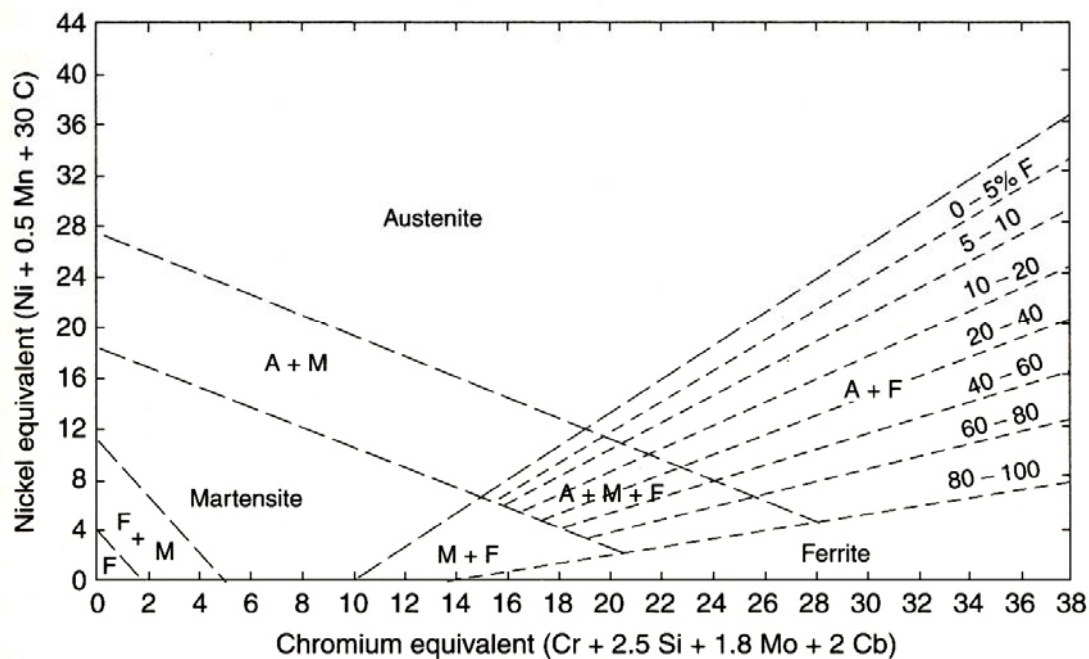
Figure 1.8 Schaeffler diagram of 1948, with linear boundaries [12]

The 1948 diagram increased the ability to quantitatively predict weld metal microstructure, adding additional isoferrite lines in the two-phase austenite + ferrite region, while retaining the original equivalency formulas. Finally, in 1949, Shaeffler published the final version of his constitution diagram [13], which is still in use today and is presented in Figure 1.9.
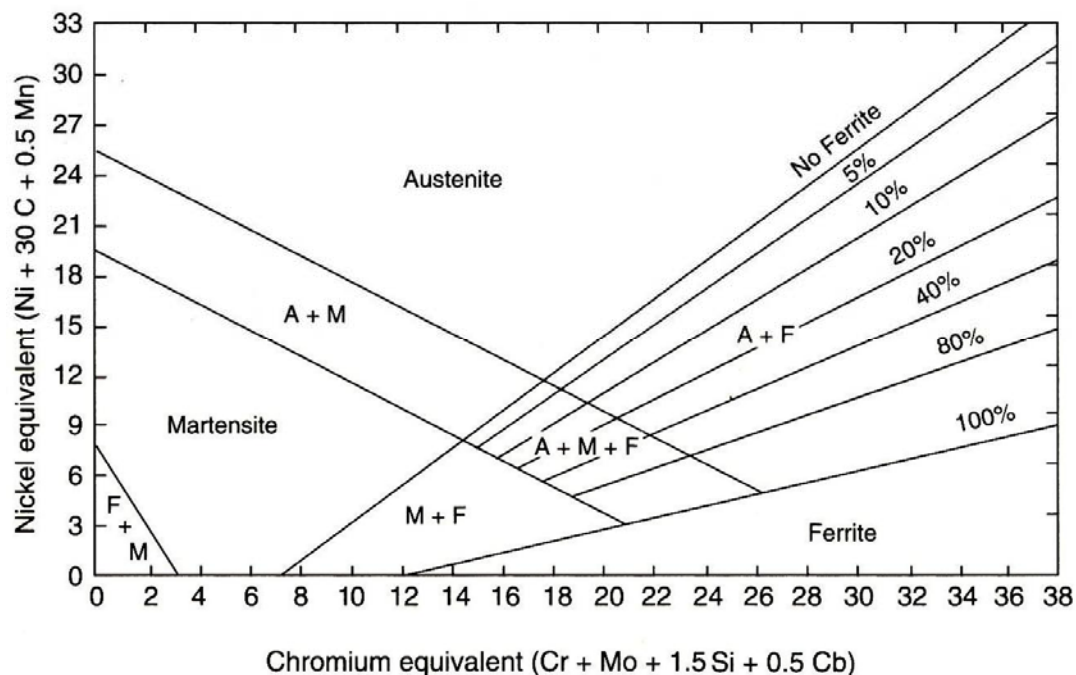
Figure 1.9 Schaeffler diagram of 1949, which is still in use [13]

The above diagram resulted after numerous examinations of weld metals. Changes were made to the coefficients of silicon, molybdenum and niobium, as well as a slight relocation of the phase boundaries.

1.6.3 DeLong Diagram

In 1956, DeLong et al. [14] introduced what was to become the next major trend in the development of constitution diagrams. Instead of predicting the weld metal constitution for the entire composition range of stainless steels, they focused on a particular region of interest, that of the 300 series austenitic stainless steels. Thus, the enlarged scale and the more precise line positions provided a more detailed and accurate prediction of the ferrite content in the stainless steel weld metal. A part of their research was the investigation of nitrogen on the weld metal microstructure, which showed that it has a major influence in the ferrite content.

The DeLong diagram of 1956 is shown in Figure 1.10, where the differences from the Schaffler diagram, regarding the same region, can be observed.
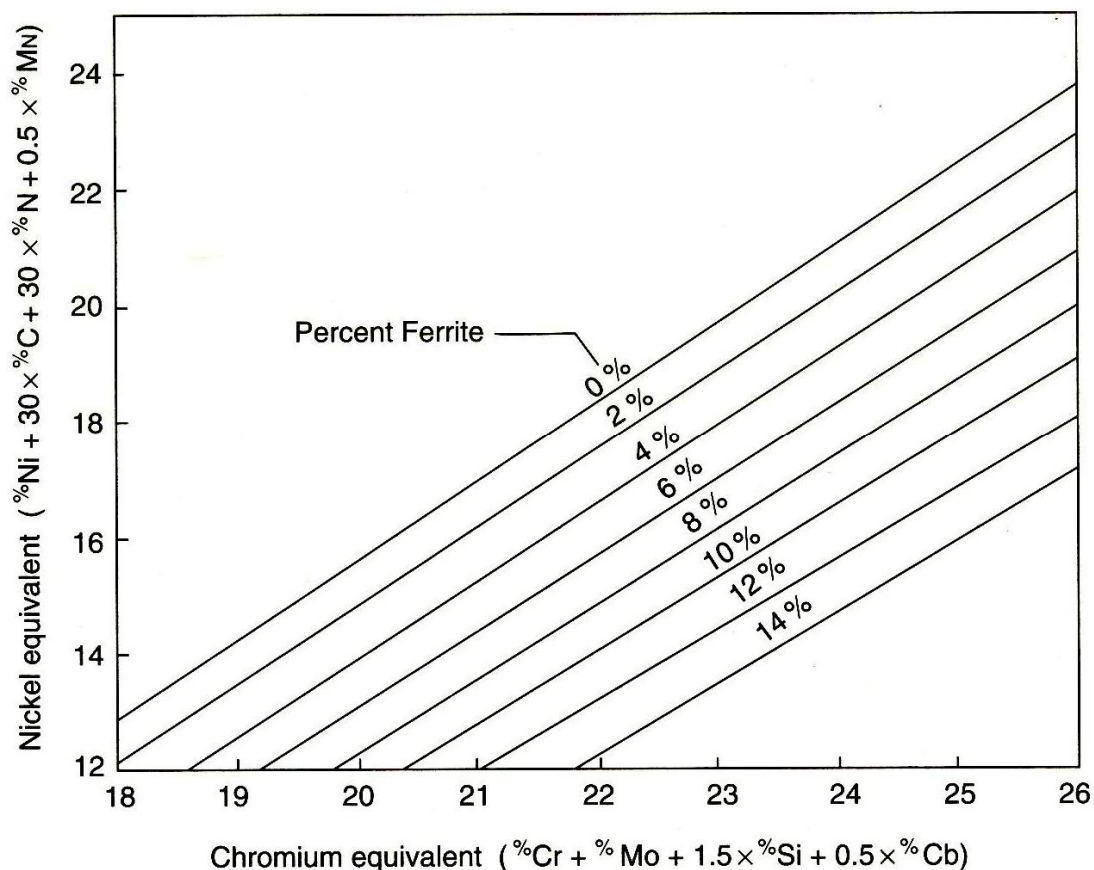
Figure 1.10 DeLong diagram of 1956 for austenitic stainless steels [14]

First, a term for nitrogen was added in the nickel equivalent, which affected the location of the lines in the diagram. Second, the slope of the isoferrite lines was increased due to the differences that

DeLong et al. found between the measured and calculated ferrite content on high-alloyed stainless steels types (e.g. 316, 316L and 309). A third difference is that the spacing between isoferrite lines is relatively constant, whereas on the Schaeffler diagram the spacing varies.

Further modifications were made by Long and DeLong [15] in 1973. The revised diagram, shown in Figure 1.11, exhibits improved ability in the prediction of the delta ferrite.
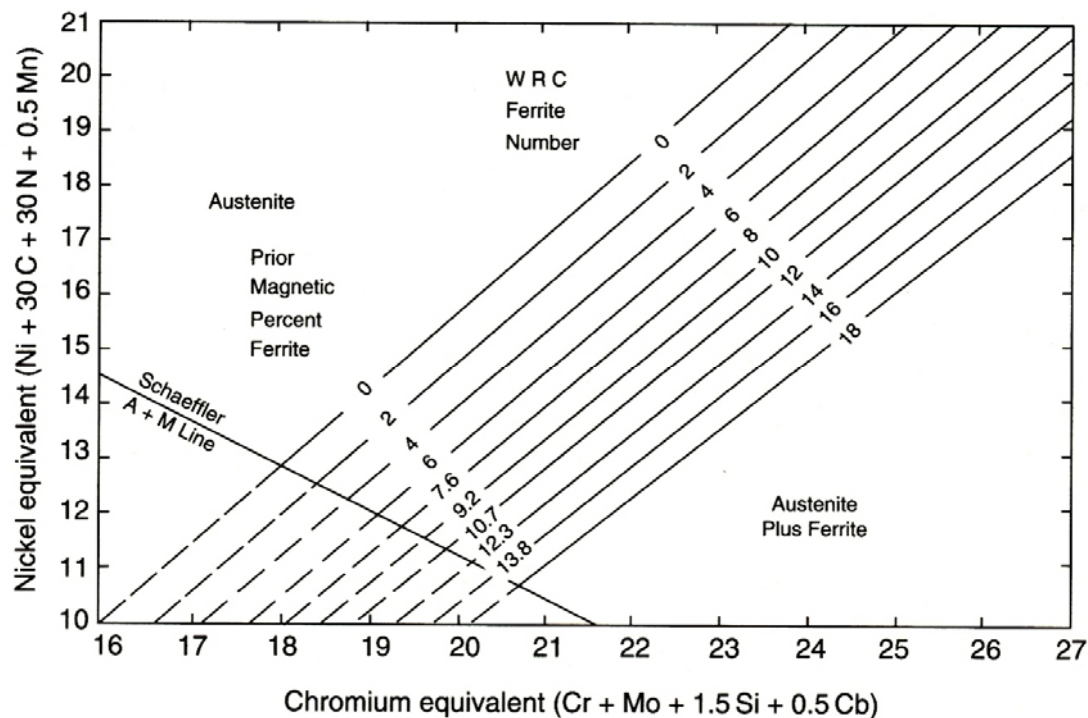
Figure 1.11 DeLong diagram of 1973, introducing the concept of Ferrite Number [15]

The major change was the addition of a *Ferrite Number (FN) scale* to the diagram. The introduction of this scale resulted due to the difficulty of measuring the ferrite content quantitatively by volume in stainless steel welds. The FN values are based on magnetic measurements, since the BCC delta ferrite is ferromagnetic, while the FCC austenite is not. The FN values are not intended to relate directly to percent ferrite, although at values below 10 they are considered to be similar.

The Welding Research Council (WRC) Subcommittee on Welding Stainless Steel adopted FN as its value for measuring ferrite in 1973 [16], and its method for calibration is specified by the AWS A4.2 and ISO 8249 standards. Long and DeLong [15], also reported that their diagram, which has been termed the *DeLong-WRC Diagram,* is fairly insensitive to the normal range of heat input variations associated with arc welding. Thus, it could be applied with a reasonable degree of accuracy to processes such as SMAW, GTAW, GMAW and SAW.

1.6.4 WRC-1988 and WRC-1992 Diagrams

The Subcommittee on Welding Stainless Steel of the Welding Research Council initiated an effort in the mid-1980s to revise and expand the Schaeffler and DeLong diagrams, in order to improve the accuracy of ferrite prediction in stainless steel weld metal. Hence, in 1988, in a study funded by WRC, Siewert et al. [17] proposed a new predictive diagram, which covered an expanded range of compositions, from 0 to 100 FN, compared to the 0 to 18 FN range of the DeLong diagram. The diagram, shown in Figure 1.12, also included boundaries that defined the solidification mode and became known as the *WRC-1988 diagram.*
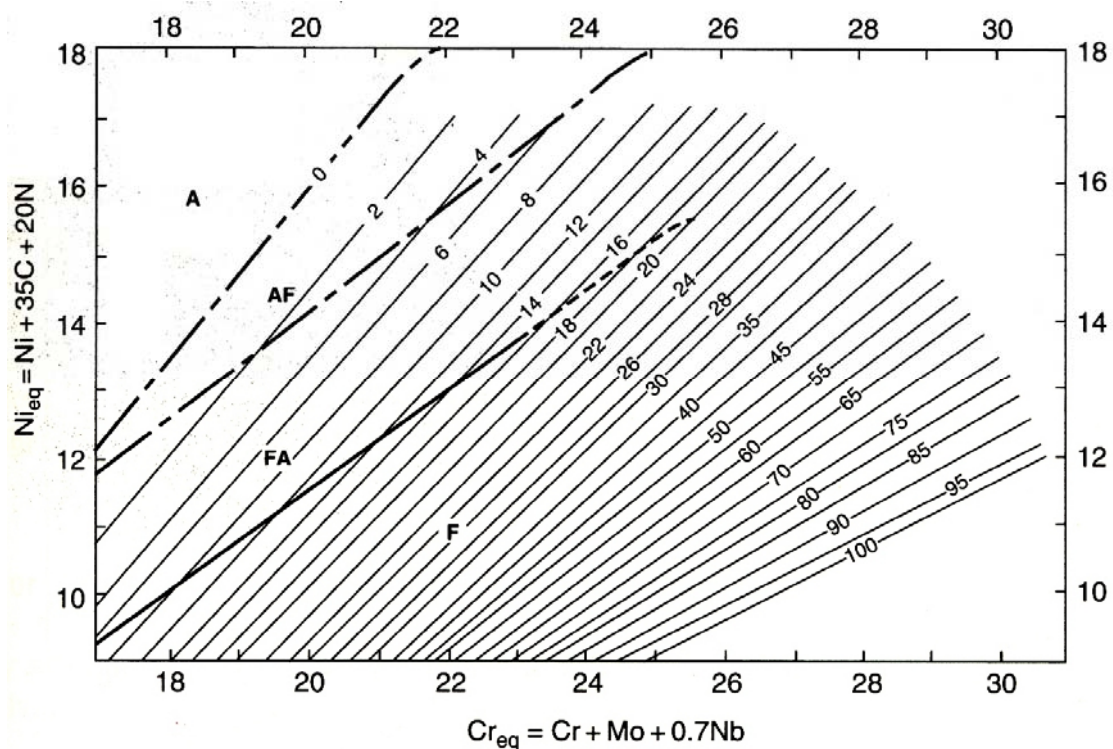
Figure 1.12 WRC-1988 diagram with solidification mode boundaries [17]

The above diagram resulted from an extremely large database of welds (approximately 950) gathered from electrode manufacturers, research institutes and the literature.

New equivalency formulas were developed which removed the manganese coefficient from the nickel equivalent, thereby eliminating the systematic overestimation of FN in highly alloyed weld metals. The WRC-1988 equivalency formulas are given as:

$$Cr_{eq} = Cr + Mo + 0.7Nb$$
$$Ni_{eq} = Ni + 35C + 20N \qquad [1.4]$$

Despite its accuracy in predicting the ferrite content in stainless steels welds, the WRC-1988 diagram was reviewed and evaluated. Shortly after the diagram's publication, Kotecki [18] used independent data from 200 welds to confirm the improved predictive accuracy of WRC-1988 compared to the DeLong diagram. At the same time, the effect of copper on ferrite content became a topic of interest due to the increased use of duplex stainless steels, which may contain up to 2% copper. Presenting his work, Lake [19] showed that the addition of a copper coefficient, in the nickel-equivalent formula, would improve the accuracy of FN prediction when copper is an important alloying element. Lake proposed a value for the copper coefficient from 0.25 to 0.30. Various researchers followed Lake's study and proposed their estimations for the copper coefficient, in order to add them in the Schaeffler and DeLong nickel-equivalents. Finally, Kotecki [20], using Lake's data as a basis, proposed a coefficient of 0.25 for copper in the nickel-equivalent formula.

In 1992, Kotecki and Siewert [21] proposed a new diagram, which was exactly the same with the WRC-1988 diagram except that it included the coefficient 0.25 for copper in the nickel-equivalent formula:

$$Ni_{eq} = Ni + 35C + 20N + 0.25Cu \qquad [1.5]$$

The WRC-1992 diagram is presented in Figure 1.13. Whereas the extended axes of the diagram allow a wide range of base and filler metal to be plotted, the FN prediction is valid only when the weld metal composition falls within the iso-FN lines of the diagram.
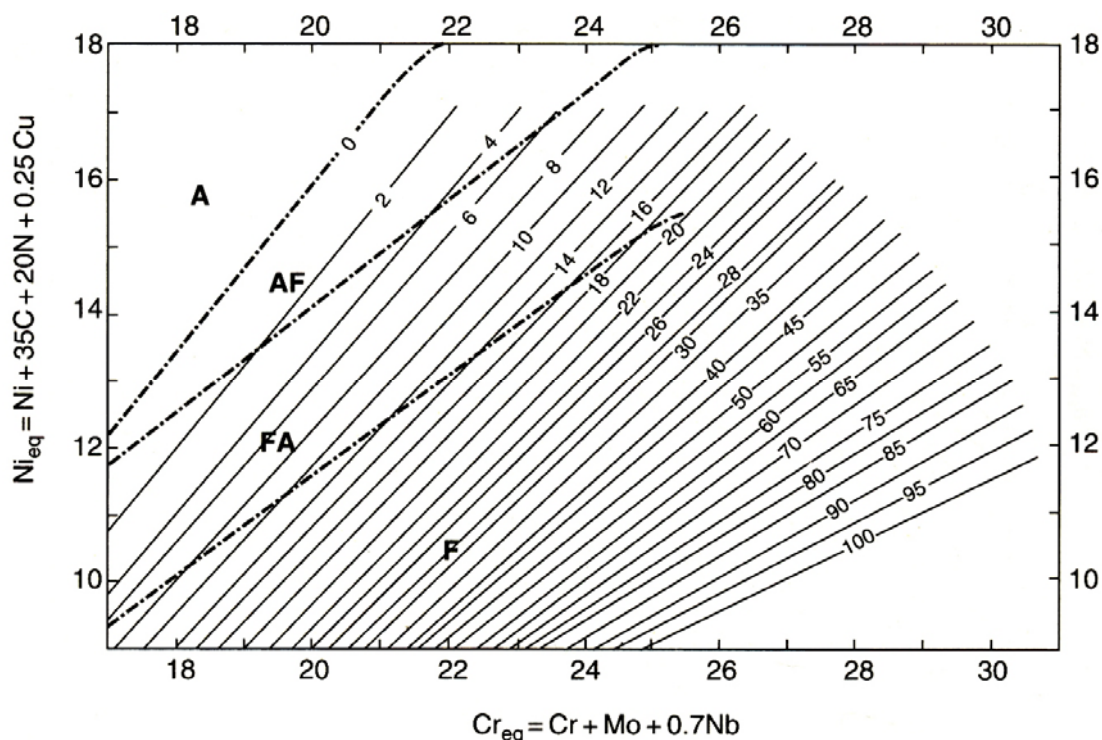
Figure 1.13 The WRC-1992 diagram [21]

At the present time, the WRC-1992 diagram is the most reliable and most accurate for the prediction of Ferrite Number in the austenitic and duplex stainless steel welds. It has been widely accepted worldwide and has replaced the DeLong diagram in the ASME code.

The only shortcoming of the WRC-1992 may be the absence of a factor for titanium, which is a potent carbide former and can influence the phase balance by removing carbon from the matrix. Titanium is also a ferrite-promoting element in the absence of carbon.

Chapter Bibliography

1. John C. Lippold and Damian J. Kotecki, *Welding Metallurgy and Weldability of Stainless Steels*, 2005 John Wiley & Sons Inc.
2. AISI – American Iron and Steel Institute, www.steel.org
3. A. J. Sedriks, *Corrosion of Stainless Steels*, 1996 John Wiley & Sons Inc.
4. Sindo Kou, *Welding Metallurgy*, 2nd Edition 2003 John Wiley & Sons Inc.
5. *ASM Metals Handbook*, 1992 - Vol. 3, ASM International, Materials Park, OH
6. D. Peckner, I. M. Bernstein, *Handbook of Stainless Steels*, 1977 McGraw-Hill, New York
7. J. C. Lippold, W. F. Savage, *Solidification of austenitic stainless steel weldments, 1: a proposed mechanism*, Welding Journal (1979) 58(12), pp. 362-374
8. B. Strauss, E. Maurer, *Die hochlegierten Chromnickelstahle als nichtrostende Stahle,* Kruppsche Monatshefte, 1920 1(8), pp. 129-146
9. R. Scherer, G. Riedrick ad G. Hoch, *Einfluss eines Gahalts an Ferrit in austenitischer Chrom-Nickel-Stahlen auf den Kornzerfall*, Archiv für das Eisenhűttenwesen, 1939 (13) July, pp. 13-52
10. H. D. Newell, M. Fleischmann, *Hot rolled metal article and method of making same*, 1938 U.S. patent 2,118,683
11. A. L. Schaeffler, *Selection of austenitic electrodes for welding dissimilar metals*, Welding Journal (1947) 26(10), pp. 601s-620s
12. A. L. Schaeffler, *Welding dissimilar metals with stainless electrodes*, Iron Age, 1948 July pp. 162-172
13. A. L. Schaeffler, *Constitution diagram for stainless steel weld metal, etal Progress*, 1949, 56(11) pp. 680-680B
14. W. T. DeLong, G. A. Ostrom, E. R. Szumachowski, *Measurement and calculation of ferrite in stainless-steel weld metal*, Welding Journal (1956) 35(11), pp. 521s-528s
15. C. J. Long, W. T. DeLong, *The ferrite content of austenitic steel weld metal*, Welding Journal (1973) 52(7), pp. 281s-297s
16. W. T. DeLong, *Calibration procedure for instruments to measure the delta ferrite content of austenitic stainless steel weld metal*, Welding Journal (1973) 52(2), pp. 69s
17. T. A. Siewert, C. N. McCowan, D. L. Olson, Ferrite Number prediction to 100 FN in stainless steel weld metal, Welding Journal, (1988) 67(12), pp.289s-298s
18. D. J. Kotecki, *Verification of the NBS-CSM Ferrite Diagram*, 1988, IIW Document II-C-834-88, American Council of the International Institute of Welding, Miami, FL
19. F. B. Lake, *Effect of Cu on stainless steel weld metal ferrite content*, 1990, paper presented at AWS Annual Convention
20. D. J. Kotecki, *Ferrite measurement and control in duplex stainless steel welds*, in Weldability of Materials: Proceedings of the Materials Symposium, October 1990, ASM International, Materials Park, OH.
21. D. J. Kotecki, T. A. Siewert, WRC-1992 constitution diagram for stainless steel weld metals: a modification of the WRC-1988 diagram, Welding Journal, (1992) 71(5), pp. 171s-178s

2nd Chapter

Austenitic Stainless Steels

2. Austenitic Stainless Steels

Austenitic stainless steels represent the largest of the general groups of stainless steels and are produced in higher quantities than any other group. They exhibit good corrosion resistance in most environments. Austenitic stainless steels have strength equivalent to those of mild steels, approximately 210 MPa minimum yield strength at ambient temperature, and are not transformation hardenable. Low-temperature impact properties are good for these alloys, making them useful in cryogenic applications. Service temperatures can be up to 760 °C or even higher, but the strength and oxidation resistance of these steels are limited at such high temperatures. Austenitic stainless steels can be strengthened significantly by cold working. They are often used in applications requiring good atmospheric or elevated temperature corrosion resistance. Austenitic stainless steels are generally considered to be weldable, if proper precautions are followed.

Elements that promote the formation of austenite, most notably nickel, are added to the austenitic stainless steels in large quantities (generally over 8%). Other austenite-promoting elements are added in small, but sufficient, quantities. Such elements are C, N and Cu. Carbon and nitrogen are strong austenite promoters, which can be seen from the various values in nickel equivalency formulas. Carbon is added to improve creep resistance at high temperatures. Nitrogen is added to some austenitic alloys in order to improve strength, mainly at ambient and cryogenic temperatures, sometimes more than doubling it. Nitrogen-strengthened alloys are designated with a suffix N added to their AISI 300 series designation (e.g., 316LN). The AISI 200 series are also nitrogen strengthened and commonly referred to under various trade names, such as Nitonic®.

Austenitic stainless steels generally have good ductility and toughness and exhibit significant elongation during tensile loading. They are more expensive than the martensitic and low to medium Cr ferritic grades, due to their higher alloy content. Despite the cost, they offer distinct engineering advantages, particularly with respect to formability and weldability, which often reduce the overall cost, compared to the other groups of stainless steels.

Although there are a wide variety of austenitic stainless steels, the oldest and most commonly used are the 300 series. Most of these alloys are based on the 18Cr-8Ni system, with additional alloying elements or modifications to provide unique or enhanced properties. Type 304 is the foundation of this alloy series and along with 304L represents the most commonly selected austenitic grade. While type 316 substitutes approximately 2%Mo for a nearly equal amount of Cr to improve pitting corrosion resistance.

The stabilized grades, 321 and 347, contain small additions of Ti and Nb, respectively, to combine with carbon and reduce the tendency for intergranular corrosion due to Cr-carbide precipitation. The L grades became popular in the 1960s and 1970s with introduction of

AOD (argon-oxygen decarburization) meting practice that reduced the cost differential between standard (not low carbon) and L grades. These low-carbon grades (304L, 316L) have been widely used in applications where intergranular attack and intergranular stress corrosion cracking are a concern.

Austenitic stainless steels are used in a wide range of applications, including structural support and containment, architectural uses, kitchen equipment and medical products. They are widely used not only because of their corrosion resistance but because they are readily formable, fabricable and durable. Some highly alloyed grades are used for very high temperature service (over 1000ºC) for applications such as heat-treating baskets. In addition to higher chromium levels, these alloys normally contain higher levels of silicon (and sometimes aluminum) and carbon, to maintain oxidation and/or carburization resistance and strength, respectively.

It should be pointed out, that the common austenitic stainless steels are not an appropriate choice in some common environments such as seawater or other chloride-containing media, or highly caustic environments. This is due to their susceptibility to stress corrosion cracking, a phenomenon that afflicts the base metal, HAZ and weld metal in these alloys. Finally, care should be taken when selecting stainless steels that will be under significant stress in these environments.

2.1   Standard Alloys and Consumables

According to the designation by the American Iron and Steel Institute (AISI), austenitic stainless steels include both the 200 and 300 series alloys. The, not so common, 200 series alloys contain high levels of carbon, manganese and nitrogen and are used in specialty applications, such as where galling resistance is required. These alloys also have lower nickel content, than the 300 series alloys, to balance the high carbon and nitrogen levels.

The 300 series alloys are by far the most widely used of the austenitic stainless steels grades. A list of the most common of the 300 series is provided in Table 2.1.

The most used alloys, Types 304, 316, 321 and 347 and their variants, are of the "18-8" type with normal values of 18Cr and 8-10Ni. The L grades represent low-carbon variants with a nominal carbon level of 0.03 wt%. These alloys have improved resistance to intergranular corrosion in corrosive environments. Due to their low carbon content, they prevent the formation of $M_{23}C_6$ carbide and the depletion of chromium on the alloy surface. The H grades are used at elevated temperatures since they have higher elevated temperature strength than standard of L grades. This property derives from their carbon content, which approaches 0.1 wt%. The N grades have nitrogen added, intentionally, to levels as high as 0.20 wt% in the 300 series (e.g. 304N, 316N, 316LN). Nitrogen is also added in higher

levels in these alloys when the manganese content is also high. This is due to the fact that manganese increases the solubility of nitrogen in the austenitic phase. The higher nitrogen content improves the strength, galling resistance and pitting corrosion resistance of austenitic stainless steels.

Table 2.1 Composition of Standard Wrought Austenitic Stainless Steels

Type	Composition (wt %)*									
	C	Mn	P	S	Si	Cr	Ni	Mo	N	Other
201	0.15	5.5-7.5	0.06	0.03	1.0	16.0-18.0	3.5-5.5	-	0.25	-
302	0.15	2.0	0.045	0.03	1.0	17.0-19.0	8.0-10.0	-	-	-
304	0.08	2.0	0.045	0.03	1.0	18.0-20.0	8.0-10.5	-	-	-
304L	0.03	2.0	0.045	0.03	1.0	18.0-20.0	8.0-12.0	-	-	-
304H	0.04-0.1	2.0	0.045	0.03	1.0	18.0-20.0	8.0-10.5	-	-	-
308	0.08	2.0	0.045	0.03	1.0	19.0-21.0	10.0-12.0	-	-	-
309	0.20	2.0	0.045	0.03	1.0	22.0-24.0	12.0-15.0	-	-	-
310	0.25	2.0	0.045	0.03	1.0	24.0-26.0	19.0-22.0	-	-	-
316	0.08	2.0	0.045	0.03	1.0	16.0-18.0	10.0-14.0	2.0-3.0	-	-
316L	0.03	2.0	0.045	0.03	1.0	16.0-18.0	10.0-14.0	2.0-3.0	-	-
317	0.08	2.0	0.045	0.03	1.0	18.0-20.0	11.0-15.0	3.0-4.0	-	-
321	0.08	2.0	0.045	0.03	1.0	17.0-19.0	9.0-12.0	-	-	Ti:5xC-0.70
330	0.10	2.0	0.045	0.03	0.75-1.5	17.0-20.0	34.0-37.0	-	-	-
347	0.08	2.0	0.045	0.03	1.0	17.0-19.0	9.0-13.0	-	-	Nb:10xC-1.00

* A single value is a maximum

Austenitic alloys containing titanium and niobium, such as Types 321 and 347, are known as *stabilized grades*. The addition of these alloying elements stabilizes the alloy against the formation of $M_{23}C_6$ chromium carbides. Titanium and niobium both form stable MC-type carbides at elevated temperature resulting to the restriction of the chromium-rich carbide formation. Adding those elements at levels up to 1.0 wt% will result to the reduction of the matrix carbon content, which makes the formation of chromium-rich carbides more difficult. Thus, the possibility for sensitization that can lead to intergranular corrosion in austenitic stainless steels is reduced.

Many other alloys can be found amongst the austenitic grades, such as the superaustenitic grades. These alloys exhibit unique characteristics and weldability concerns.

Austenitic stainless steels filler metals, usually, have similar composition with the base metal, but it can also vary depending on the welding procedure or the service application of the steel. Austenitic stainless steel filler metals are listed in Table 2.2, which is divided in three parts, reflecting to the AWS specifications for consumables:

1. Specification AWS A5.4 for covered electrodes used in the SMAW process.
2. Specification AWS A5.9 for bare wire and tubular metal-cored electrodes used in the GMAW and GTAW process.
3. Specification AWS A5.22 for gas-shielded flux-cored electrodes used in the FCAW process.

Table 2.2 Classification of Austenitic Stainless Steel AWS Filler Metals

Type	Composition (wt %)*									
	C	Mn	P	S	Si	Cr	Ni	Mo	N	Other
Part 1: Covered Electrodes from AWS A5.4										
219	0.06	8.0-10.0	0.04	0.03	1.0	19.0-21.5	5.5-7.0	0.75	0.1-0.3	-
308	0.08	0.5-2.5	0.04	0.03	1.0	18.0-21.0	9.0-11.0	0.75	-	-
308H	0.04-0.08	0.5-2.5	0.04	0.03	1.0	18.0-21.0	9.0-11.0	0.75	-	-
308L	0.04	0.5-2.5	0.04	0.03	1.0	18.0-21.0	9.0-11.0	0.75	-	-
309	0.15	0.5-2.5	0.04	0.03	1.0	22.0-25.0	12.0-14.0	0.75	-	-
309L	0.04	0.5-2.5	0.04	0.03	1.0	22.0-25.0	12.0-14.0	0.75	-	-
310	0.08-0.20	1.0-2.5	0.03	0.03	1.0	25.0-28.0	20.0-22.5	0.75	-	-
316	0.08	0.5-2.5	0.04	0.03	1.0	17.0-20.0	11.0-14.0	2.0-3.0	-	-
316H	0.04-0.08	0.5-2.5	0.04	0.03	1.0	17.0-20.0	11.0-14.0	2.0-3.0	-	-
316L	0.04	0.5-2.5	0.04	0.03	1.0	17.0-20.0	11.0-14.0	2.0-3.0	-	-
317	0.08	0.5-2.5	0.04	0.03	1.0	18.0-21.0	12.0-14.0	3.0-4.0	-	-
317L	0.04	0.5-2.5	0.04	0.03	1.0	18.0-21.0	12.0-14.0	3.0-4.0	-	-
330	0.18-0.25	1.0-2..5	0.04	0.03	0.75-1.5	14.0-17.0	33.0-37.0	0.75	-	-
347	0.08	0.5-2.5	0.04	0.03	1.0	18.0-21.0	9.0-11.0	0.75	-	Nb:10xC-1.00
Part 2: Bare Electrodes, Bare Rods, Tubular Metal-Cored Electrodes and Strips from AWS A5.9										
219	0.05	8.0-10.0	0.03	0.03	1.00	19.0-21.5	5.5-7.0	0.75	0.1-0.3	-
308	0.08	1.0-2.5	0.03	0.03	0.3-0.65	19.5-22.0	9.0-11.0	0.75	-	-
308H	0.04-0.08	1.0-2.5	0.03	0.03	0.3-0.65	19.5-22.0	9.0-11.0	0.75	-	-
308:	0.03	1.0-2.5	0.03	0.03	0.3-0.65	19.5-22.0	9.0-11.0	0.75	-	-
308Si	0.08	1.0-2.5	0.03	0.03	0.65-1.0	19.5-22.0	9.0-11.0	0.75	-	-
308LSi	0.03	1.0-2.5	0.03	0.03	0.65-1.0	19.5-22.0	9.0-11.0	0.75	-	-
309	0.12	1.0-2.5	0.03	0.03	0.3-0.65	23.0-25.0	12.0-14.0	0.75	-	-
309L	0.03	1.0-2.5	0.03	0.03	0.3-0.65	23.0-25.0	12.0-14.0	0.75	-	-
309Si	0.12	1.0-2.5	0.03	0.03	0.65-1.0	23.0-25.0	12.0-14.0	0.75	-	-
309LSi	0.03	1.0-2.5	0.03	0.03	0.65-1.0	23.0-25.0	12.0-14.0	0.75	-	-
310	0.08-0.15	1.0-2.5	0.03	0.03	0.3-0.65	25.0-28.0	20.0-22.5	0.75	-	-
316	0.08	1.0-2.5	0.03	0.03	0.3-0.65	18.0-20.0	11.0-14.0	2.0-3.0	-	-
316H	0.04-0.08	1.0-2.5	0.03	0.03	0.3-0.65	18.0-20.0	11.0-14.0	2.0-3.0	-	-
316L	0.03	1.0-2.5	0.03	0.03	0.3-0.65	18.0-20.0	11.0-14.0	2.0-3.0	-	-
316Si	0.08	1.0-2.5	0.03	0.03	0.65-1.0	18.0-20.0	11.0-14.0	2.0-3.0	-	-
316LSi	0.03	1.0-2.5	0.03	0.03	0.65-1.0	18.0-20.0	11.0-14.0	2.0-3.0	-	-
317	0.08	1.0-2.5	0.03	0.03	0.3-0.65	18.5-20.5	13.0-15.0	3.0-4.0	-	-
317L	0.03	1.0-2.5	0.03	0.03	0.3-0.65	18.5-20.5	13.0-15.0	3.0-4.0	-	-
330	0.18-0.25	1.0-2.5	0.03	0.03	0.3-0.65	15.0-17.0	34.0-37.0	0.75	-	-
347	0.08	1.0-2.5	0.03	0.03	0.3-0.65	19.0-21.5	9.0-11.0	0.75	-	Nb:10xC-1.00
347Si	0.08	1.0-2.5	0.03	0.03	0.65-1.0	19.0-21.5	9.0-11.0	0.75	-	Nb:10xC-1.00
*Part 3: Gas-Shielded Flux Cored Electrodes from AWS A5.22** *										
308	0.08	0.5-2.5	0.04	0.03	1.0	18.0-21.0	9.0-11.0	0.5	-	-
308L	0.04	0.5-2.5	0.04	0.03	1.0	18.0-21.0	9.0-11.0	0.5	-	-
308H	0.04-0.08	0.5-2.5	0.04	0.03	1.0	18.0-21.0	9.0-11.0	0.5	-	-
309	0.10	0.5-2.5	0.04	0.03	1.0	22.0-25.0	12.0-14.0	0.5	-	-
309L	0.04	0.5-2.5	0.04	0.03	1.0	22.0-25.0	12.0-14.0	0.5	-	-
310	0.20	1.0-2.5	0.03	0.03	1.0	25.0-28.0	20.0-22.5	0.5	-	-
316	0.08	0.5-2.5	0.04	0.03	1.0	17.0-20.0	11.0-14.0	2.0-3.0	-	-
316L	0.04	0.5-2.5	0.04	0.03	1.0	17.0-20.0	11.0-14.0	2.0-3.0	-	-
317L	0.04	0.5-2.5	0.04	0.03	1.0	18.0-21.0	12.0-14.0	3.0-4.0	-	-
347	0.08	0.5-2.5	0.04	0.03	1.0	18.0-21.0	9.0-11.0	0.5	-	Nb:8xC-1.00

*A single value is a maximum

** Self-shielded flux-cored stainless steel electrodes are also included in the AWS A5.22 standard. They have virtually identical composition limits to those of the gas-shielded electrodes except that the Cr limits tend to be slightly higher in the ferrite-containing grades, to compensate for expected higher nitrogen in the self-shielded deposit.

2.2 Alloying Elements and γ-promoting Elements

Stainless steels are iron-base alloys with iron contents ranging from 50 to 88 wt% of the composition. The main alloying additions to stainless steel grades are chromium and carbon for the ferritic and martensitic grades, with the addition of nickel for the austenitic and duplex grades. Essentially all stainless steel grades contain manganese and silicon as intentional additions. Other alloying additions include molybdenum, niobium, titanium, aluminum, copper, tungsten, nitrogen and many others to improve their fabrication, develop special properties, enhance corrosion resistance, or influence microstructure. Impurity elements commonly found in stainless steels are nitrogen, oxygen, sulfur and phosphorus. All the above alloy and impurity element have some effect on weldability and performance. The level of these elements in the base or filler metal is controlled by the material specification, in order to assure that the steel will perform as anticipated.

2.2.1 Chromium

The primary objective of the chromium addition is to provide corrosion protection to the steel. Its effectiveness can be observed, when the steel is exposed to oxidized environment, such as nitric acid. Under this oxidizing condition, and due to the chromium content, an oxide, of stoichiometry $(Fe,Cr)_2O_3$, forms on the steel surface. The percentage of chromium increases the stability of the oxide since it has a much higher affinity for oxygen than does iron. When the chromium exceeds approximately 12 wt%, the steel is considered "stainless" under ambient conditions. For more aggressive environments, higher content of chromium may be required for the stability of the oxide.

Chromium is also a ferrite promoter, so that an iron-chromium alloy with more than 12 wt% chromium will be fully ferritic. In the Fe-Cr-C and Fe-Cr-Ni-C alloys, chromium will promote ferrite formation and retention in martensitic, austenitic and duplex grades. In the ferritic alloys chromium is the primary alloying element stabilizing the ferritic microstructure.

Chromium is also known as strong carbide former. The most common Cr-rich carbide is the $M_{23}C_6$, where "M" is predominantly chromium but may also have some fraction of Fe and Mo present. This carbide can be found in virtually all stainless steels. Another, not so common, carbide, which is possible to form, is Cr_7C_3. Chromium also combines with nitrogen to form nitrides. The most common nitride is Cr_2N, which can be found in both the ferritic and duplex grades, but not in the austenitic ones.

Chromium is also a key ingredient in the formation of intermetallic compounds, many of which can embrittle the stainless steels. The most common is σ (sigma) phase, which is a (Fe,Cr) compound and in the Fe-Cr systems forms just below the 815ºC. The

sigma phase can be found in any stainless steel but it is most common in the Cr-rich austenitic, ferritic and duplex grades. Chromium is also present in the x (chi) and Laves intermetallic phases.

Chromium is a substitutional element in body-centered cubic (BCC) and in the face-centered cubic (FCC) crystal lattices, and so from a mechanical properties standpoint, chromium will provide some degree of solid solution strengthening.

2.2.2 Nickel

The primary purpose of nickel's addition is to promote the austenitic phase as the predominant phase, in order to produce austenitic or austenitic-ferritic (duplex) alloys. With the addition of sufficient nickel in the stainless steels, the austenitic phase field can be greatly expanded such that austenite is stable at ambient temperature and below. Nickel is not a strong carbide former and does not form intermetallic compounds, although there is evidence that its presence, in the alloy, may influence precipitation kinetics [2]. There is some evidence, that the presence of nickel in ferritic alloys improves general corrosion resistance. However, nickel has been associated with a decrease in stress corrosion cracking resistance. Copson [3] showed that with addition of nickel to a Fe-20Cr alloy, in an aggressive Cl-containing environment, a decrease in stress corrosion cracking resistance occurs. The Copson curve, that was created, shows that the lowest stress corrosion cracking resistance occurs in the range of 8-12 wt% Ni in the alloy. Azuma e.a. [7] also showed that the presence of high Ni content decreases the crevice corrosion resistance of austenitic stainless steels, but it increases the crevice corrosion resistance of ferritic stainless steels.

Nickel is good solid solution strengthener, but is most beneficial in terms of improving toughness in both the martensitic and ferritic grades.

2.2.3 Manganese

As an alloying element, manganese is added to all steels. In the austenitic stainless steels it is normally present in the range 1-2 wt%, while in the ferritic and martesnitic grades is usually added in less than 1 wt%. The original purpose of manganese addition was the prevention of hot shortness during casting, which is a form of solidification cracking associated with the formation of low melting point iron-sulfide eutectic constituents. Manganese combines more readily with sulfur, than does iron, forming stable manganese sulfide (MnS) and effectively eliminating the hot shortness problem [1].

Manganese is considered to bean austenite-promoting element, although the degree of promotion is depended on the amount present and the level of nickel in the alloy. Manganese efficiency is the stabilization of austenite at low temperatures, in order to avoid the

transformation to martensite. Its potency to promote austenite at elevated temperatures is dependent on the overall composition of the alloy. In austenitic stainless steels, such as the 304 type, it appears to have little effect in promoting austenite versus ferrite.

Sometimes, manganese is added to specialty in order to increase the solubility of nitrogen, which enhances the alloy with specific mechanical properties, in the austenitic phase. The effect of manganese on the mechanical properties of the alloy is minimal.

2.2.4 Silicon

Silicon is added virtually to all stainless steels and it is added primarily for deoxidation during melting. In most alloys its content ranges from 0.3 to 0.6 wt%. Silicon can be substituted, in some cases, with aluminum, as a deoxidizer, but this is rarely the case. It has been found to improve corrosion resistance [8] and it is added to some heat-resisting alloys in the range of 1 to 3 wt% to improve oxide scaling resistance at elevated temperature [1]. The role of silicon, regarding the promotion of the austenitic or the ferritic phase is not clear yet. In austenitic stainless steels, in levels up to 1 wt%, silicon appears to have no effect on the phase balance at all, but higher levels appear to promote ferrite. In martensitic and ferritic grades, silicon the addition of silicon seems to help the ferrite promotion.

Silicon forms a number of silicides ($FeSi$, Fe_2Si, Fe_3Si, Fe_5Si_3) and a Cr_3Si intermetallic, all of wich tend to embrittle the structure [1]. It is also known, that silicon segregates during solidification, resulting in the formation of low melting eutectic constituents, particularly in combination with nickel [1]. For the above reasons, silicon is held below 1 wt%.

Silicon's advantage is the improvement of the fluidity of molten steel. For this reason, silicon can be added, in somewhat higher than normal amounts, in the weld filler metals. Some stainless steels, particularly the austenitic grades, can be quite sluggish in the molten state during solidification and the addition of silicon in the weld filler metal can improve their fluidity.

2.2.5 Molybdenum

Molybdenum is added to some stainless steels and its effect varies depending on the steel grade. Regarding the austenitic, ferritic and duplex stainless steels, molybdenum is added in amounts up to 6 wt% or more in the super austenitic grades. The addition of molybdenum in the above grades increases the corrosion resistance and particularly the pitting and crevice corrosion resistance. In austenitic stainless steels, Mo improves elevated temperature strength, which can also be negative, while alloys containing Mo are more difficult to hot work.

Some of the martensitic grades contain o as carbide former. The addition of as little, as 0.5 wt% Mo increases the secondary hardening

characteristics of the steel, resulting to higher room temperature yield and tensile strength and improved elevated-temperature properties.

Molybdenum is a ferrite-promoting element and its presence will promote ferrite formation and retention in the microstructure.

2.2.6 Interstitial Elements – Carbon and Nitrogen

Carbon is present in all steels. In the stainless steels, in addiction to C-Mn steels and low alloy structural steels, it is usually desirable to control carbon below 0.1 wt%. The exception of stainless steels, are the martensitic grades, where carbon is critical for the transformation strengthening of these alloys. In the solid solution, carbon provides an interstitial strengthening effect, particularly at elevated temperatures.

In most alloys, carbon combines with other elements to form carbides. When, the most common, Cr-rich $M_{23}C_6$ carbide forms, a degradation of corrosion resistance occurs, and for this reason low-carbon (L-Grades) alloys are produces where the carbon content is kept below 0.04 wt%.

Nitrogen is considered to be an impurity element in most of the stainless steels, but it is an intentional addition to the some of the austenitic and almost all the duplex grades. Similar to carbon, nitrogen is a strong solid solution strengthening agent and even small additions of N can increase dramatically the strength of austenitic alloys. The strengthening effect of nitrogen in austenitic alloys is pronounced at cryogenic temperatures [9]. Nitrogen is added to the duplex grades not only to improve strength, but more important to increase resistance to pitting and crevice corrosion. For that reason some of the duplex grades contain up to 0.3 wt% nitrogen.

Carbon and nitrogen are the most potent of the austenite promoting elements and that is why their content levels should be controlled carefully in order to achieve the desired microstructure balance. Their content levels and their effect on the microstructure can be controlled with the addition of other elements that will form carbides (Nb, Ti) or nitrides (Ti, Al) and hence effectively neutralize their effect in the matrix. The desired levels of nitrogen are jeopardized during welding if proper precautions are not taken. The pickup of nitrogen from the atmosphere can occur if proper shielding gas flow is not present. Also, nitrogen loss during welding from high-nitrogen alloys can be a problem. For that reason, nitrogen is added sometimes in the shielding gas in order to balance the loss during welding.

2.3   Welding of Stainless Steel

The three most popular processes for welding stainless steels are shielded metal arc, gas tungsten arc and gas metal arc (including fluxed cored arc) welding; however, almost all welding processes can be used. Stainless steel, although they are considered to be very weldable, are slightly more difficult to weld than mild steels [10]. This

is due to the fact that the physical properties of stainless steels exhibit several differences from those of the mild steels. These differences are:
1. Lower melting temperature
2. Lower coefficient of thermal conductivity
3. Higher coefficient of thermal expansion
4. Higher electrical resistance

The above physical properties are not the same for all stainless steel grades. The metallurgical features are those that determine the physical properties and the weldability characteristics.

In generally, the weldability of martensitic stainless steels is affected greatly by hardenability that can result in cold working. Welded joints in ferritic stainless steels have low ductility as a result of grain coarsening that is related to the absence of allotropic phase transformation. The weldability of austenitic stainless steels is governed by their susceptibility to hot cracking, similar to other single-phase alloys with a FCC structure [11].

2.3.1 Welding Processes

As noted before, the common grades of stainless steel can readily be joined by arc, electron beam, laser beam, resistance and friction welding processes. Gas metal arc, gas tungsten arc, flux cored arc and shielded metal arc welding are commonly used. Plasma arc and submerged arc welding are also suitable methods. The welding processes available for specialty grades are more limited due to the effects of these alloys individual metallurgical characteristics on their weldability.

2.3.1.1   Shielded Metal Arc Welding (SMAW)

The shielded metal arc welding process (Figure 2.1) uses an electric arc between a flux-covered metal electrode and the base metal (metal being welded). Heat from the electric arc melts both the end of the electrode and the base metal to be joined. This process is often used for maintenance work and small production welding. Heavy pipe welding is done almost exclusively with shielded metal arc welding.

Equipment used in this welding process provides an electric current, which may be either alternative current (ac) or direct current (dc). Current adjustment controls on the welding machine allow the welder to set the desired current. The movement of the hand-held electrode holder is controlled exclusively by the welder. The heat of the electric arc may be controlled by the current setting and by the arc length. The electrode diameter and the flux material will determine the type (ac or dc) and the amount of the welding current required. The electrode used is a flux-covered metal wire. The flux that covers the electrode plays a multipart role in the whole process:
A. *Protection.* It provides a gaseous shield to protect the molten metal from air. For a cellulose-type electrode, the covering contains cellulose. A large mixture of gas mixture of H_2, CO,

H_2O and CO_2 is produced when cellulose in the electrode is heated and decomposes. For a limestone-type electrode, on the other hand, CO_2 gas and CaO slag form when the limestone decomposes. The limestone-type electrode is a low-hydrogen-type electrode because it produces a gaseous shield low in hydrogen. It is often used for welding metals that are susceptible to hydrogen cracking.

B. *Deoxidation.* It provides deoxidizers and fluxing agents to deoxidize cleanse the weld metal. The solid slag formed also protects the already solidified but still hot weld metal from oxidation.

C. *Arc Stabilization.* It provides arc stabilizers to help maintain a stable arc. The arc is an ionic gas (plasma) that conducts the electric current. Arc stabilizers are compounds that decompose readily into ions in the arc, such as potassium oxalate and lithium carbonate. They increase the electrical conductivity of the arc and help the arc conduct the electric arc more smoothly.

D. *Metal Addition.* It provides alloying elements and/or metal powder to the weld pool. The alloying additions help control the composition of the weld metal while the powder increases the deposition rate.
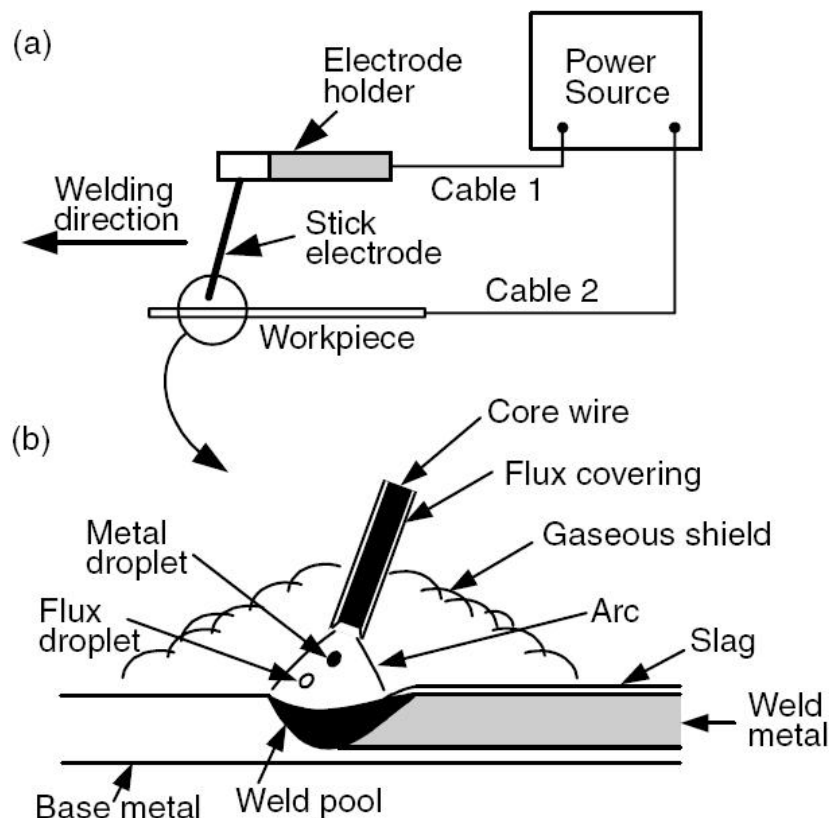
Figure 2.1 Shielded Metal Arc Welding Process a) Overall Process and b) Welding area [6]

2.3.1.2   Gas Tungsten Arc Welding (GTAW)

The gas tungsten arc welding process (Figure 2.2) uses an electric arc, established by a non-consumable tungsten electrode and the base metal, to join the metal being welded. A separate welding filler rod is fed into the molten base metal, if needed. The torch holding the tungsten electrode is connected to a shielding gas cylinder and to one of the terminal of the power source. The tungsten electrode is usually in contact with a water-cooled copper tube, called the contact tube, which is connected to the terminal as well. This allows both the welding current to enter the electrode and the electrode to be cooled to prevent overheating.
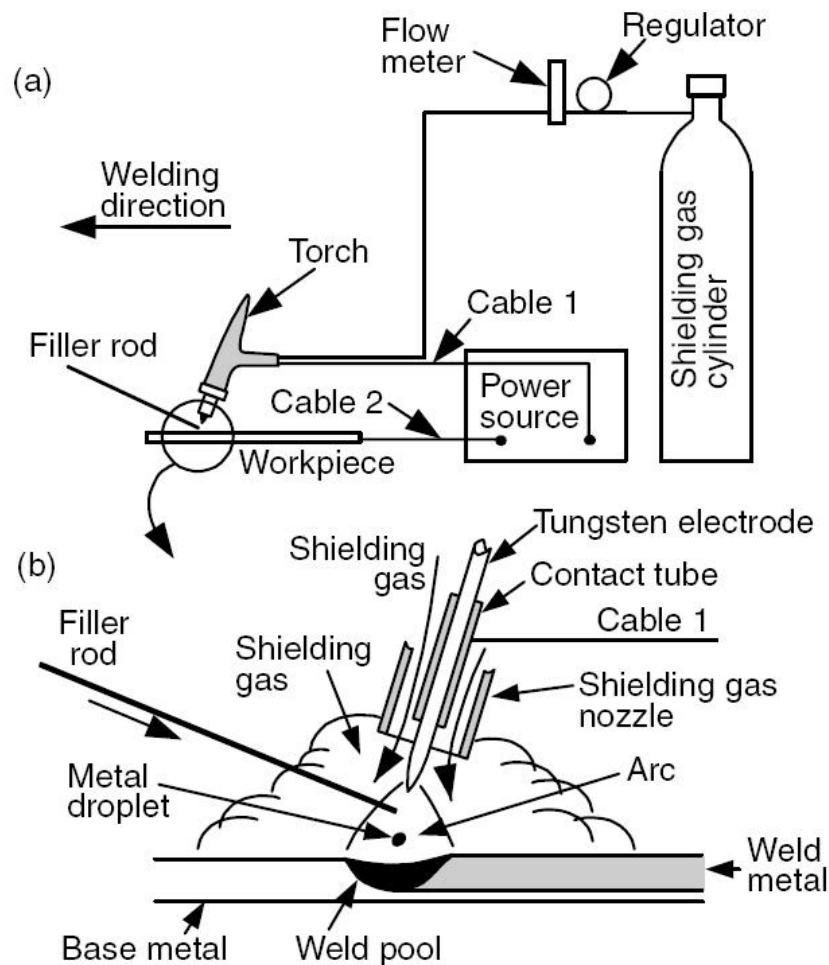
Figure 2.2 Gas Tunsten Arc Welding Process a) Overall Process and b) Welding area [6]

The workpiece is connected to the other terminal of the power source through a different cable. The shielding gas goes through the torch body and is directed by a nozzle toward the weld pool to protect it from the surrounding atmosphere. The gaseous protection in GTAW is much better than SMAW, because an inert gas, such as argon or helium, in usually used as the shielding gas and because the shielding gas is directed toward the weld pool.

In the GTAW process three different polarities can be achieved. The current being used may be AC or DC, where DC is subdivided according to the electrode polarity (negative or positive). In a more detailed description the polarities are:

a. *Direct Current Electrode Negative (DCEN)*. This, also called straight polarity, is the most common polarity in GTAW. With DCEN, the amount of power located in the work piece is more than the one at the end of the electrode. In this way a relatively narrow and deep weld pool is produced (Figure 2.3a)

b. *Direct Current Electrode Positive (DCEP)*. This is also called reverse polarity. Consequently, with DCEP, more power will be located at the electrode, which is why water-cooled electrodes must be used, and less penetration of the weld metal will be achieved (Figure 2.3b). Also, positive ions of the shielding gas will bombard the base metal knocking off oxide films and producing a clean weld surface.

c. *Alternative Current (AC)*. As illustrated in Figure 2.3c, reasonably good penetration and oxide cleaning action can be obtained.
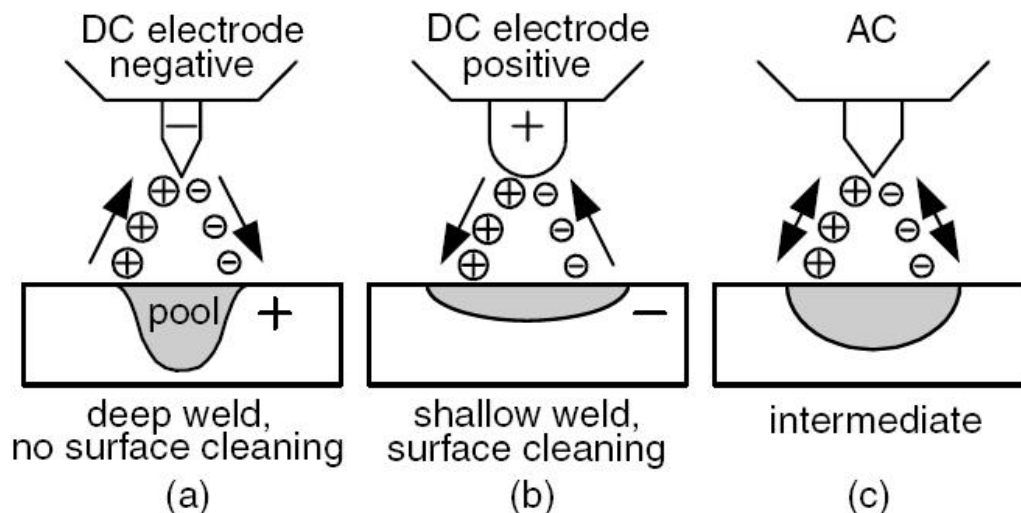
Figure 2.3 Three different polarities in GTAW a) *DCEN*, b) *DCEP,* c) *AC* [6]

As shielding gases, both argon and helium can be used in the GTAW process. The ionization potentials fro argon and helium are 15.7 and 24.5 eV, respectively. Since it is easier to ionize argon than helium, arc initiation is easier and the voltage drop across the arc is lower with argon. Also, argon is heavier than helium, offering a more effective shielding in the weld pool. These advantages, plus the lower cost of argon, make it more attractive for GTAW than helium.

However, due to the greater voltage drop across a helium arc than an argon arc, higher power inputs and greater sensitivity to variations on the arc length can be obtained with helium. Higher power allows the welding of thicker sections and the use of higher

welding speeds, while greater sensitivity to arc variations allows a better control of the arc length during automatic GTAW.

2.3.1.3   Gas Metal Arc Welding (GMAW)

In this process, metals are melted and joined together with an arc established between them and a continuously fed filler wire electrode, as shown in Figure 2.4. Shielding of the arc and the molten weld pool is often obtained by using inert gases, such as argon and helium, or mixtures of inert and active gases. Active gases, which are used as additions, are CO_2 and O_2.
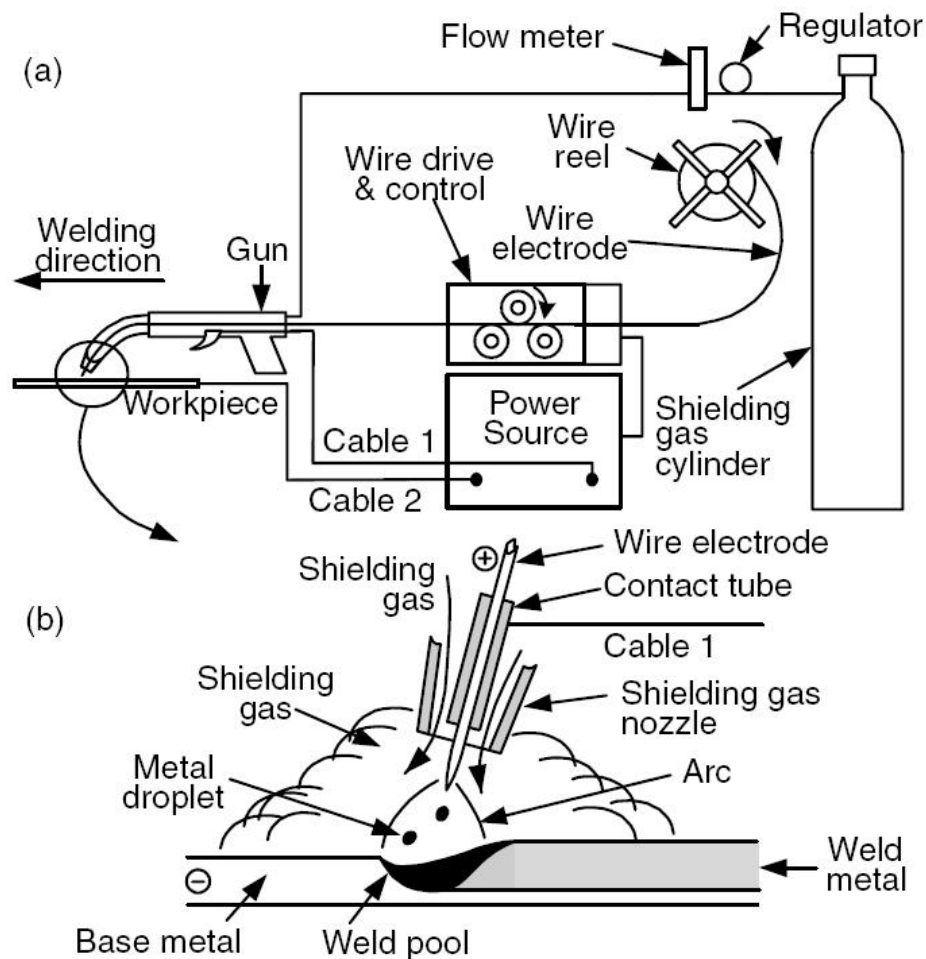
Figure 2.3 Gas Metal Arc Welding Process a) Overall Process and b) Welding area [6]

In general, argon, helium and their mixtures are used for nonferrous metals as well as stainless and alloy steels. The arc energy is less uniformly dispersed in an Ar arc than in a He arc because of the lower thermal conductivity of Ar. Consequently, the Ar arc plasma has a very high energy core and an outer mantle of lesser thermal energy. This helps produce a stable, axial transfer of metal droplets. The resultant weld transverse cross section exhibits good penetration but reduced width. With pure He shielding, on the other hand, a broad, parabolic-type penetration is often observed.

With ferrous metals, however, helium shielding may produce spatter and argon shielding may cause undercutting at the fusion lines. Adding O_2 (≥9%) and CO_2 (≥20%) in Argon shielding gas reduces these problems.

Shielding gas is, also, one of the factors that determine the way of metal transfer in gas metal arc welding. The liquid droplets of the filler metal can be deposited in the weld pool in several ways. The three basic ways of the weld metal deposition are:

A. *Short Circuit Transfer.* The molten metal at the electrode tip is transferred to the weld pool when it touches the pool surface, that is, when short circuiting occurs. Short-circuiting transfer encompasses the lowest range of welding currents and electrode diameters. It produces a small and fast-freezing weld pool that is desirable for welding thin sections, out-of-position welding (like overhead welding) and bridging large root openings.

B. *Globular Transfer.* Discrete metal drops close to or larger than the electrode diameter travel across the arc gap under the influence of gravity. Globular transfer often is not smooth and produces spatter. At relatively low welding current globular transfer occurs regardless of the type of the shielding gas. With CO_2 and helium, however, globular transfer mode occurs in all usable welding currents.

C. *Spray Transfer.* Above a critical current level, small discrete metal drops travel across the arc gap under the influence of electromagnetic force at much higher frequency and speed than in the globular mode. Here, the metal transfer is much more stable and spatter free. The critical current level depends on the material and size of the electrode and the composition of the shielding gas.

The factors that determine type of the metal transfer are:
1. The Magnitude and Type of the Welding Current
2. The Electrode Diameter
3. The electrode Composition
4. The Electrode Extension, and
5. The Shielding Gas

2.3.1.4   Flux Cored Arc Welding (FCAW)

The Flux Cored Arc Welding process (Figure 2.4) is similar to the GMAW process. The same concept covers both welding methods. The only difference lies in the filler metal being used. In the GMAW process a solid metal wire, of similar composition with the base metal, is used to establish an arc between its tip and the base metal being welded. In the FCAW process, the wire, which is used, contains in its core a flux, similar to the flux that surrounds the shielded electrodes of the SMAW process.

The purpose of the flux is to provide extra shielding in the welding pool and the weld metal and to function as a heat insulator on the weld pool surface, increasing the heat flow rate, resulting to higher welding speed. The use of the FCAW process has increased due to the advantages that exhibit in comparison to the GMAW process. Most of the welding of stainless steel is done with the use of the FCAW process.
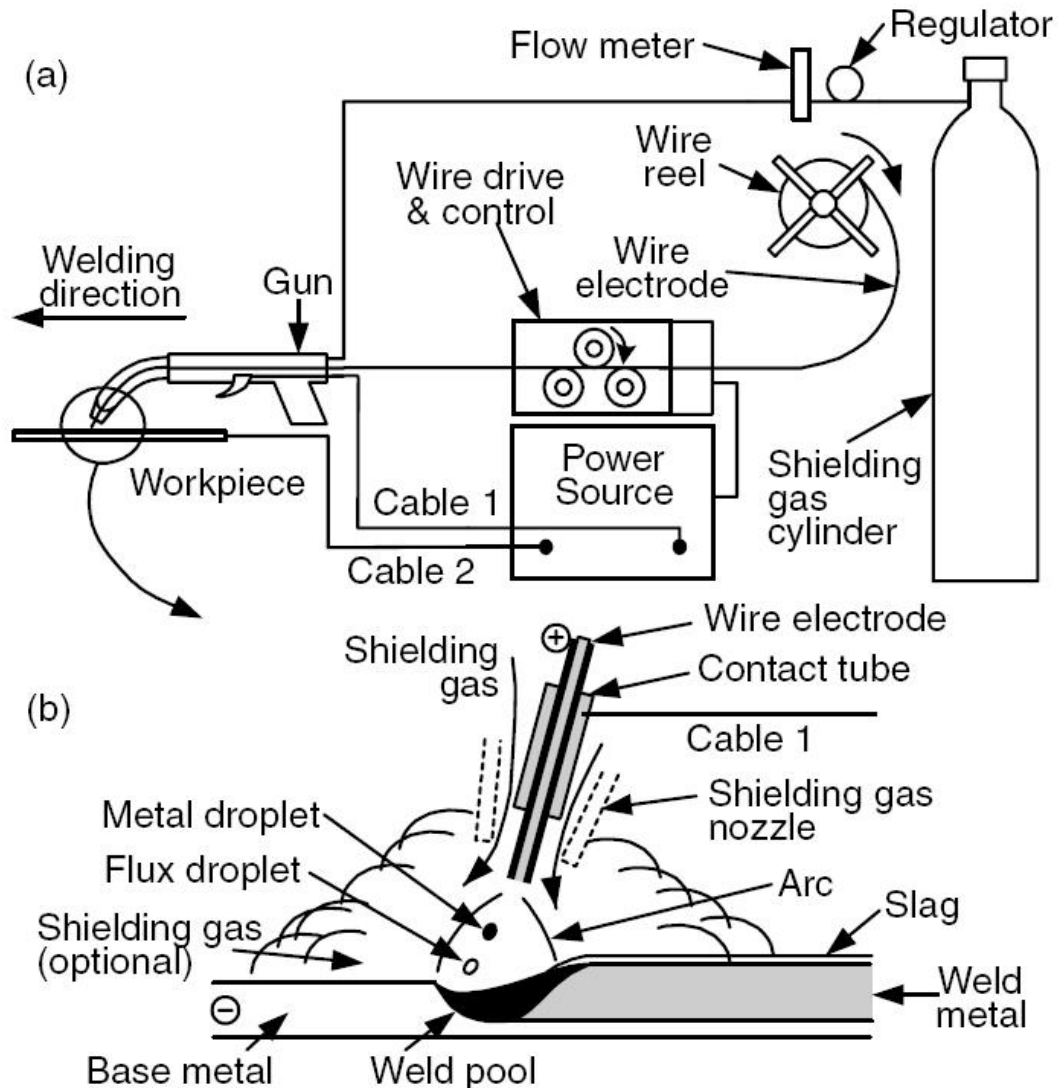

Figure 2.4 Flux Cored Arc Welding Process a) Overall Process and b) Welding area [6]

2.3.1.5 Submerged Arc Welding (SAW)

The Submerged Arc Welding process (Figure 2.5) produces coalescence of metals by heating them with an arc, established between a bare metal electrode and the base metal. The arc and the weld pool are "submerged" in a blanket of granular fusible flux. The filler metal is obtained from the electrode and sometimes from a

supplemental source such as a metal rod, or metal granules, or additional wire electrode.
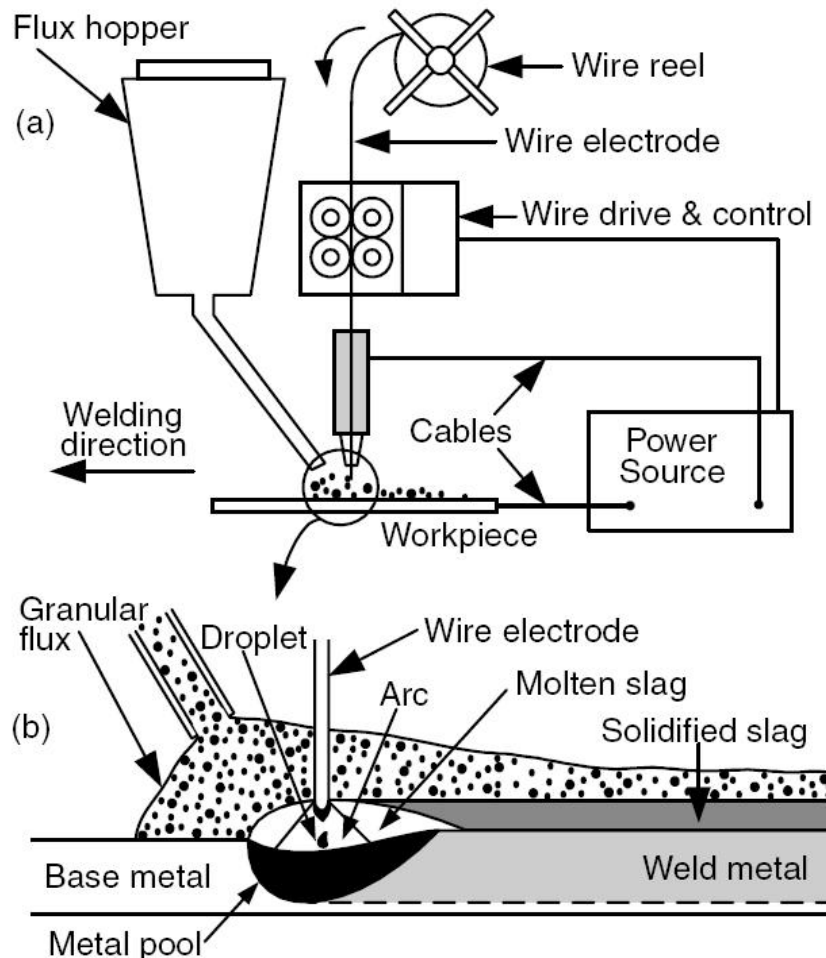
Figure 2.5 Submerged Arc Welding Process a) Overall Process and b) Welding area [6]

The flux that covers the weld pool contributes in many ways to the process. Beside the role of shielding, the flux stabilizes the arc and depended on the flux-composition, mechanical and metallurgical properties of the weld can be determined. Finally, the quality of the weld may be affected by the handling and care of the flux.

Submerged arc welding is a versatile production welding process capable of making welds with currents up to 2000 amperes, ac or dc, using single or multiple wires or strips of filler metal. Both ac and dc power sources may be used on the same weld at the same time.

2.3.1.6   Laser Beam Welding (LBW)

Laser Beam Welding (LBW) process, shown in Figure 2.6, is a fusion joining process that produces coalescence of materials with the heat, obtained from a concentrated beam of coherent, monochromatic light impinging on the joint to be welded.

In the LBW process, the laser beam is directed by flat optical elements, such as mirrors, and then focused to a small spot (for high-power density) at the workpiece using either reflective focusing elements or lenses. LBW is a noncontact process, and thus requires that no pressure be applied. Inert gas is generally employed, as shielding, to prevent oxidation of the molten puddle and filler metal may occasionally be used.

The lasers predominantly being used for industrial material processing and welding tasks are the 1.0 µm YAG laser and the 10.6 µm CO_2 laser, with the active element most commonly employed in these two varieties of lasers being the neodymium (Nd) ion and the CO_2 molecule (respectively).
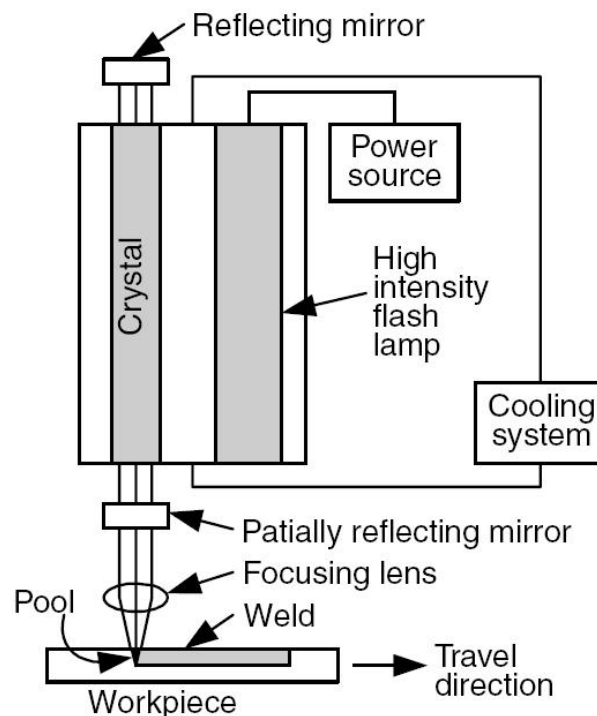
Figure 2.6 Laser Beam Welding (LBW) Process [6]

The LBW process is enlisted, along with EBW (Electron Beam Welding), in the high-power welding processes. LBW incorporates its unique characteristics to provide heat input, close to the minimum required, to fuse the weld metal; thus, metallurgical effects in the heat affected zone are reduced and heat-induced workpiece distortion in minimized. In addition, single pass laser procedures have been qualified in materials of up to 32 mm thick, thus reducing the time to weld thick sections and the need for filler wire to be eliminated. Laser beams are readily focused, aligned and directed by optical elements. Thus the laser can be located at a convenient distance from the workpiece and redirected around tooling and obstacles in the workpiece. This permits welding in areas not easily accessible with other means of welding. In addition, the laser can be readily

mechanized for automated, high-speed welding, including numerical and computer control.

LBW, as a process, has some limitations. Joints must be accurately positioned under the beam and at a controlled position with respect to the beam focal point. The process demands accuracy mostly in thick sections, due to the fact that the weld penetration can easily miss the joint. Thus, weld penetrations of much greater than 19 mm are not considered to be practical production LBW applications.

2.3.2 Welding Process Suitability

As noted before, austenitic stainless steel can be readily welded by arc, laser beam, electron beam and friction welding processes. The GMAW, SMAW, FCAW and GTAW processes are the most commonly used, while plasma and submerged arc welding are also suitable joining methods. Sound welds can be produced by the use of SAW techniques, but certain restrictions may need to be placed on the process. Generally, the composition of the weld metal deposited, in this process, is more difficult to control than that produced with the other arc welding processes because of the effect of arc voltage variations on element pickup from fluxes and potentially high levels of dilution.

2.4 Welding Metallurgy of Austenitic Stainless Steels

Austenitic stainless steels are formulated and thermo-mechanically processed in such way, that their microstructure is primarily austenite. Depending on the balance of ferrite-promoting elements to austenite-promoting elements, the wrought or cast microstructure will be either fully austenitic or a mixture of austenite and residual ferrite. In order to observe the fully austenitic and the mixture of austenitic and ferritic microstructure, two wrought austenitic stainless steels are shown in Figure 2.7. In case (a) the microstructure consists of austenitic grains and in case (b), some residual high-temperature ferrite (δ-ferrite) is aligned along the rolling direction. These ferrite stringers can result from the ferrite-promoting element segregation (primarily chromium) during solidification and thermo-mechanical processing (rolling). It is usually present in relatively low fraction volume (less than 2 to 3 %).
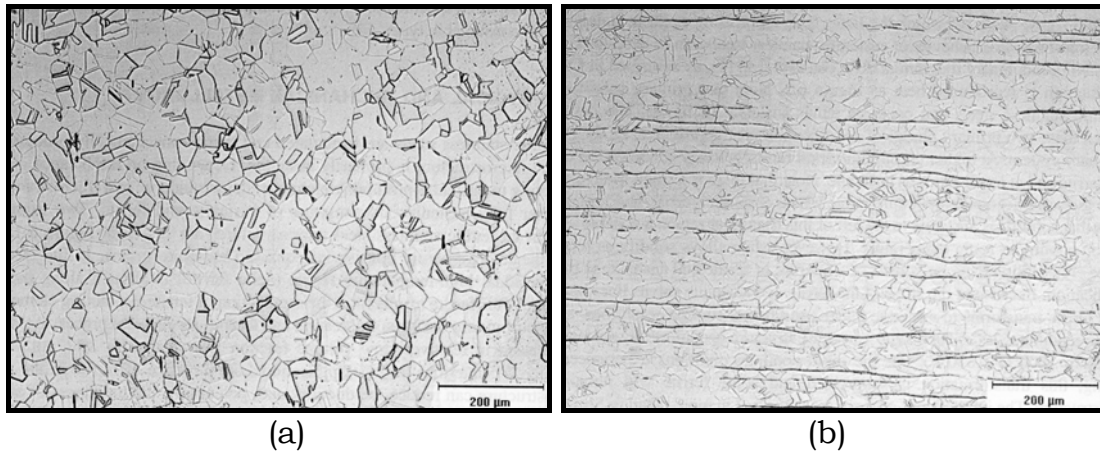
(a)   (b)

Figure 2.7 Microstructure of Type 304 a) fully austenitic and b) austenite with δ-ferrite stringers

The presence of δ-ferrite in the austenitic microstructure of wrought austenitic stainless steels can reduce the ductility and, potentially, the toughness of austenitic stainless steels. It can also be a preferential site for the precipitation of $M_{23}C_6$ carbides and σ-phase, which is an embrittling agent in stainless steels.

The description of the transformation behavior of austenitic stainless steels can be achieved with the use of the Fe-Cr-Ni pseudo-binary diagram, at 70% constant iron, which can be seen in Figure 2.8 [10].
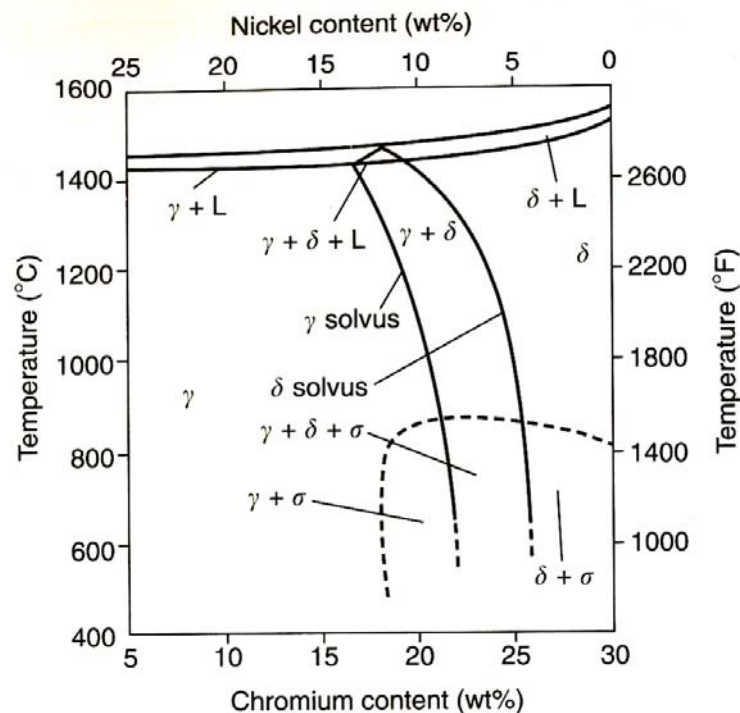
Figure 2.8 Pseudo-binary section of the Fe-Cr-Ni system at 70% iron [10]

The primary solidification can occur as either austenite or ferrite. The boundary of these two primary phases of solidification is

approximately at 18Cr-12Ni in the respective ternary system. At lower chromium/nickel ratios, primary solidification occurs as austenite and at higher ratios as δ-ferrite. In the pseudo-binary diagram, a small triangular area can be seen, where austenite, ferrite and liquid coexist. Alloys, which solidify on the left of this triangular area, are stable as austenitic upon cooling at room temperature. However, when alloys solidify as ferrite, they can be fully ferritic or a mixture of ferrite and austenite (duplex grades) at the end of solidification. The reason for this is the slope of the solvus lines of ferrite and austenite. Most or all the ferrite transforms to austenite upon cooling, and for the rapid cooling conditions, that experience during welding, this transformation is suppressed and some residual ferrite will remain in the alloy microstructure at the end. The effect of other alloying elements on the phase equilibrium in austenitic stainless steels can be determined using phase diagrams generated using computational thermodynamics, such as Thermo-Calc ™ [11].

Depending on the microstructure and heat treatment of the austenitic alloy, a variety of precipitates may form in the alloy. A list of those precipitates, their structure and stoichiometry is given in Table 2.3 [1].

Table 2.3 Precipitates in Austenitic Stainless Steels [1]

Precipitate	Crystal Structure	Lattice Parameters (nm)	Stoichiometry
MC	FCC	$a = 0.424–0.447$	TiC, NbC
M_6C	Diamond cubic	$a = 1.062–1.128$	$(FeCr)_3Mo_3C$, Fe_3Nb_3C, Mo_5SiC
$M_{23}C_6$	FCC	$a = 1.057–1.068$	$(Cr,Fe)_{23}C_6$, $(Cr,Fe,Mo)_{23}C_6$
NbN	FCC	$a = 0.440$	NbN
Z phase	Tetragonal	$a = 0.307, c = 0.7391$	CrNbN
Sigma phase	Tetragonal	$a = 0.880, c = 0.454$	Fe–Ni–Cr–Mo
Laves phase (η)	Hexagonal	$a = 0.473, c = 0.772$	Fe_2Mo, Fe_2Nb
Chi phase (χ)	BCC	$a = 0.8807–0.8878$	$Fe_{36}Cr_{12}Mo_{10}$
G phase	FCC	$a = 1.12$	$Ni_{16}Nb_6Si_7$, $Ni_{16}Ti_6Si_7$
R	Hexagonal	$a = 1.0903, c = 1.9342$	Mo–Co–Cr
	Rhombohedral	$a = 0.9011 \, \alpha = 74°27.5'$	Mo–Co–Cr
ε Nitride (Cr_2N)	Hexagonal	$a = 0.480, c = 0.447$	Cr_2N
Ni_3Ti	Hexagonal	$a = 0.9654, c = 1.5683$	Ni_3Ti
$Ni_3(Al,Ti)$	FCC	$a = 0.681$	Ni_3Al

Carbides are present in, virtually, all stainless steels, since chromium is a strong carbide former. Carbide formation is also promoted with the addition of other carbide formers, such as Mo, Nb and Ti. The nature of carbide formation, including the effect of composition and the temperature range of formation is quite complex.

As noted before the room-temperature microstructure of the fusion zone of austenitic stainless steels is depended both on the solidification behavior and subsequent transformations. All stainless steels solidify with either ferrite or austenite as the primary phase.

The austenitic stainless steels may solidify as primary ferrite or primary austenite, depending on the specific composition. Even small changes in the alloys composition are enough to change the solidification mode from austenite to ferrite or conversely. The composition range of the austenitic grades is broad enough, so that both solidification modes are possible.

Following the solidification process, additional transformations can occur in the solid state upon cooling to ambient temperature. These transformations are most important in the austenitic alloys undergoing primary ferrite solidification, since most of the ferrite will transform to austenite.

2.4.1 Fusion Zone Microstructure Evolution

In the fusion zone of the austenitic stainless steels welds, solidification can occur in four possible modes [12, 13]. These modes depend on the solidification and the solid-state transformation of the austenitic grades, and they are listed in Table 2.4. Solidification modes A and AF are associated with primary austenite solidification, since austenite is the first phase to form upon cooling. On the other hand, FA and F modes have δ-ferrite as the primary phase that forms first. Following the cooling processes additional solid state transformations occur in the FA and A mode, due to the instability of δ-ferrite at lower temperatures.

Table 2.4 Solidification Modes, Reactions and Final Microstructure [1]

Solidification Mode	Reaction	Microstructure
A	$L \rightarrow L + A \rightarrow A$	*Fully Austenitic*
AF	$L \rightarrow L + A \rightarrow$ $L + A + (A + F)_{eut} \rightarrow$ $A + F_{eut}$	*Ferrite at cell and dendrite boundaries*
FA	$L \rightarrow L + F \rightarrow$ $L + F + (F + A)_{per/eut} \rightarrow$ $F + A$	*Skeletal and/or lathy ferrite resulting from ferrite to austenite transformation*
F	$L \rightarrow L + F \rightarrow F \rightarrow$ $F + A$	*Acicular ferrite or ferrite matrix with grain boundary austenite and Windmastätten side plates*

The solidification modes of austenitic stainless steels upon cooling have also been associated with the Cr_{eq}/Ni_{eq} ratio, where the values of the equivalents, though determined by the WRC-1992 and Schaeffler diagrams, slightly vary amongst several researchers. However, from the recent work of Ferrandini et a. [15] and Ma et a. [16] the equivalent ration defines the solidification modes as presented in Table 2.5.

Table 2.5 Cr_{eq}/Ni_{eq} ratio and solidification mode association

Solidification Mode	Equivalent ratio
A - Fully Austenitic	$Cr_{eq}/Ni_{eq} < 1.25$
AF - Austenitic Ferritic	$1.25 < Cr_{eq}/Ni_{eq} < 1.48$
FA - Ferritic Austenitic	$1.48 < Cr_{eq}/Ni_{eq} < 1.95$
F - Ferritic	$1.95 < Cr_{eq}/Ni_{eq}$

The four solidification modes can also be observed on the pseudo-binary Fe-Cr-Ni diagram in Figure 2.10 (at 70 wt% Fe), which was discussed earlier.
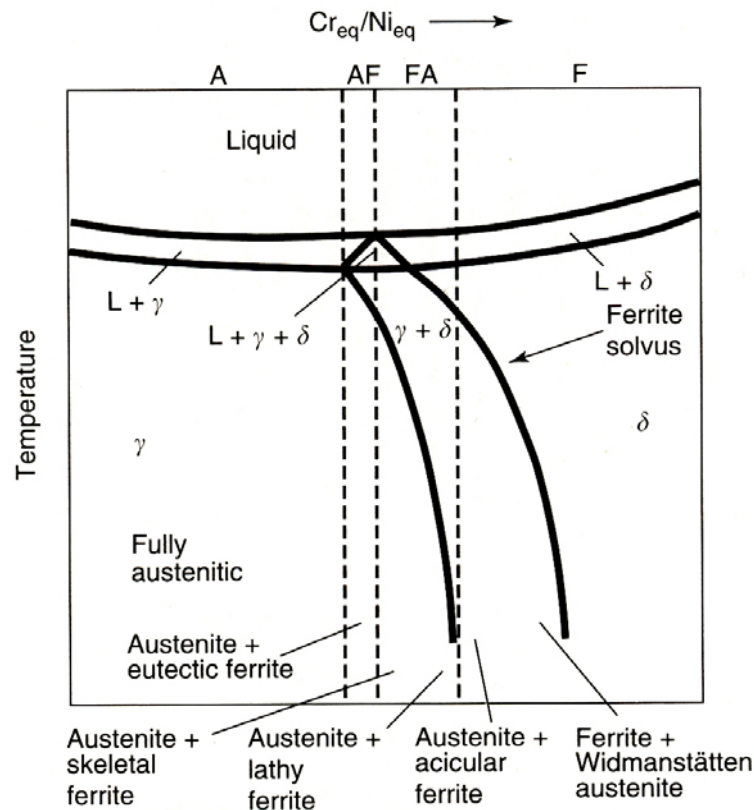
Figure 2.10 Solidification modes on the pseudo-binary phase diagram [1]

The various microstructures that are possible in the austenitic stainless steels are described separately in the following sections.

2.4.1.1   Type A: Fully Austenitic Solidification

When solidification occurs as primary austenite, two weld metal microstructures are possible. Hence, if the microstructure is fully austenitic at the end of the solidification, it shall remain austenitic upon cooling to room temperature. This solidification is termed *Type A solidification* and it is presented in Figure 2.11(a) schematically, while in Figure 2.12, the fusion zone, with Type A, of an austenitic stainless steel is presented metallographically. A characteristic of the solidification as primary austenite is that the solidification substructure (cells and dendrites) is clearly visible. This is due to the

segregation of alloying and impurity elements that occurs during solidification.

(a)   (b)
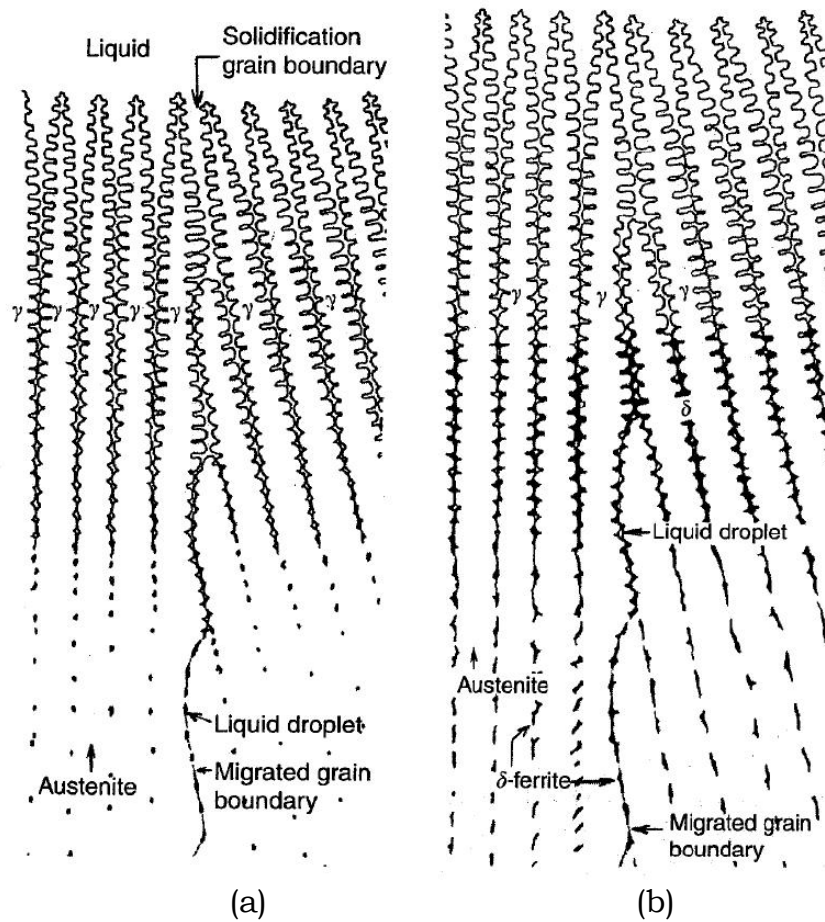
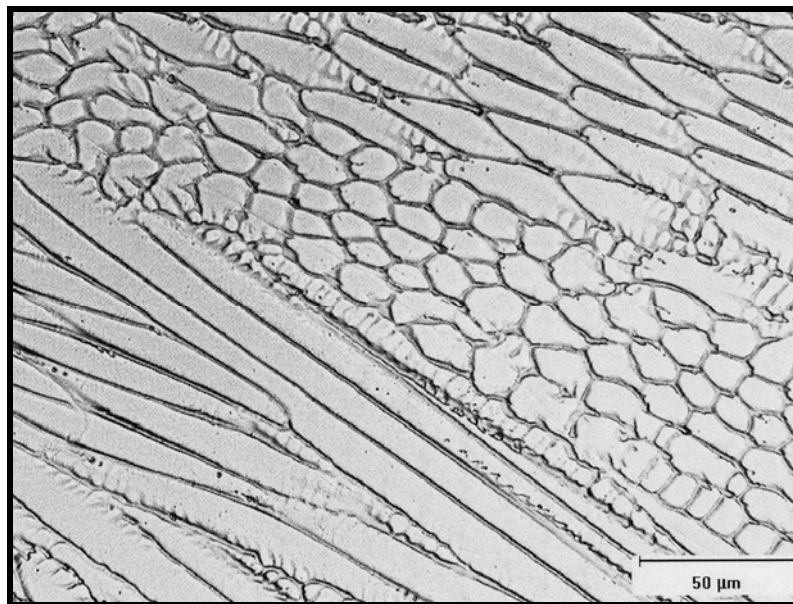**Figure 2.11** Schematically representation of a) Type A and b) Type AF solidification Mode [17]

Figure 2.12 Microstructure of fusion zone resulting from fully austenitic solidification [1]

The relatively low diffusivity of these elements at melting temperatures preserves the segregation profile, which develops during solidification. It has been observed that when alloys such as Type 304 and 316 solidify as Type A, Cr and Mo have been shown to partition to the cell and dendrite boundaries.

2.4.1.2   Type AF Solidification

At the end of the primary austenite solidification process, if some ferrite forms via a eutectic reaction, then the solidification is termed *Type AF solidification* and it is resented schematically in Figure 2.11(b). This occurs if sufficient ferrite-promoting elements, primarily Cr and Mo, partirion to the solidification subgrain boundaries during the whole solidification process, in order to promote the formation of ferrite as a terminal solidification product.

The ferrite that forms along the austenitic grain boundaries is relatively stable and capable to resist to austenite transformation during weld cooling, since it is enriched in ferrite–promoting elements. An example of the microstructure that exhibits ferrite along subgrain boundaries is presented in Figure 2.13, where the solidification substructure is readily apparent, due to the primary austenite solidification.
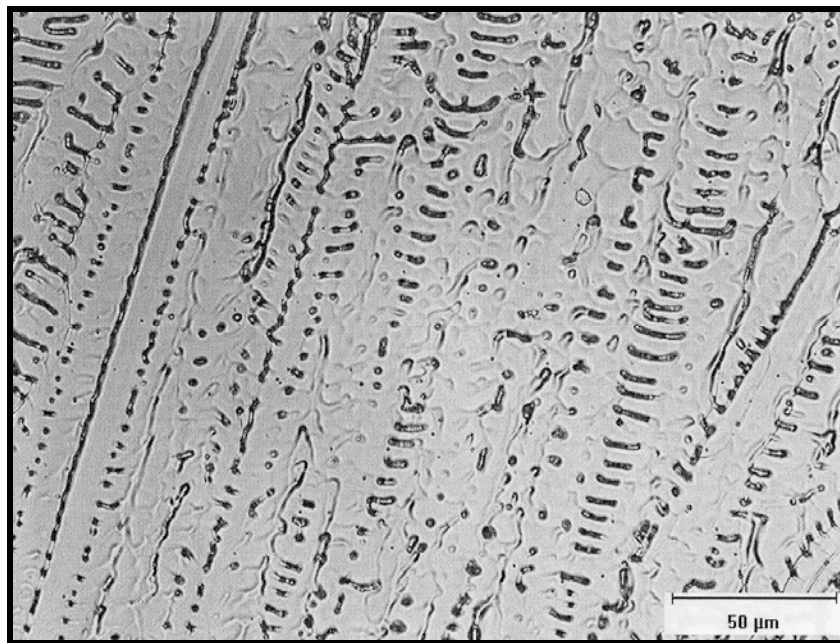
Figure 2.13 Microstructure of fusion zone resulting from Type AF solidification [1]

2.4.1.3   Type FA Solidification

Similar to the previous solidification modes, when solidification occurs as primary ferrite, there are also two possibilities. One possibility is when some austenite forms at the end of the process, thus the solidification is termed *FA Type*. This austenite forms via a

peritectic-eutectic reaction and exists at the ferrite solidification boundaries at the end of solidification. The peritectic-eutectic reaction has been studied extensively by many researchers in order to determine the solidification and transformation sequence that occurs to give rise to the ferrite morphologies resulting from FA solidification.

The above reaction occurs within and along the three-phase triangular region shown in Figure 2.10, and it is called peritectic-eutectic, because it is composition dependent and results from a transition from a peritectic reaction in the Fe-Ni system to a eutectic reaction in the Fe-Cr-Ni system. When the solidification is complete, the microstructure consists of primary ferrite dendrites with an interdendritic layer of austenite. The amount of austenite that is present depends on the solidification conditions and the Cr_{eq}/Ni_{eq} ratio. As the ratio increases, the amount of austenite decreases until solidification becomes entirely ferritic and shifts from FA to F solidification Type.

As the weld metal cools through the two-phase, δ-ferrite and austenite, field, the ferrite becomes increasingly unstable and the austenite begins to consume the ferrite via a diffusion-controlled reaction [1]. The final microstructure of the weld metal is depended on the cooling rates.

- When weld cooling rates are moderate, and/or the Cr_{eq}/Ni_{eq} is low but still within the FA range, a vermicular or skeletal ferrite (Figure 2.14(a)) morphology results. This is a consequence of the advance of the austenite consuming the ferrite until the ferrite is sufficiently enriched in ferrite-promoting elements and depleted in austenite-promoting elements that it is stable at lower temperatures where diffusion is limited. The skeletal morphology is shown in micrograph in Figure 2.15(a).

- When weld cooling rates are high, and/or Cr_{eq}/Ni_{eq} increases within the FA range, lathy ferrite morphology results (Figure 2.14(b)). The lathy morphology forms in place of the skeletal morphology due to restricted diffusion during the ferrite-austenite transformation. When diffusion distances are reduced it is more efficient for the transformation to proceed as more tightly spaced laths, resulting in a residual ferrite pattern that cuts across the original dendrite or cell growth direction. A metallographic presentation of the lathy ferrite morphology is presented in Figure 2.15(b).

- When solidification and cooling rates are extremely high, such as during laser or electron beam welding, a complete transformation from ferrite to austenite may be possible due to a diffusionless, "massive" transformation. A shift in primary solidification mode from ferrite to austenite may also occur at high solidification rates.

2.4.1.4   Type F Solidification

If solidification occurs completely as ferrite, it is termed Type F. in this case the microstructure is fully ferritic at the end of solidification, and when the metal cools below the ferrite solvus, austenite forms within the microstructure, usually first at the ferrite grain boundaries. The degree of transformation to austenite depends on the Cr_{eq}/Ni_{eq} and cooling rate, again. At low Cr_{eq}/Ni_{eq} values within the F mode range, the transformation begins at higher temperature, and at low to moderate cooling rates, much of the ferrite is consumed. With higher cooling rates, diffusion is suppressed and the austenite will not consume of the ferrite. Similar, if the Cr_{eq}/Ni_{eq} value is increased within the F mode range, the ferrite solvus is depressed and transformation will occur at lower temperatures. However, in both cases, weld metals with high ferrite contents will result.

The microstructure that forms as a result of Type F solidification in austenitic stainless steels again is a function of composition and cooling rate. At low Cr_{eq}/Ni_{eq} values within the F range an acicular ferrite structure (shown schematically in Figure 2.14(a)) will form within the ferrite grains. The continuous austenite networks are present at the prior ferrite grain boundaries and the acicular ferrite is no longer contained within the bounds of the original ferrite dendrites.

The structure is completely ferritic in the solid state before the transformation to austenite begins. When this structure cools below the ferrite solvus, austenite first forms at the ferrite grain boundary. But the transformation front breaks down and parallel needles of austenite form within the ferrite.

At higher Cr_{eq}/Ni_{eq} values, considering though the same cooling rate, the microstructure will consist of a ferrite matrix with grain boundary austenite and Windmanstätten austenite plates that nucleate at the grain boundary austenite or within the ferrite grains. A schematically representation of the microstructure is shown in Figure 2.14(b) and a micrograph in Figure 2.15.

In this case, transformation does not occur entirely across the ferrite grain. Initial austenite again forms at the ferrite grain boundary, but transformation across the entire grain is suppressed by lower diffusion rates and lower driving force (the equilibrium microstructure contains more ferrite). This can be clarified from the pseudo-binary diagram in Figure 2.10, where as Cr_{eq}/Ni_{eq} increases, the ferrite solvus decreases and the equilibrium ferrite content increases, thus reducing the driving force for the ferrite-to-austenite transformation and the temperature at which the transformation begins.
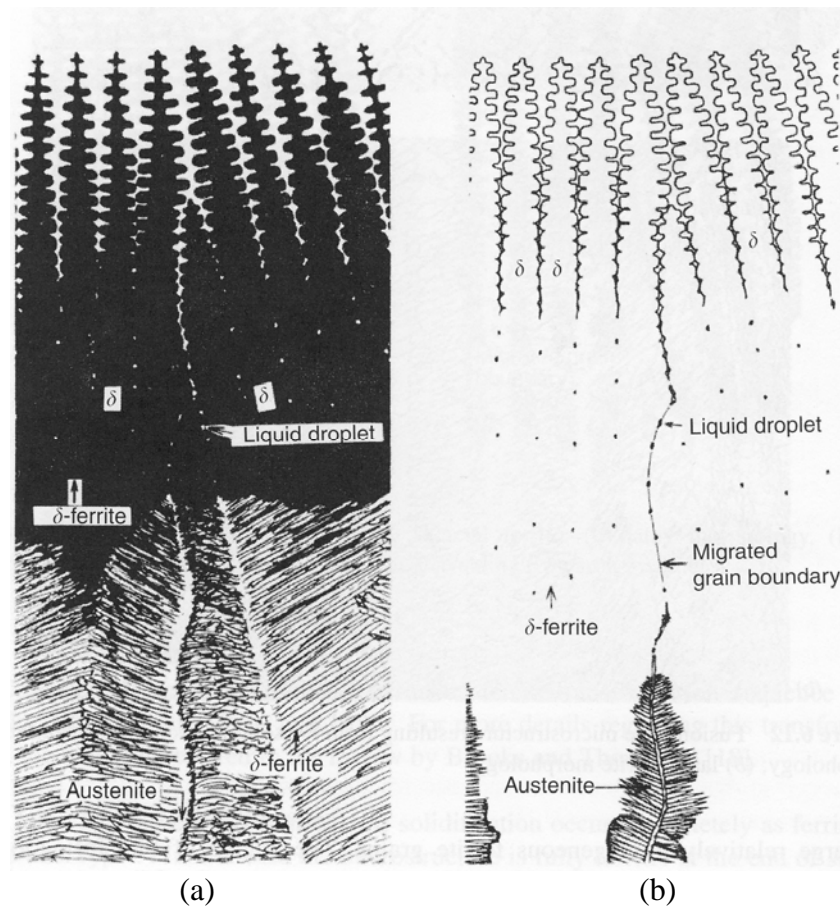
(a)   (b)

Figure 2.14 Schematic of Type F solidification: a) acicular ferrite b) ferrite and Windmanstätten austenite [17]
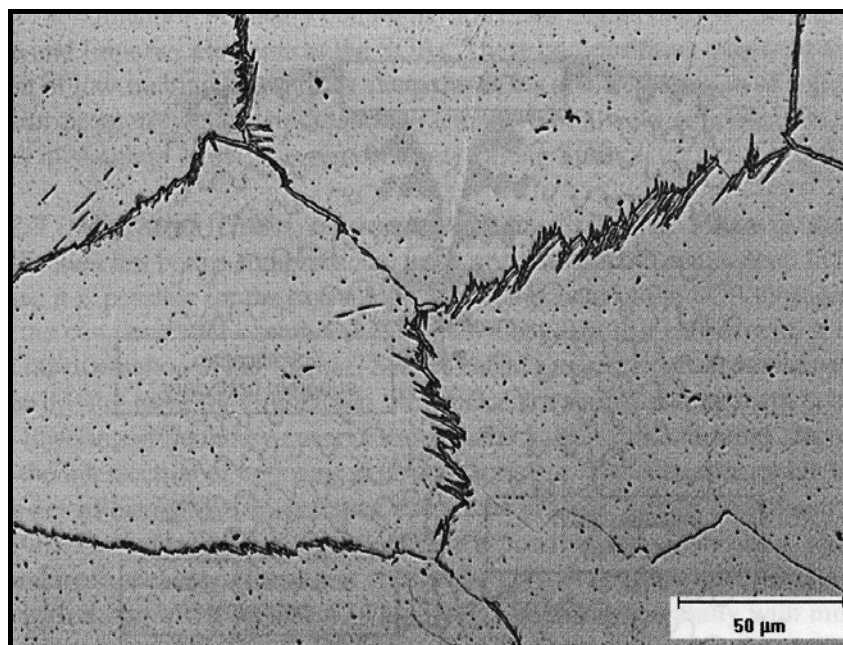

Figure 2.15 Fusion zone microstructure resulting from F solidification: Windmanstätten austenite nucleates from austenite along the ferrite grain boundaries [1]

In practice, Type F solidification is very unusual in austenitic stainless steel weld metals. Most filler metals are formulated such that solidification occurs in the FA mode, with weld metal ferrite content ranging from 5 to 20FN (Ferrite Number). Only highly alloyed filler metals, such as Type 309LMo, would be expected to exhibit microstructures with higher levels of ferrite. Type F solidification is more characteristic of the duplex stainless steels.

2.4.2 Interfaces in Single-Phase Austenitic Weld Metal

The importance of the discrimination along with the nature of the various boundaries, that are present in austenitic stainless steel weld metal, is crucial. Many of the defects associated with the fusion zone both during fabrication and in service are associated with these boundaries [1]. Boundaries are especially evident in weld metals that solidify in A or AF mode, since the solidification structure is clearly apparent after polishing and etching. At least three different boundary types can be observed metallographically and are shown schematically in Figure 2.16.
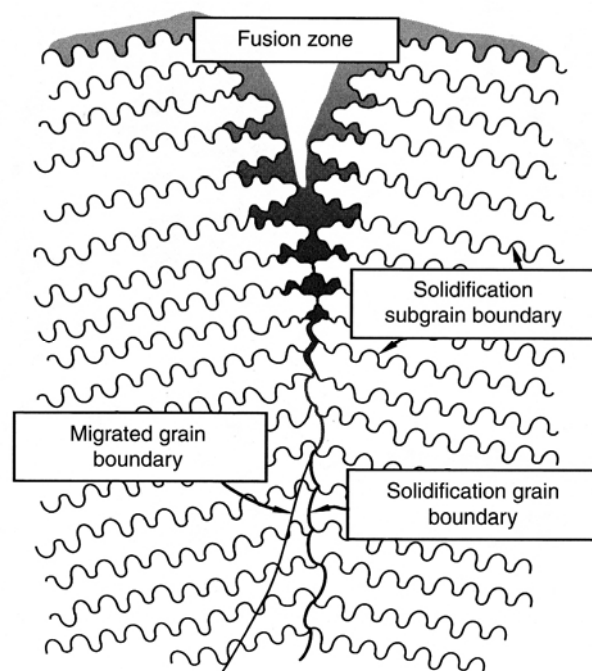
Figure 2.16 Schematic of boundaries observed in weld metals that solidify as primary austenite [1]

2.4.2.1   Solidification Subgrain Boundaries

The solidification subgrains represent the finest structure that can be resolved in the optical microscope. These subgrains are normally present as cells or dendrites and the boundary separating adjacent subgrains is known as a solidification subgrain boundary

(SSGB). These boundaries are evident in the microstructure because their composition is different from that of the bulk microstructure.

There is little crystallographic misorientation across the SSGB, and these boundaries are characterized crystallographically as low-angle boundaries. The low angular misorientation results from the fact that subgrain growth during solidification occurs along preferred crystallographic directions, which are easy growth directions.

2.4.2.2   Solidification Grain Boundaries

The solidification grain boundary (SGB) results from the intersection of packets, or groups, of subgrains. Thus, SGBs are the direct result of competitive growth that occurs during solidification along the trailing edge of the weld pool. Because each of these packets of subgrains has a different growth direction and orientation, their intersection results in a boundary with high angular misorientation. These are often called high-angle grain boundaries. This misorientation results in the development of a dislocation network along the SGB.

The SGB also exhibits a compositional component resulting from solute redistribution during solidification. This redistribution, often, results from in high concentrations of solute and impurity elements at the SGBs. These compositions may lead to the formation of low-melting liquid films along the SGBs at the conclusion of solidification that can promote weld solidification cracking. When weld solidification cracking occurs in stainless steels, it is almost always along SGBs.

2.4.2.3   Migrated Grain Boundaries

The SGB that forms at the end of solidification has both a compositional and a crystallographic component. In some situations, it is possible for the crystallographic component of the SGB to migrate away from the compositional component. This new boundary that carries with it the high-angle misorientation of the "parent" SGB is called a migrated grain boundary (MGB).

The driving force for migration is the same as for a simple grain growth in base metals, a lowering of boundary energy. The original SGB is quite tortuous since it forms from the intersection of opposing cells and dendrites. The crystallographic boundary can lower its energy by straightening and, in the process; it pulls away from original SGB. Further migration of the boundary is possible during reheating, such as during multipass welding. The composition of the boundary varies locally, depending on the composition of the microstructure where it has migrated.

Migrated grain boundaries are most prevalent in fully austenitic weld metals. When the weld metal undergoes AF solidification, ferrite forms at the end of solidification along the SSGBs and SGB. The ferrite, formed, is effective in constraining the crystallographic component of the SGB, thus preventing it from migrating away from

the parent SGB. An example of these interface types in a single-phase Type 304L fusion zone microstructure, is presented in Figure 2.17.
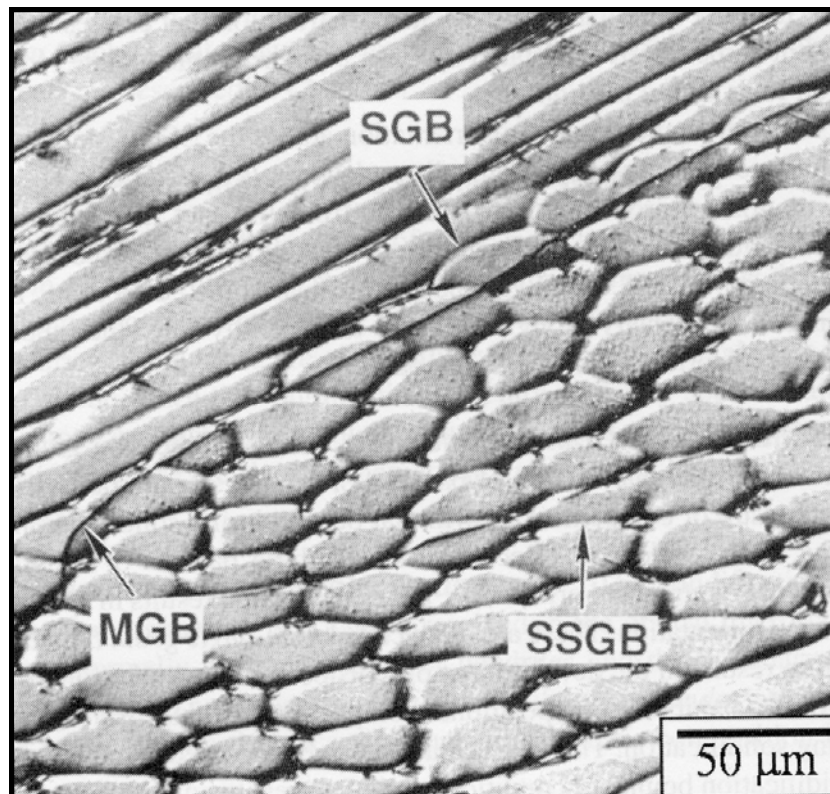

Figure 2.17 Fusion zone microstructure of Type 304L that has undergone Type A solidification [1]

When solidification occurs in the FA or F modes, SSGBs and SGBs also form but they are typically not apparent in the microstructure. This results for three reasons:

1. Segregation during ferrite solidification is not as pronounced as during austenite solidification.
2. Elevated temperature diffusion is much more rapid in ferrite relative to austenite (approximately by 100 times).
3. The ferrite-to-austenite transformation tends to mask any solidification segregation in the ferrite.

MGBs are also not typically, not observed in weld metals that solidify in FA or A modes. Although, they must be present, they are virtually impossible to distinguish from the ferrite-austenite interface.

2.4.3 Heat Affected Zone

The nature of the heat affected zone (HAZ) in austenitic stainless steels depends on the composition and the microstructure of the base metal. In this particular area, next to the fusion zone, some metallurgical reactions may occur. Some of them are the grain growth, the ferrite formation, precipitation of carbides and grain boundary liquation.

Most stainless steels are welded in the solution-annealed or hot-rolled condition, so grain growth is usually restricted unless weld heat inputs are extremely high. Some grain coarsening can usually be observed, but in most cases it is not dramatic. In base metals that have been strengthened by cold working, recrystallization and grain growth can result in significant HAZ softening. In this case, a distinct HAZ results and the grain size is clearly larger than of the base metal.

Regarding the ferrite formation in the HAZ, as shown in the pseudo-binary diagram in Figure 2.10, alloys whose compositions are to the right of the fully austenitic solidification range will form ferrite when heated to temperatures just below the solidus temperatures. The higher the Cr_{eq}/Ni_{eq} ratio of the alloy, the more likely ferrite formation will be. When ferrite forms, it is usually along the grain boundary, as shown in Figure 2.18. Formation of Ferrite along the HAZ grain boundaries will restrict grain growth and also minimize the susceptibility to HAZ liquation cracking. The degree of ferrite formation is usually low since the austenite-to-ferrite transformation is relatively sluggish and the HAZ thermal cycle is normally quite rapid. Also, there is the possibility that some of the ferrite that forms during elevated temperature exposure transforms back to austenite on cooling.
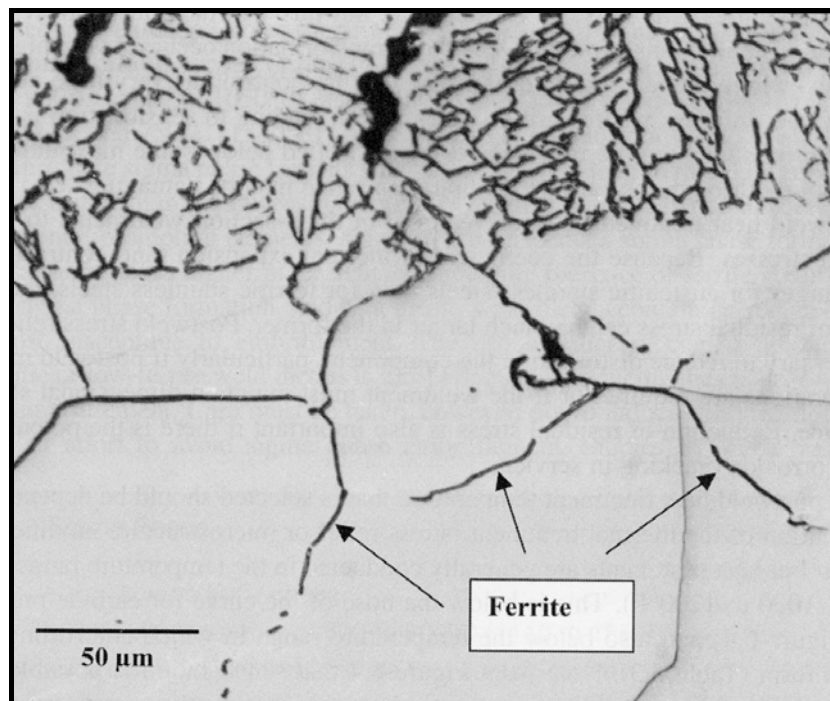
Figure 2.17 Ferrite along the austenite grain boundaries in the HAZ of Type 304L stainless steel [1]

The HAZ of the austenitic stainless steels can be heated up to temperatures approaching the solidus of the alloy, thus many of the precipitated that are present may dissolve. This can lead to a supersaturation of austenite matrix during cooling, resulting in the formation of various precipitates. Carbides and nitrides are the most likely precipitates to form in the HAZ of the austenitic stainless steels.

52

These precipitates will usually form along grain boundaries or, if ferrite is present, at the ferrite-austenite interface. Even though not apparent metallographically, it is likely that these precipitates will be present in the HAZ of most austenitic alloys. The precipitate size, distribution and morphology are depended on the alloy composition and the HAZ thermal cycle.

Another metallurgical reaction that can occur in the HAZ of austenitic stainless steels is the local melting along the austenite grain boundaries. This usually results from the segregation of impurity elements that reduce the grain boundary melting temperature. Alloys that contain titanium and niobium and that from MC carbides rich in these elements may undergo constitutional liquation, a phenomenon that can lead to HAZ liquation cracking. Segregation of impurity elements, particularly sulfur and phosphorus, to the grain boundaries can also promote liquation.

2.4.4 Preheat, Interpass Temperature and Post Weld Heat Treatment

In general, preheat and interpass temperature control is not required for austenitic stainless steels as it is for transformable (martensitic) steels. High preheat and interpass temperatures will slow the cooling rate, but this will have little effect on the ferrite-to-austenite transformation, since it occurs in very high temperatures, where preheat and interpass temperature control has very little effect on cooling rate. In cases where carbide precipitation leading to sensitization is a concern, interpass temperature may need to be controlled below some maximum since slow cooling through the carbide precipitation range may be damaging.

Post weld heat treatment is often required in thick-section weldments to relieve residual stresses. Because the coefficient of thermal expansion is much larger for austenitic stainless steels than e.g. the ferritic stainless steels, the magnitude of the residual stresses can be extremely large. Postweld stress relief may be necessary to reduce distortion in the component, particularly if postweld machining operations are required or if the weldment must maintain dimensional stability in service. Reduction of residual stresses is also crucial, if there is the potential for stress corrosion cracking in service.

The postweld heat treatment that is selected should be depended on the intention of thermal treatment, such as stress relief or microstructure modification. Stress-relief heat treatments are generally conducted in the temperature range 550 to 650 °C, which is below the nose of the curve for carbide precipitation, shown in Figure 2.18, and also below the temperature range in which embrittling compounds form (Table 2.3). It can be noted from Figure 2.18 that sensitization is possible if stress-relief treatment requires several hours, as may be the case in heavy section weldments. In this situation, the use of low-carbon base and filler metals or stabilized grades is recommended.
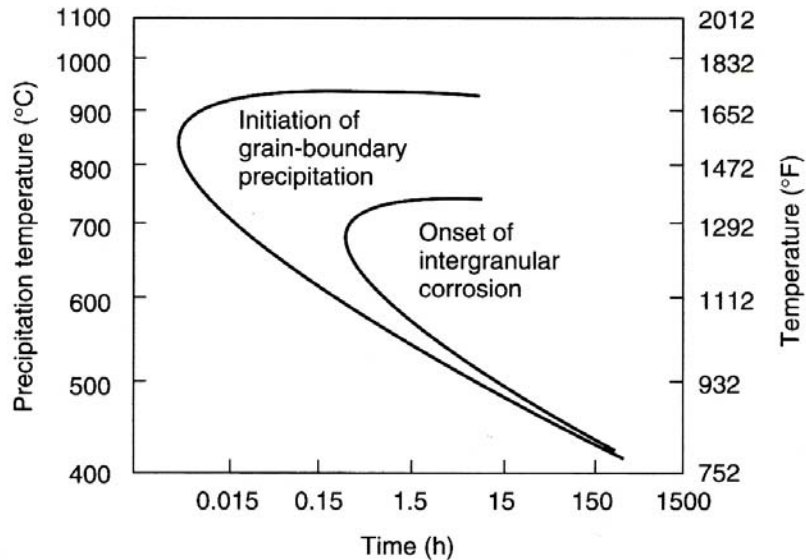
Figure 2.18 Precipitation of $M_{23}C_6$ carbides

Higher postweld heat treatment may be desirable in some cases, in order to relieve more effectively residual stresses, or to modify the as-welded microstructure. Special care should be taken in the range of 650 to 900 °C, since both $M_{23}C_6$ carbides and sigma (σ) phase form rapidly. The carbides formation may sensitize the material, while sigma phase can lead to embrittlement and loss of toughness. Postweld heat treatment can be possible in this range, if the weld metal is fully austenitic and if the base and filler metals are low-carbon grades. Weld metals that contain ferrite form sigma phase rapidly.

When the weldment undergoes postweld heat treatment in the range of 950 to 1100 °C, it will be completely relieved from residual stresses and also its as-welded microstructure will be modified, without the formation of carbides or sigma phase. Heating above 950 °C followed by rapid quenching will remove any carbides in the original microstructure, while heating to temperatures approaching 1100 °C will dissolve some or all of the ferrite, depending on the hold time at temperature, composition of the weld metals and the as-welded ferrite content. If this extreme heat treatment is used, rapid cooling to room temperature by water quenching is generally required since carbide precipitation may occur during slow cooling.

2.5 Weldability of Austenitic Stainless Steels

Although the austenitic grades are generally considered to be very weldable, they are subject to a number of weldability problems, if proper precautions are not taken. Weld solidification and liquation cracking may occur depending on the composition of the base and filler metal and the level of impurities, particularly S and P [18]. Solid-

state cracking, icluding ductility dip, reheat for stress relief and Cu contamination, has also been encountered in these alloys [20].

Despite the good general corrosion resistance of austenitic stainless steels, they may be subject to localized forms of corrosion at grain boundaries in the HAZ (IGA and IGSCC) or at stress concentrations in and around the weld. Because many of the weld metals contain ferrite, intermediate temperature embrittlement due to sigma phase and carbide formation may also occur. As with the ferritic grades, the sigma phase precipitation reaction is quite sluggish and embrittlement by sigma phase is usually a service-related rather than a fabrication-related problem. However, it may occure during the postweld heat treatment of large structures or thick sections when cooling rates from the postweld heat treatment are extremely slow.

2.5.1 Weld Solidification Cracking

Weld solidification cracking can be a formidable problem with the austenitic stainless steels. Cracking susceptibility is primarily a function of composition. Weld metals that solidify in the A mode and are fully austenitic tend to be the most susceptible, while those that solidify in the FA mode tend to be the most resistant to solidification cracking. High impurity levels, particularly sulfur and phosphorus, tend to increase the susceptibility in alloys that solidify in the A and AF mode [20, 21, 23]. However, the addition of other elements, such as niobium, has shown a tendency to increase the resistance to solidification cracking [19].

Examples of weld solidification cracking in alloys that solidify as primary austenite are presented in Figure 2.19. Weld restrain conditions and weld shape also influence cracking susceptibility. High levels of heat input resulting in large weld beads or excessive travel speeds that promote teardrop-shaped weld pools are most problematic with respect to cracking. Concave bead shape and underfilled craters a weld stops also promote solidification cracking.

Weld solidification cracking is a strong function of composition, as shown by the schematic representation of cracking susceptibility versus Cr_{eq}/Ni_{eq} (WRC-1992 equivalents) in Figure 2.20. It can be seen, from the schematic figure, that the A and AF modes are the most susceptible to cracking that the FA and F modes, which show good resistance in solidification cracking. In fact, the F mode is more susceptible to cracking than FA, but superior to A and AF. Thus, composition can be used very effectively to control weld solidification cracking. The principal reason for the superiority of the FA mode in solidification cracking resistance is the existence of a two-phase austenite + ferrite mixture along SGBs at the end of solidification that resists wetting by liquid films and presents a tortuous boundary along which cracks must propagate [1,18,19,20].

Historically, a number of factors have been used to explain the beneficial effect of ferrite on solidification cracking resistance in austenitic stainless steels. However, some of those factors may have

no significant or even negligible influence on the resistance to solidification cracking.
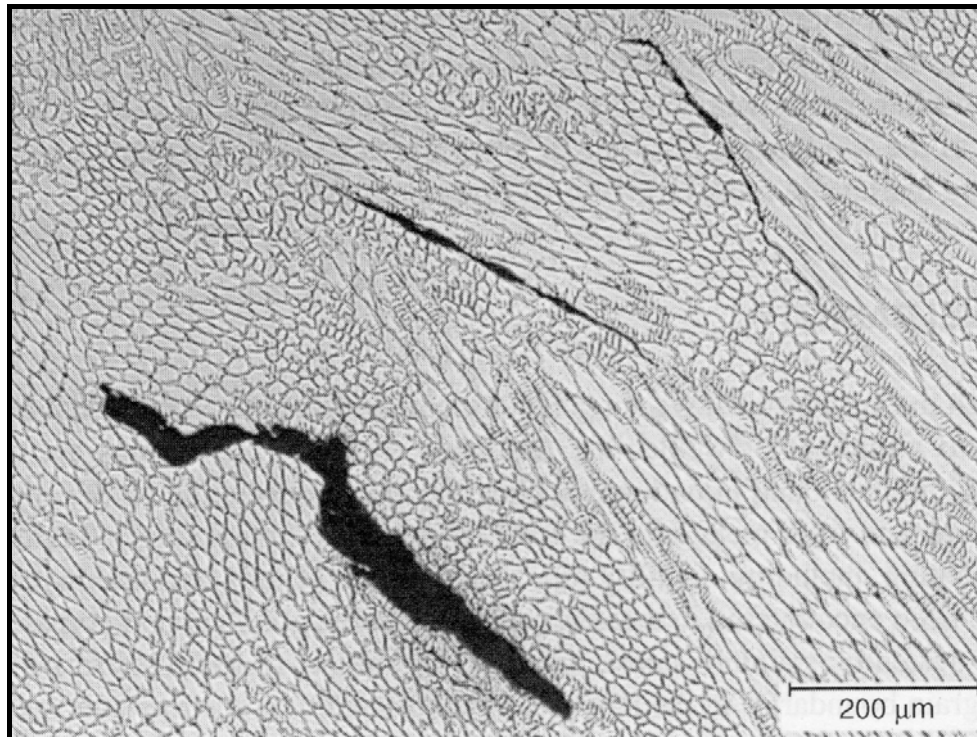
(a)

(b)

Figure 2.19 Weld solidification cracks in a) fully austenitic weld metal (FN 0) b) weld metal with FN 6 – FA solidification mode [1]
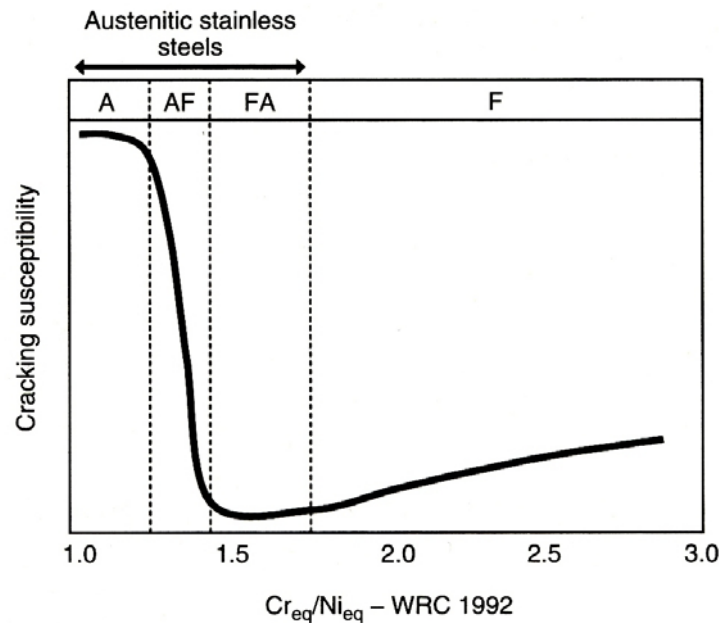
Figure 2.20 Weld solidification cracking susceptibility as a function of composition

Ferrite certainly has higher solubility for impurity elements such as sulfur and phosphorous, which restricts their partition to interdendritic regions during primary ferrite solidification. The most important factors, however, are the nature of boundary wetting and the inherent boundary tortuosity that occurs when ferrite and austenite are both present at the end of solidification. In the FA mode, a ferrite-austenite boundary is present at the end of solidification that is both difficult for liquid films to wet and presents a very non-planar crack path. Thus, once a crack is initiated, it becomes very difficult for it to propagate along this boundary. On the other hand, both austenite-austenite (A mode) and ferrite-ferrite (F mode) boundaries are much straighter, since no secondary solidification product is present. This makes crack propagation much easier. In the AF mode, some ferrite is present along a relatively smooth A-A boundary resulting in some improvement over fully austenitic solidification. The effect of boundary tortuosity is presented in Figure 2.21. Weld solidification cracks occur preferentially along solidification grain boundaries. Under Type A solidification, these boundaries are very straight, contain no residual ferrite and offer very little resistance to crack propagation if a liquid film wets the boundary. By contrast, a SGB under Type FA solidification contains a mixture of ferrite and austenite that mitigates liquid film wetting and complicates crack propagation, since the crack must follow a very non-planar austenite-ferrite interface.
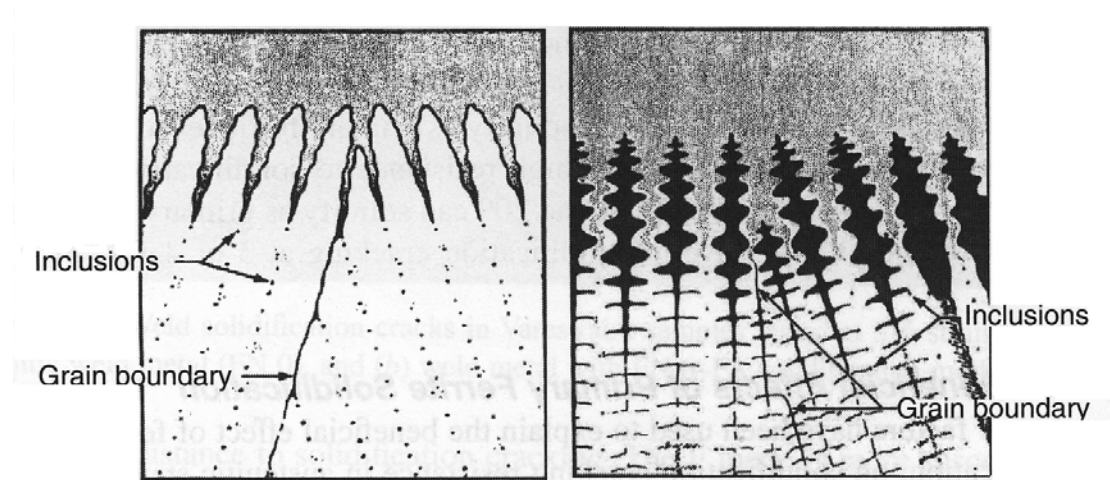
Figure 2.21 Effect of solidification type on grain boundary tortuosity a)A solidification b)FA solidification with skeletal ferrite [22]

2.5.2 Preventing Weld Solidification Cracking

Avoiding or minimizing weld solidification cracking in austenitic stainless steels is accomplished simply and most effectively by controlling the composition of base and filler metals. By assuring solidification as primary ferrite, the potential for cracking will be effectively eliminated. For most stainless steels this means that the composition should be controlled to achieve the FA solidification mode, resulting in the presence of FN 3-20 in the weld deposit. The use of constitution diagrams, such as WRC-1992, can be very helpful in accomplishing the desired composition.

In systems where the base and filler compositions preclude FA solidification, hence solidify as primary austenite, the potential for cracking will be much higher. The most effective way to avoid cracking in these welds is to reduce impurity content and/or minimize the weld restrain. High-purity fully austenitic weld metals can be quite resistant to weld cracking under conditions of moderate restrain. Convex bead shape and filled weld stops (craters) are also helpful.

Depending on the application and/or service conditions, some care should be taken when prescribing a weld metal ferrite content. While the presence of ferrite levels in the range of FN 3 to 20 is almost certain to avoid solidification cracking, ferrite above FN 10 may in fact compromise mechanical properties if the weldment is to be stress-relieved of the structure put to service at either cryogenic temperatures or elevated temperatures.

Service temperatures in the range of 425 to 870 °C can lead to embrittlement due to formation of alpha-prime (α') or sigma (σ) phase, both of which form preferentially at the ferrite-austenite interface. For weld metals, with FN above 10, these phases can severely reduce toughness and ductility. High ferrite contents have also been shown to reduce elevated temperature stress-rupture properties. Hence, in the

quest for appropriate base and filler metal, composition and moderate ferrite content is the aim to prevent solidification cracking.

2.5.3 HAZ Liquation Cracking

Austenitic stainless steels can be susceptible to various forms of cracking in the HAZ [24, 25]. HAZ liquation cracking occurs intergranularly due to localized melting of the base metal grain boundaries adjacent to the fusion line where temperatures are close to the weld metal solidus. The liquation is associated with the formation of low melting eutectic phases caused by segregation of elements such as niobium and titanium along with impurities such as phosphorous and silicon [23].

HAZ liquation cracking can be controlled by managing the composition of the base metal. Base metals that have a Ferrite Potential (on the WRC-1992 diagram) of 1 or higher will for some ferrite along the HAZ/PMZ (Partly Melted Zone) boundary, as shown in Figure 2.17 and effectively inhibit liquation cracking. In alloys where the HAZ is fully austenitic, and there is no grain boundary ferrite, liquation cracking can be minimized by restricting impurity levels and grain size. Lowering the heat input will result in steeper temperature gradients in the surrounding HAZ and restrict the distance over which liquation occurs. Grain size also has an important role effect on liquation cracking susceptibility, with smaller grain improving the cracking resistance. Since failure occurs along grain boundaries, increasing the grain boundary area, a reduction of segregation and local stress occurs, which would result in higher total stress to initiate cracking. Examples of HAZ liquation cracking are presented in Figure 2.22.

(a)   (b)
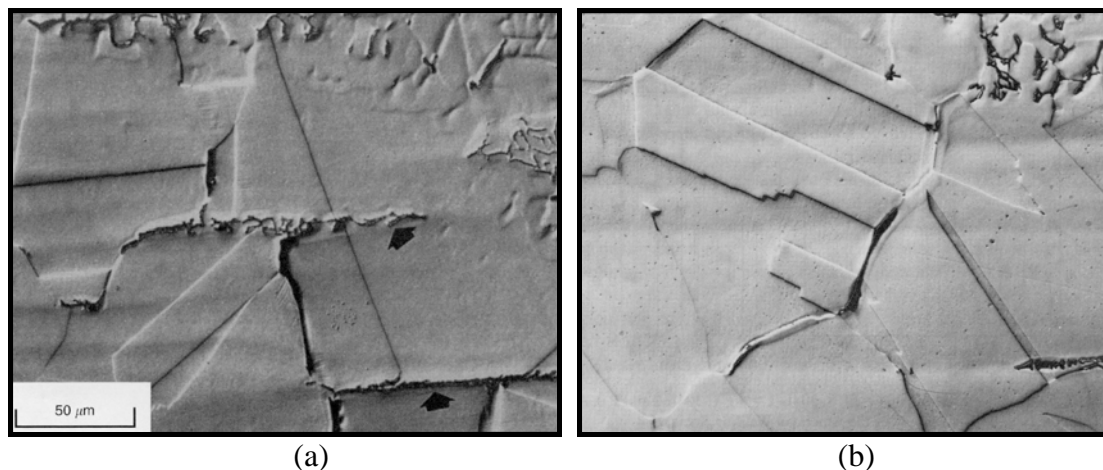
Figure 2.22 HAZ liquation cracking in the HAZ of a) Type 304 with FP 1 and b) Type 304L with FP 0 [26]

2.5.4 Weld Metal Liquation Cracking

Weld metal liquation cracking occurs in multipass welds along SGBs or MGBs. Fully austenitic welds are the most susceptible, due to the presence of a primary austenite solidification structures, A or AF Type, that exhibit significant segregation. Weld metals that contain sufficient ferrite sufficient ferrite, greater than FN 2 to 6, are generally resistant to weld metal liquation cracking. These defects are also referred as microfissures since they tend to be small and buried within the weld deposit.

An example of WM liquation cracking is displayed in Figure 2.23, where the weld metal is fully austenitic. This crack lies in the HAZ of the pass above and resides along a MGB. It is relatively short in the cross-section dimension of the weld since it exists only where remelting of the MGB occurs during reheating, due to the subsequent pass. The detection of these cracks is difficult because they are relatively short. Metallographic examination of a fissure bend test is necessary to find them.
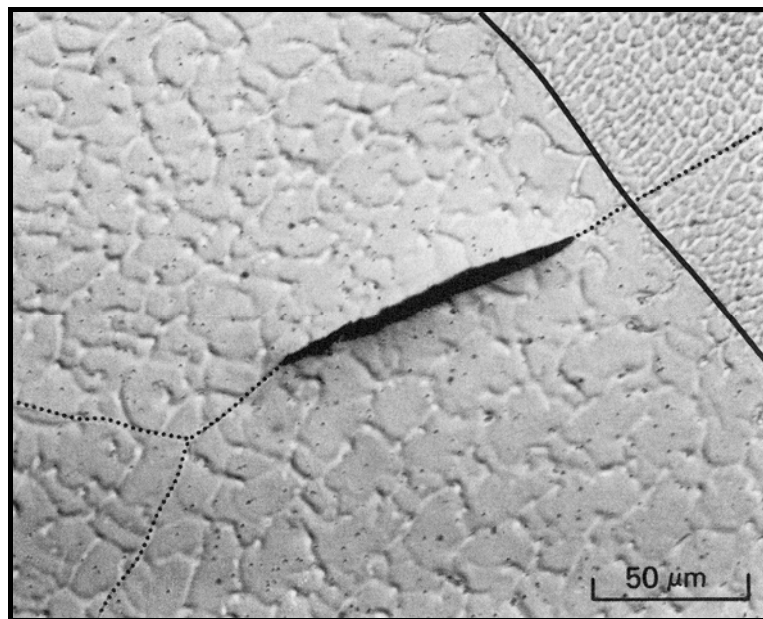
Figure 2.23 Weld metal liquation cracking along a MGB in a fully austenitic multipass weld. The solid line represents the fusion boundary of the subsequent pass, while dotted lines show the location of the MGBs

Weld metal liquation cracking is best controlled by adjusting the deposit composition such that ferrite is present in the deposit. In fully austenitic deposits, control of impurity levels and minimizing heat input can reduce or eliminate this form of cracking. Some filler metals have been developed with increased Mn to minimize cracking in fully austenitic welds [27]. The control of weld metal ferrite content is also extremely important, as Lundin et al. showed, for avoiding cracking in multipass welding [28, 29, 30]. They used the Fissure Bend test on multipass weld pads to determine the critical level of ferrite necessary to eliminate cracking. Their results are presented in Table 2.6.

Table 2.6 Minimum F needed to avoid WM liquation cracking [30]

Weld Metal	Minimum FN
316	1.5
308	2.0
316L	2.5
308L	3.0
309	4.0
347	6.0

2.6 Corrosion Resistance

Although austenitic stainless steels are often selected because of their corrosion resistance, some precautions must be taken when these alloys are welded and exposed to certain environments. The general atmospheric corrosion resistance of austenitic grades is very good. At room temperature, atmospheric corrosion is essentially negligible and the material will remain stainless indefinitely. At elevated temperature, general corrosion rates increase and some degradation and material loss will occur with time. In freshwater marine environments, general corrosion rates are also quite low, on the order of 2.5×10^{-5} mm/yr or less. In addition to general corrosion, austenitic stainless steels may experience the following forms of corrosion: pitting, intergranular, stress-assisted, crevice, galvanic, erosion corrosion and microbiologically induced corrosion [2, 6].

Welding can produce metallurgical modifications that can increase susceptibility to corrosion attack. In combination with the residual stresses that are present following welding, these modifications can result in accelerated attack of the weld region. Two forms of welding-related corrosion have been studies extensively in austenitic stainless steels because of the possibility of compromising the engineering usefulness of the welded structure. These forms are *intergranular corrosion* (IGC), often called *intergranular attack* (IGA), in the HAZ and *stress corrosion cracking* (SCC). Stress corrosion cracking can occur both inter- and intragranularly (or transgranularly), depending on the microstructure and stress state. When it occurs intergranularly, it is termed *intregranular stress corrosion cracking* (IGSCC).

2.6.1 Intergranular Corrosion

Intergranular corrosion has always been a subject of investigation and research [31-35], due to the implications that can cause to the welded structures in service conditions. Figure 2.24 presents a schematic representation of a weld that has undergone intergranular attack in the HAZ. On the surface, exposed to the corrosive environment, often appears a linear area of attack that

parallels the fusion boundary. In cross section, severe attack (or weld "decay") can be observed along a sensitized band in the HAZ. Note that this band is at some distance from the fusion boundary. This is due to the fact that the carbide precipitation that leads to sensitization occurs in the temperature range of from about 650 to 850 °C. Above this temperature range, carbides go back into solution and thus the region adjacent to the fusion boundary is relatively free of carbides, assuming that the cooling rates are rapid enough to suppress carbide precipitation during cooling.
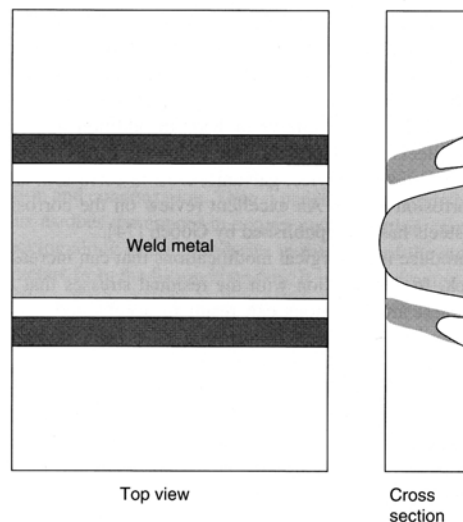
Figure 2.24 Schematic representation of Intergranular attack in the HAZ

In the HAZ of most austenitic stainless steels, Cr-rich $M_{23}C_6$ carbides form preferentially along grain boundaries, shown schematically in Figure 2.25. This results in a chromium-depleted zone along the grain boundary that is "sensitive" to corrosive attack. Hence, the term sensitization is often used to describe the metallurgical condition leading to intergranular attack. The exception to this is the stabilized grades of stainless steel, such as Types 347 and 321, containing Nb and/or Ti. In these steels the Nb and Ti ties up carbon in the form of stable MC-type carbides and minimizes the formation of $M_{23}C_6$ carbides and the depletion of chromium in the grain boundaries.
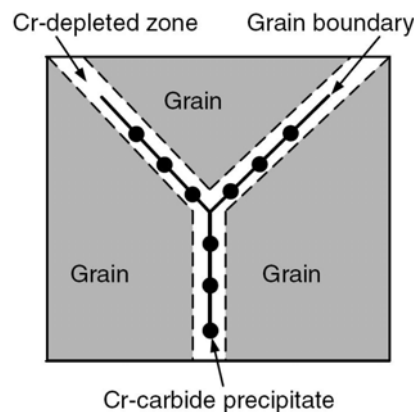
Figure 2.25 Grain boundary carbide precipitation and local chromium depletion [6]

Intergranular corrosion results from the localized precipitation of Cr-rich carbides, or carbonitrides, at the grain boundary. This precipitation requires short-range diffusion of Cr from the adjacent matrix and produces a Cr-depleted region surrounding the precipitate, as shown in Figure 2.26. This reduces local corrosion resistance of the microstructure and promotes rapid attack of the grain boundary region. In certain corrosive environments the effect is a local "ditching" at the grain boundary, as shown in Figure 2.26(a). In extreme cases, the grains will actually drop out of the structure because of complete grain boundary attack and dilution.

(a)   (b)

(c)
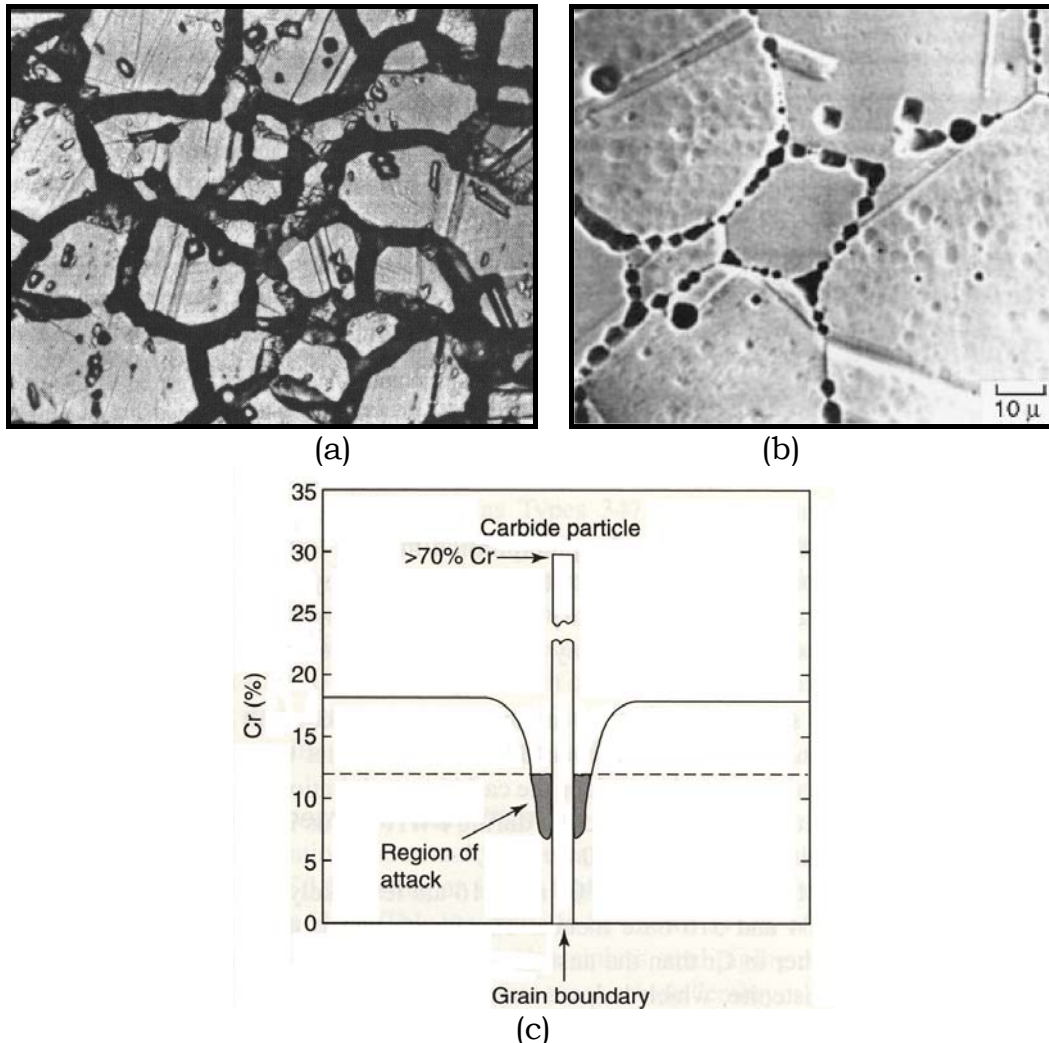
Figure 2.26 Intergranular corrosion: Grain boundary attack in the A of Type 304 a) with C 0.06 wt% [1], b) with C 0.05 wt% [6] and c) chromium depletion adjacent to the grain boundary carbide [1]

Carbon content has the most profound influence on susceptibility to IGC in austenitic stainless steels. The use of low-carbon (L grades) alloys minimizes the risk of sensitization by slowing down the carbide precipitation reaction. The time-temperature-precipitation curves, in Figure 2.27, demonstrate the effect of carbon content on the time to precipitation. For low carbon content (e.g. C<0.04 wt %), the nose of the curve is beyond 1 hour, while for carbon levels from 0.06 to 0.08

wt % the time of precipitation may be less than a minute. This difference demonstrates the benefit of the low-carbon alloys for reducing or eliminating HAZ grain boundary sensitization during welding. The presence of residual stresses in the HAZ may also serve to accelerate the precipitation reaction.
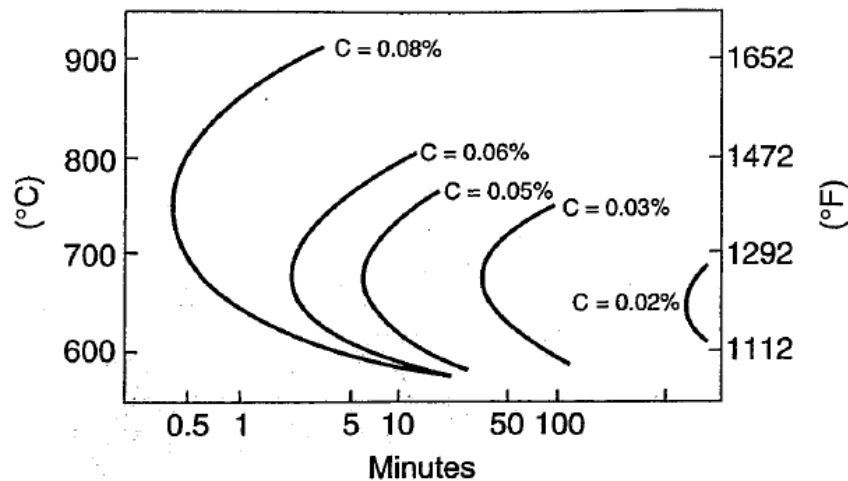
Figure 2.27 $M_{23}C_6$ time-temperature-precipitation curves for "18-8" alloys with variable carbon content [2]

In most cases sensitization occurs in the HAZ as a direct result of the weld thermal cycle. It should be noted, however, that the stress relief temperature range for most austenitic stainless steels overlaps the carbide precipitation range. Care must be taken not to sensitize the entire structure during PHT. This is a particular concern with alloys containing more than 0.04 wt % C.

In general, weld metals, such as 308 and 316, are less likely to be sensitized than corresponding 304 and 316 base metals. The ferrite that is normally found in the weld metal is richer in Cr than austenite, and Cr diffuses much more rapidly in ferrite than in austenite, which helps overcome any Cr depletion. Cr-rich carbides tend to precipitate at the tortuous ferrite-austenite boundaries instead of at usual much straighter austenite-austenite boundaries. All these factors greatly limit the tendency for sensitization in austenitic stainless steel weld metals containing ferrite [36]. So, except in fully austenitic stainless steel weld metals, sensitization is largely a HAZ problem.

In order to avoid the consequences and damage that can be caused by sensitization, it is possible to minimize or eliminate intergranular corrosion in austenitic stainless steel welds by the following methods:
- Selection of base and filler metal with as low carbon content as possible (grades such as 304L and 316L)
- Usage of base metals that are "stabilized" by additions of niobium (Nb) and titanium (Ti). These elements, as noted above, are more potent carbide formers than chromium and thus tie up

the carbon, minimizing the formation of Cr-rich grain boundary carbides.

- Usage of annealed base material or annealing prior to welding, in order to remove any prior cold work, which accelerates carbide precipitation.
- Usage of weld heat inputs and low interpass temperatures to increase weld cooling rates, thereby minimizing the time in the sensitization temperature range.
- During pipe welding, cooling the inside of the pipe with water after the root pass. This will eliminate the sensitization of the inner diameter.
- Solution heat treating after welding. Heating the structure into the temperature range 900 to 1100 °C dissolves any carbides that may have formed along grain boundaries in the HAZ. The structure is then quenched from this temperature to prevent carbide precipitation during cooling. However, there are a number of practical considerations that tend to limit the usefulness of this method. Distortion during quenching is a serious problem for plate structures.

2.6.2 Stress Corrosion Cracking

Many of the stainless steels are inherently susceptible to SCC, particularly in Cl-bearing environments, such as seawater. Copson in his work [37] presented the known Copson-curve, where he plotted the resistance to SCC in boiling magnesium-chloride as a function of nickel content. The use of this aggressive environment intended to accelerate the corrosion process that would occur in other Cl-bearing environments, such as seawater. The curve shows that in the content range 8 to 12 wt % of Ni, the resistance to SCC is extremely low, but outside this range the resistance is high and SCC is difficult to occur. But the latter range is precisely the nickel range of many popular austenitic alloys, such as 304 and 316.

SCC can be avoided by selecting alloys with either higher (>20 wt %) or lower (<5 wt %) nickel content. In the case of high nickel content the use or superaustenitics or Ni-base alloys is common, while in the case of low-nickel alloys, ferritic or duplex alloys are often selected. SC has also been observed in caustic (high-pH) environments, such as in pulp and paper mills. It appears that the same rules apply in these environments as with Cl-bearing environments with respect to alloy selection to avoid caustic-induced SCC.

In Figure 2.28, an example of severe transgranular SCC in a Type 316L tubesheet after exposure to a caustic solution of sodium hydroxide in a pulp and paper mill. This structure was exposed to the caustic solution for less than a year prior to failure. The residual stresses resulting from the weld in addition to impose operating stresses led to the severe cracking, presented in the Figure.
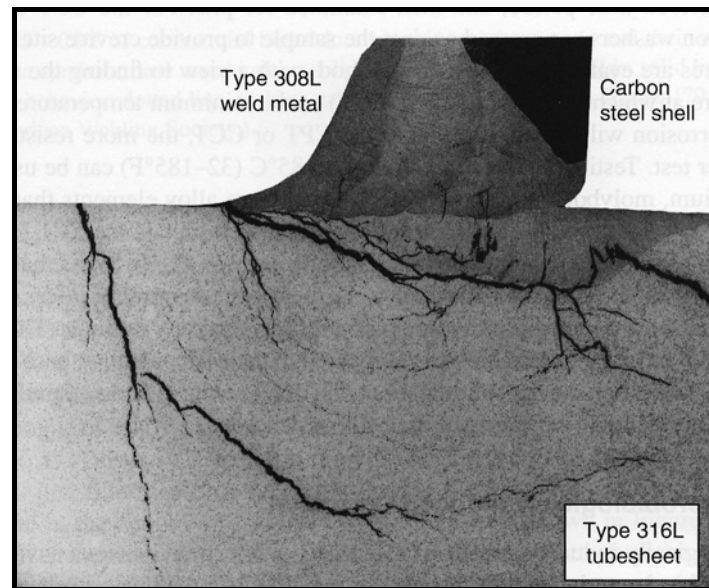
Figure 2.28 Transgranular SCC near the weld in Type 316L after exposure to a caustic sodium hydroxide solution [1]

Stress corrosion cracking is best avoided by proper alloy selection. The use of duplex and ferritic stainless steels in applications where austenitic grades would otherwise be selected can avoid SCC. Welding may exacerbate SCC in alloy systems that are otherwise resistant due to changes in microstructure and residual stresses. Sensitization can promote IGSCC in both austenitic and ferritic stainless steels. Weld designs or conditions that generate high residual stresses or create stress concentrations can also promote SCC. Postweld stress relief can sometimes be used to reduce these stresses and minimize susceptibility to SCC. But, as noted above, postweld stress relief needs to be done with care.

2.6.3 Pitting and Crevice Corrosion

Pitting and crevice corrosion are related phenomena. Halible eement ions, most commonly Cl^-, are very often present in aqueous solutions. A penetration of the passive film on the stainless steel surface allows the metal beneath to become active. The penetration site might be an inclusion exposed to the corrosive media [38]. In Figure 2.29(a), an example of pitting corrosion is presented. A crevice, as might exist at the edge of a gasket or sealing ring at a flanged connection, can also serve as a pit initiation site. Figure 2.29(b)presents an example of crevice corrosion.

Pitting and crevice corrosion resistance can be measured by the ASTM G48 ferric chloride test. Through this test, a critical pitting temperature CPT) and a critical crevice temperature (CCT) are determined by two separate methods, prescribed in the standard. The CPT and CCT can be used as blueprints, depending on the service conditions of the welded section, to avoid the undesirable corrosion.

Chromium, molybdenum, tungsten and nitrogen are alloy elements that improve pitting and crevice corrosion resistance [38-44].
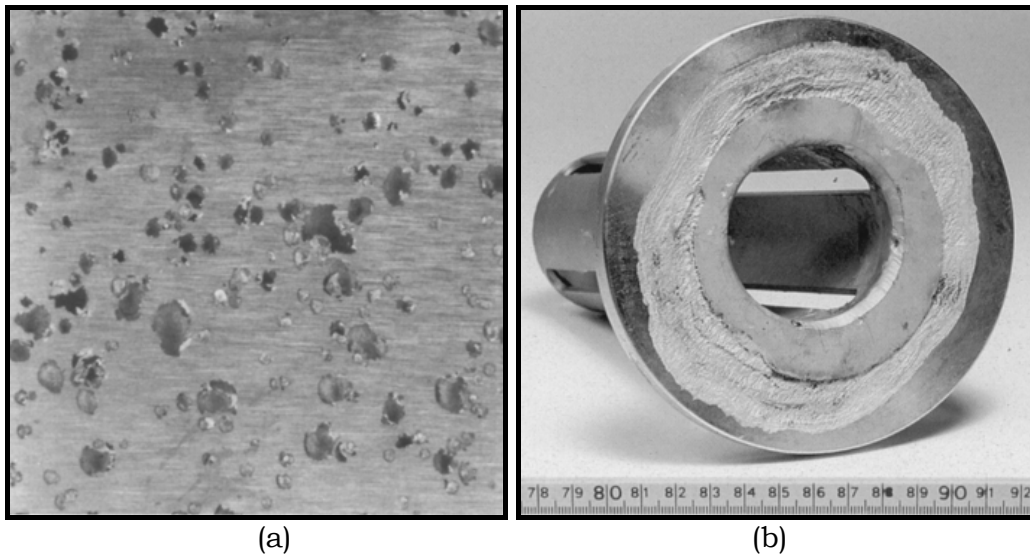
(a)   (b)

Figure 2.29 An example of (a) pitting corrosion on the surface of an austenitic stainless steel [43] and (b) crevice corrosion on the flange of an austenitic stainless steel

Chapter Bibliography

1. John C. Lippold and Damian J. Kotecki, 2005, *Welding Metallurgy and Weldability of Stainless Steels*, John Wiley & Sons Inc.
2. D. Peckner and I. M. Bernstein, 1977, *Handbook of Stainless Steels*, McGraw-Hill, New York
3. H. R. Copson, 1959, *Physical Metallurgy of Stress-Corrosion Fracture*, Interscience, New York
4. AISI – American Iron and Steel Institute, www.steel.org
5. A. J. Sedriks, 1996, *Corrosion of Stainless Steels*, John Wiley & Sons Inc.
6. Sindo Kou, 2003, *Welding Metallurgy* 2nd Edition, John Wiley & Sons Inc.
7. S. Azuma, T. Kudo, H. Miyuki, M. Yamashita, H. Uchida, 2004, *Effect of nickel alloying on crevice corrosion resistance of stainless steels*, Corrosion Science Vol. 46 pp. 2265 – 2280
8. J. Nakano, Y. Miwa, T. Kohya, T. Tsukada, 2004, *Effects of silicon, carbon and molybdenum additions on IASCC of neutron irradiated austenitic stainless steels*, Journal of Nuclear Materials, 329 – 333 pp. 643 – 647
9. J. W. Sa e.a., 2005, *Mechanical characteristics of Austenitic Stainless Steel 316LN Weldments at Cryogenic Temperatures*, Fusion Engineering – 21st IEEE/NPS Symposium, September 2005
10. H. B. Cary, S. C. Hezler, 2005, *Modern Welding Technology* 6th Edition, Pearson Prentice Hall™
11. *Welding Handbook 8th Edition – Volume 4, Materials and Applications Part 2*, 1998 - The American Welding Society
12. J. C. Lippold, W. F. Savage, 1979, *Solidification of austenitic stainless steel weldments, 1: a proposed mechanism*, Welding Journal 58(12), pp. 362-374
13. B. Sundman, B. Jansson, J. O. Andersson, 1985, *The Thermo-Calc ™ Data Bank System*, Calphad Vol.6 pp. 153-190
14. T. Koseki, M. C. Flemings, 1996, *Solidification of undercooled Fe-Cr-Ni alloys: Part II - microstructural evolution*, Journal of Metallurgical and Materials Transactions Vol. 27A (10) pp. 3226-3240
15. P. L. Ferrandini, C. T. Rios, A. T. Dutra, M. A. Jaime, P. R. Mei, R. Caram, 2006, *Solute segregation and microstructure of directionally solidified austenitic stainless steel*, Materials Science and Engineering A 435-436 pp. 139-144
16. J. C. Ma, Y. S. Yang, W. H. Tong, Y. Fang, Y. Yu, Z. Q. Hu, 2007, *Microstructural evolution in AISI 304 stainless steel during directional solidification and subsequent solid-state transformation*, Material Science and Engineering A 444 pp. 64-68
17. S. Katayama, T. Fujimoto, A. Matsunawa, 1985, *Correlation among solidification process, microstructure, microsegregation and solidification cracking susceptibility in stainless steel weld metals*, Transactions of Japanese Welding Reasearch Institute, 14(1):123
18. V. Shankar, T. P. S. Gill, S. L. Mannan, S. Sundaresan, 2003, *Solidification cracking in austenitic stainless steel welds*, Sadhana Vol. 28, Parts 3 & 4, June & August pp. 359-382
19. Z. Sun, 1992, *A study of solidification crack susceptibility using the solidification hot-tension test*, Materials Science and Engineering, A154, pp. 85-92

20. B. Raj, V. Shankar, A. K. Bhaduri, 2006, *Welding Technology for Engineers*, Alpha Science International Ltd. - Oxford, U.K.
21. V. Shankar, T. P. S. Gill, S. L. Mannan, S. Sundaresan, 2003, *Effect of nitrogen addition on microstructure and fusion zone cracking in type 316L stainless steel weld metals*, Materials Science and Engineering, A343, pp. 170-181
22. J. A. Brooks, A. W. Thompson, J. C. Williams, 1984, *A fundamental study of the beneficial effects of delta ferrite I reducing weld cracking*, Welding Journal 63(3), pp. 71s-83s
23. L. Li, R. W. Messler, Jr., 1999, *The effect of phosphorous and sulfur on susceptibility to weld hot cracking in austenitic stainless steels*, Welding Journal 78(12), pp. 387s-396s
24. R. D. Thomas, Jr., 1984, *HAZ cracking in thick sections of austenitic stainless steels – Part 1*, Welding Journal 62(12), pp. 24-32
25. R. D. Thomas, Jr., 1984, *HAZ cracking in thick sections of austenitic stainless steels – Part 2*, Welding Journal 62(12), pp. 355s-368s
26. J. C. Lippold, I. Varol, W. A. Baeslack, 1992, *An investigation of heat-affected zone liquation cracking in austenitic and duplex stainless steels*, Welding Journal 71(1), pp. 1s-14s
27. J, Honeycompe, T. G. Gooch, 1972, *Effect of manganese on cracking and corrosion resistance on fully austenitic stainless steel weld metals*, Metal Construction and British Welding Journal 4(12):456
28. C. D. Lundin, D. F. Spond, 1976, *The nature of morphology of fissures in austenitic stainless steel weld metal*, Welding Journal 55(11), pp. 356s-367s
29. C. D. Lundin, W. T. DeLong, D. F. Spond, 1975, *Ferrite-fissuring relationship in austenitic stainless steel weld metals*, Welding Journal 54(8), pp. 241s-246s
30. C. D. Lundin, C. P. D. Chou, 1985, *Fissuring in the "Hazard HAZ" region of austenitic stainless steel welds*, Welding Journal 64(4), pp. 113s-118s
31. Martin Matula, et al., 2001, *Intergranular corrosion of ASI 316L steel*, Materials Characterization 46, pp. 203-210
32. H. Sahlaoui, K. Makhlouf, H. Sidhom, J. Philibert, 2003, *Effects of ageing conditions on the precipitates evolution, chromium depletion and intergranular corrosion susceptibility of AISI 316L: experimental and modeling results*, Materials Science and Engineering A 372, pp. 98-108
33. Y. Cui, C. D. Lundin, 2005, *Evaluation on initial corrosion location in E316L austenitic stainless steel weld metals*, Materials Letters 59, pp. 1542-1546
34. G. H. Aydoğdu, M. K. Aydinol, 2006, *Determination of susceptibility to intergranular corrosion and electrochemical reactivation behavior of AISI 316L type stainless steel*, Corrosion Science 48, pp. 3565-3583
35. Y. Cui, C. D. Lundin, 2007, *Austenite-preferential corrosion attack in 316 austenitic stainless steel weld metals*, Materials and Design 28, pp. 324-328
36. T. G. Gooch, 1996, *Corrosion behavior of welded stainless steels*, Welding Journal 75(5), pp.135s-154s
37. H. R. Copson, 1959, *Effect of composition on stress corrosion cracking of some alloys containing Ni*, in Physical Metallurgy of Stress Corrosion Cracking, Interscience, New York
38. L. Guocheng, C. Haidong, X. Chunchun, H. Zonghu, 2008, *Effect of strain and chloride concentration on pitting susceptibility for Type 304 austenitic stainless steel*, Chinese Journal of Chemical Engineering 16(2), pp. 314-319

39. A. Pardo, M. C. Merino, M. Carboneras, A. E. Coy, R. Arrabal, 2007, *Pitting corrosion behavior of austenitic stainless steels with Cu and Sn additions*, Corrosion Science 49, pp. 510-525
40. A. Pardo, M. C. Merino, A. E. Coy, F. Viejo, R. Arrabal, E. Matykina, 2008, *Pitting corrosion behavior of austenitic stainless steels – combining effects of Mn and Mo additions*, Corrosion Science Vol.50, pp. 1796-1806
41. D. R. Johns, K. Shemwell, 1997, The crevice corrosion and stress corrosion cracking resistance of austenitic and duplex stainless steels fastener, Corrosion Science Vol.39(3), pp. 473-481
42. H. Baba, Y. Kataba, 2006, Effect of nitrogen on crevice corrosion in austenitic stainless steels, Corrosion Science Vol.48, pp. 2510-2524
43. G. S. Frankel, 2003, *Pitting Corrosion, in ASM Handbook Vol. 13A - Corrosion: Fundamentals, Testing and Protection*, pp.236-241
44. R. G. Kelly, 2003, *Crevice Corrosion, in ASM Handbook Vol. 13A - Corrosion: Fundamentals, Testing and Protection*, pp.242-247

3D Numerical Modeling of Austenitic Stainless Steel 316L Multi-pass Butt Welding and Comparison with Experimental Results

3rd Chapter

Thermo-Mechanical Analysis of Welding

3. Thermo-Mechanical Analysis of Welding

Welding as a fabrication technique presents a number of difficult problems to the design and manufacturing community. The welding process incorporates a variety of parameters, which must be taken into account, in order to produce sound welded structures. The introduction of the Finite Element Analysis in the design procedure of the welding process, aimed at predicting its thermal, material and mechanical effects, resulted in what is known today as Computational Welding Mechanics (CWM).

Over the last years, developments in calculating the thermal and elastoplastic stress-strain cycles have been slow because of the inherent complexity of the geometry, boundary conditions and the nonlinearity of material properties. However, the exponential growth in computer performance, combined with equally rapid developments in numerical models and geometric modeling, has enabled CWM to reach the stage where most of the problems regarding welding can be effectively solved. Although the ability to perform such analyses is important, the real justification for CWM is that it is becoming cheaper, faster and more accurate to perform computer simulation than to do laboratory experiments.

Furthermore, numerical models can be utilized in ways that provide insight, which could never be obtained by experiment. For example, the distortion caused by welding of austenitic stainless steel is approximately three times higher than that caused by welding carbon steel. By analyzing models in which each property is varied separately, the sensitivity of the distortion to each property can be computed, analyzed and can eventually lead to techniques for reducing distortion.

3.1 Thermal Analysis of Welding

In thermal analysis, the fundamental principal is the conservation of energy. Therefore, the heat transfer theory deals with energy and ignores stress, strain and displacement. Energy is needed in the form of heat transfer, in order to melt the separate metals and with or without filler metal addition, to produce a homogenous welded joint. The heat that is applied must be adequate to weld the metals. The amount of heat needed depends on many factors, such as the material type, the welding procedure, and the dimensions of the joint, which all affect the total energy equivalent.

With the introduction of the heat input in the weld, the formation of a transient temperature field commences, which will finally be the welded section's temperature history. Far from the welding pool the temperature gradients during welding are quite smooth, but near the weld pool they become steeper. In the weld pool the temperatures exceed by far the melting temperature of the metal. For each metal alloy the temperature field is unique. This is due to the different

thermal properties that each alloy has. In Figure 3.1 several surface temperature fields, for various materials, are depicted.
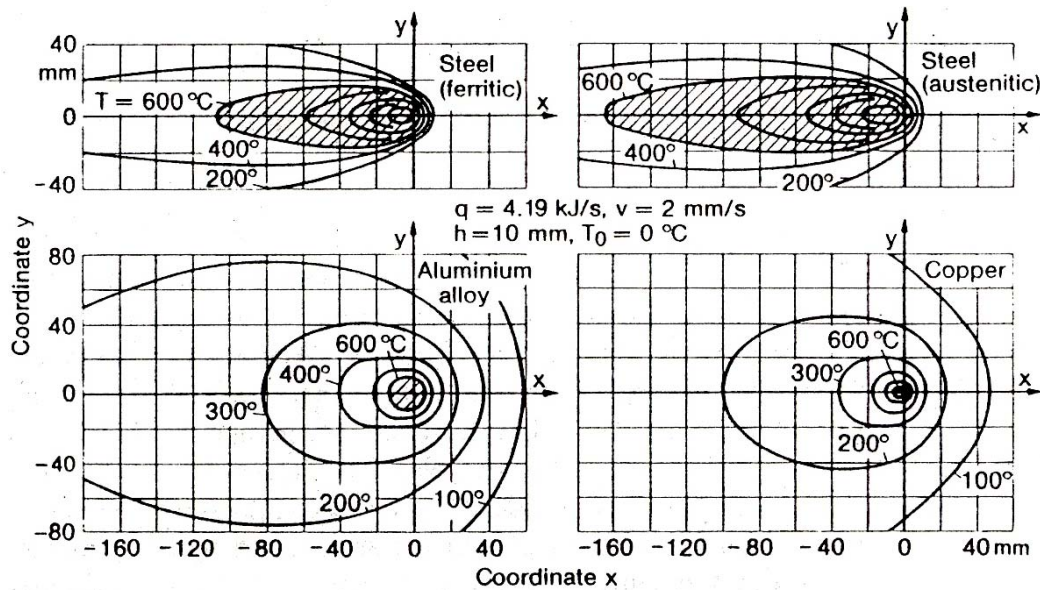

Figure 3.1 Temperature fields for various metals [2]

It is notable from the isothermal lines, in Figure 3.1, that, though the heat flux is the same in all cases, the temperature fields vary, due to the different material type. The gradients of the temperature distribution are extremely steep during welding of austenitic and ferritic stainless steel grades, but in the case of aluminum and copper the distribution seems to be quite smooth. As mentioned above, the reason for the above variation is the difference in all thermal temperature-dependent properties that the various materials exhibit. The properties that affect the temperature distribution and the overall thermal analysis in welding are the following:
  ✓ Thermal conductivity, λ [J/mm sec °C]
  ✓ Specific heat capacity, c [J/gr °C]
  ✓ Density, ρ [gr/mm³]
  ✓ Thermal diffusity [mm²/sec]
  Along with the above properties come also the convection and radiation heat transfer mechanisms that determine the interaction of the heated metal with the environment. In Figure 3.2, the specific heat and density are presented for mild, low and high-alloy steels, as a function of temperature. While density exhibits a decrease, for all alloys, during the whole temperature range, specific heat for the mild and low-alloy steels increases until the temperature range of the phase transformation of ferrite to austenite and then decreases rapidly. For the high alloy steels (such as stainless steels) the specific heat presents a moderate increase during the whole temperature range. Similarly, in Figure 3.3, the thermal conductivity and thermal diffusity are presented. Mild and low-alloy steels cover a wide range of thermal conductivity and diffusity values at ambient temperature, which tend to converge at a low range of values as the temperature

increases. The high-alloy steels cover a more restricted area in the diagrams, exhibiting small variations during temperature increase.

(a)   (b)
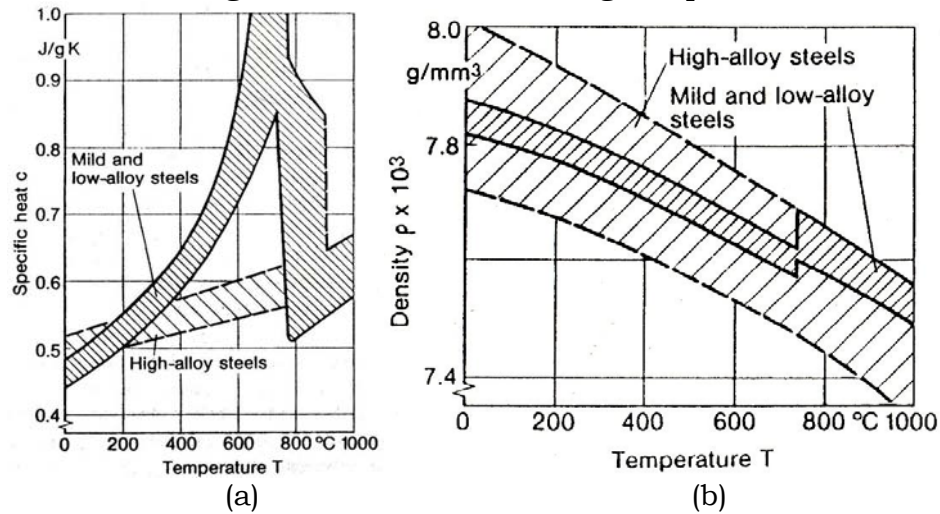
Figure 3.2 a) Specific heat, and b) density as a function of temperature [2]
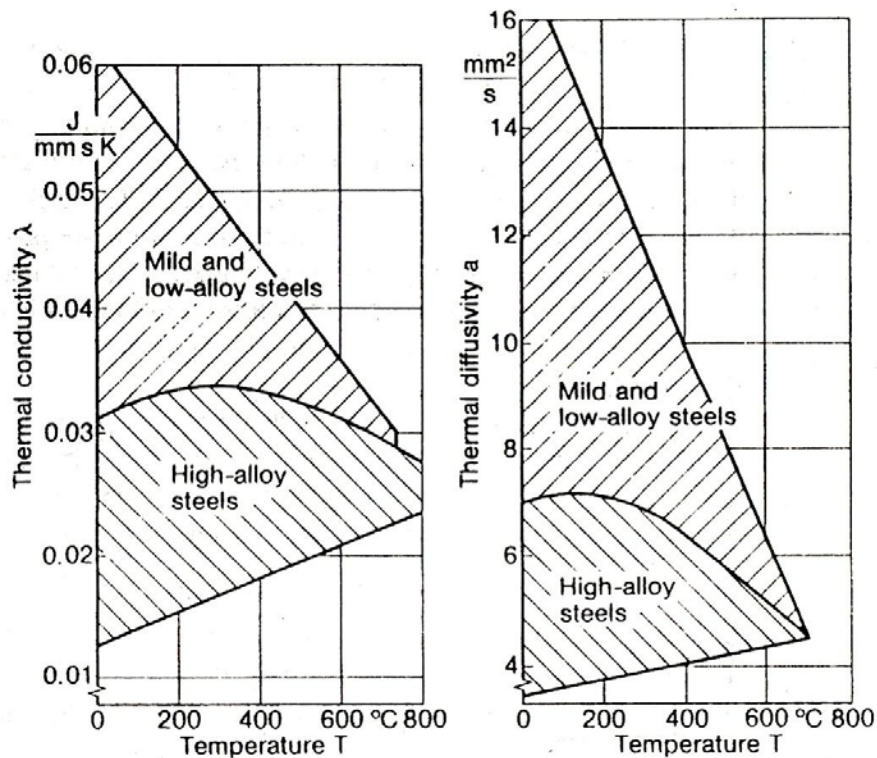
Figure 3.3 a) Thermal conductivity, and b) thermal diffusity as a function of temperature [2]

Each welding procedure, which depends on the geometry of the welded section, the material properties and many other factors, requires a different heat flux, resulting in a different temperature field, which is the unique temperature load history of each welded structure. The temperature load employed to the materials, along with the material properties, result into distortion and residual stresses of the welded structure.

The whole concept of CWM is to simulate the temperature load history of the welded structure and employ it to the precise geometry of the section to be welded, along with all the non-linear material properties, in order to end up with the same mechanical results that would be present in an actual welding procedure. The basic tools for the above analysis are a model of the heat source that will cause the local melting and joining of the materials, the non-linear temperature dependent properties of the material and the geometrical features of the section to be welded. However, each of the above features hides many parameters that if inputted to the simulation would result into a "heavy" analysis. A "heavy" analysis is an extremely time-consuming analysis, that may lead to failure and false results (e.g. due to ill-conditioning matrices). Thus, simplifications must be made in order not to burden the analysis, but at the same time to acquire good and reliable results that reflect to the reality of the welded procedure.

3.2 Welding Heat Source

The essential component, in order to simulate a welding procedure, would be the welding heat source, which is the cause of the whole process. The heat source, depending on the process, can be an arc or a high energy beam (Laser or Electron Beam Welding). In both cases, a large amount of energy is released and focused on the area to be welded, resulting to the melting of the materials and their joining upon cooling. One of the major characteristics of the heat source is its motion through time and space.

The first efforts of analyzing and simulating the moving heat sources were made by Rosenthal [4] and Rykalin [5]. In the latter years many researchers have proved the existence of errors, especially to Rosenthal's point or line heat source models, due to the fact that he assumed an infinite temperature in the heat source's center. These assumptions lead to false results in the FZ and in the HAZ temperature fields. To overcome the assumptions and limitations of Rosenthal's research, many researchers used the finite element method (FEM) to analyze heat flow in the weld.

One of the first suggestions, that the heat source should be distributed was made by Pavelic et al. [6]. They proposed a Gaussian distribution of the heat source on the surface of the workpiece, as shown in Figure 3.4(a). This distribution is known as the Pavelic's "disc", because of the circular form of the surface distribution. Many researchers followed this form of heat source distribution combining it with finite element analysis and achieving significantly better temperature distributions in the fusion and heat affected zones, than those computed with Rosenthal's model.
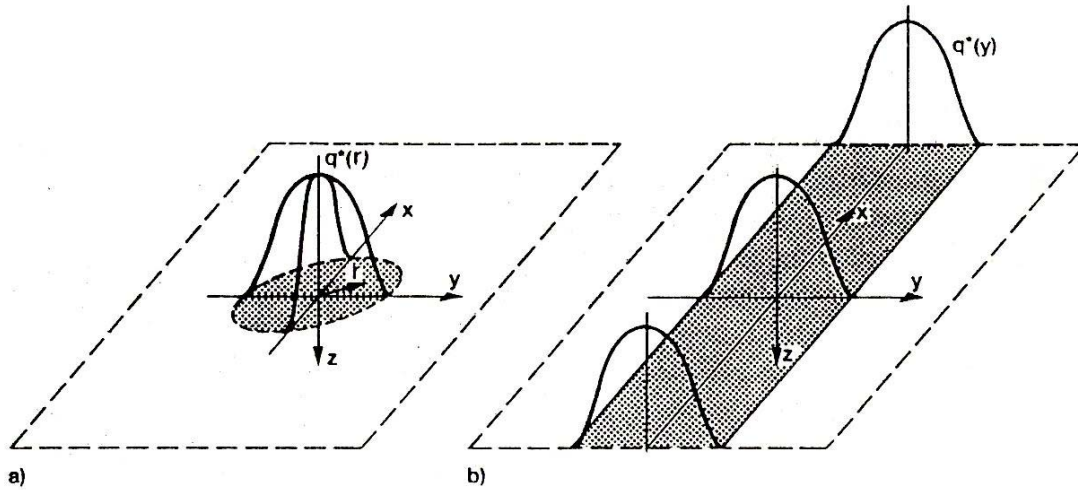
Figure 3.4 a) The Gaussian Heat source distribution b) travelling along weld seam

The basic equations that determine the surface heat flux of the Gaussian heat source are the following:

$$q_{surf} = q_{max}e^{-kr^2}$$

$$q_{max} = \frac{k}{\pi}q$$

[3.1]

In the above equations, q [J/s] is the effective output of the heat source and the factor k [1/mm^2] designates the heat source concentration, namely the width of the Gaussian distribution curve, as shown in Figure 3.5. The parameter r [mm] designates the distance from the centre of the circular source. As known, the Gaussian distribution runs towards zero only at infinity. It was important to establish an agreement, regarding which small values of the Gaussian distribution can be regarded as negligible. The minimum value, that sets the surface heat source distribution boundary is considered to be the 5% of the maximum value, thus $q_{min} = 0.05 \times q_{max}$.
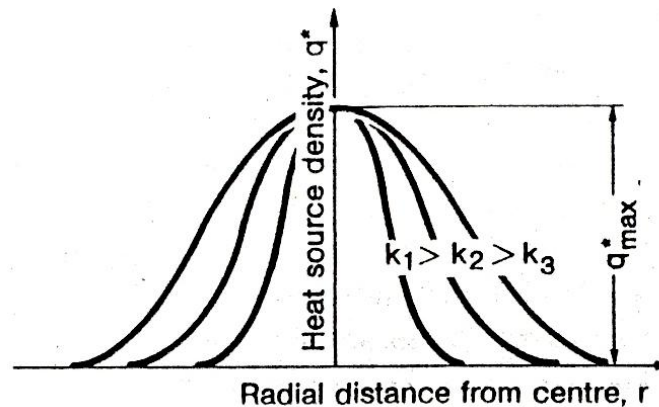
Figure 3.5 Several Gaussian heat sources for various k factor values

During the welding simulation the Gaussian heat source is travelling along the welding direction (Figure 3.4(b)) maintaining a stable welding speed, in order to input the same heat flux along the weld. The form of the weld metal, which derives from the Gaussian heat source movement, was initially described as a hemisphere (Figure 3.6). However, this shape was never in good agreement with the form that the metallographic pictures of the weld metal showed. The hemispherical form has been substituted with an ellipsoidal form, resulting into a better shaped weld metal profile.
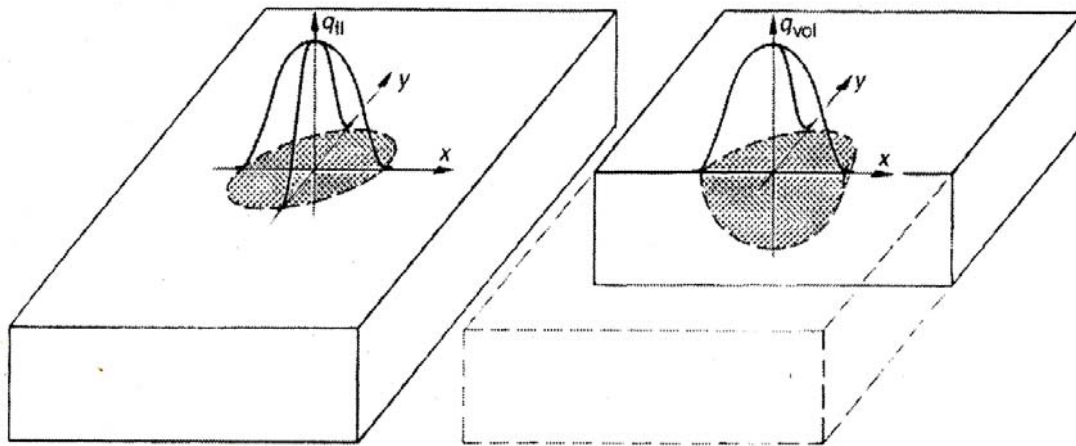
Figure 3.6 The sphere-shaped volume distribution

It has been observed from many researchers, who worked on analytical models of welding heat sources that, while the heat source moves, the thermal gradients are different in front and in the back of the source. This is due to the welding speed and the heat flux, especially in the arc welding processes, which are considered to be medium-power sources and the welding speeds are necessarily low. The Gaussian heat source model could not offer such a different thermal gradient. Finally, Goldak et al. [7] proposed an analytical heat source model, which is known as the "double ellipsoidal heat source model", shown in Figure 3.7.
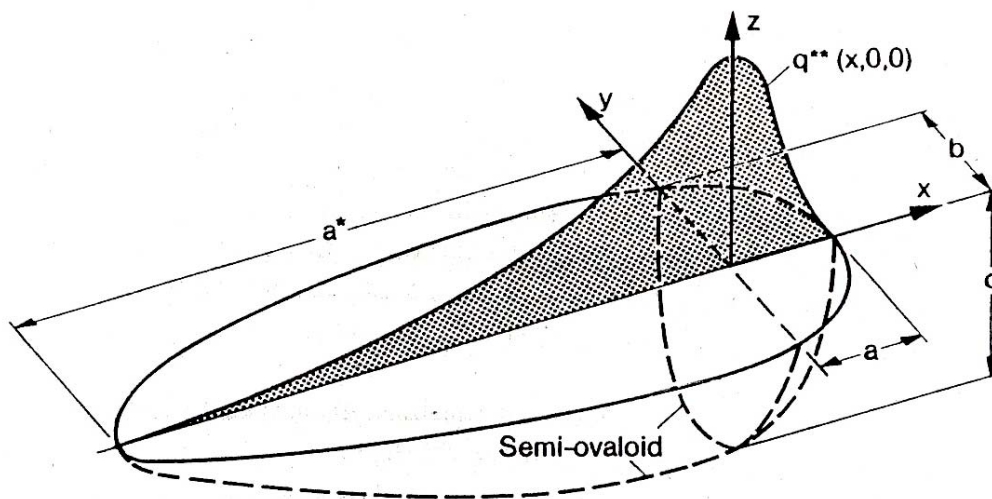
Figure 3.7 The double ellipsoidal heat source [2]

The double ellipsoidal heat source compromises two different volumetric power sources of the same geometrical shapes but of dissimilar dimensions. The two different components of the model define the front and the rear of the heat source, respectively. The mathematical equation that describes the front of the heat source models its steep shape, resulting from the movement of the heat source. Meanwhile the equation that describes the rear of the heat source is adapted to the smooth gradients of the heat flux. In conclusion, two different semi-ellipsoids are combined to give the heat source, while the heat flux within each ellipsoid is described by equations 3.2(a, b).

For a point (x, y, z) within the first semi-ellipsoid located in the front of the welding arc, the heat flux equation is described as:

$$Q(x,y,z) = \frac{6\sqrt{3}r_f Q}{a_h b_h c_{hf} \pi \sqrt{\pi}} \exp(-\frac{3x^2}{c_{hf}^2} - \frac{3y^2}{a_h^2} - \frac{3z^2}{b_h^2}) \qquad \text{[3.2(a)]},$$

while, for a point located in the second semi-ellipsoid, covering the rear section of the arc, the heat flux is described as:

$$Q(x,y,z) = \frac{6\sqrt{3}r_b Q}{a_h b_h c_{hb} \pi \sqrt{\pi}} \exp(-\frac{3x^2}{c_{hb}^2} - \frac{3y^2}{a_h^2} - \frac{3z^2}{b_h^2}) \qquad \text{[3.2(b)]}$$
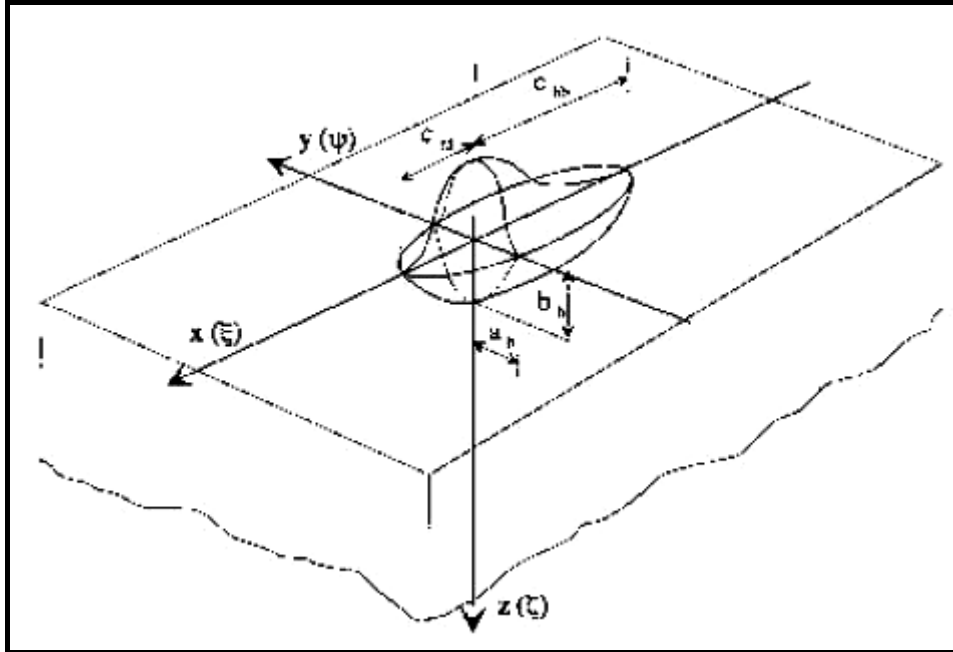
Figure 3.8 Geometric parameters of Goldak's double ellipsoidal model [8,9]

where a_h, b_h, c_{hf} and c_{hb} are the ellipsoidal heat source geometric parameters, shown in Figure 3.8, Q is the arc heat input, which includes the factor of arc efficiency, η, in equation: $Q = \eta \cdot V \cdot I$. The parameters r_f and r_b are proportion coefficients representing heat apportionment in front and back of the heat source, respectively,

where $r_f + r_b = 2$ [7]. It is of great importance to note that, due to the condition of continuity of the overall volumetric heat source, the values of Q(x, y, z) given by equations [3.2] must be equal at the $x = 0$ plane. From this condition, another constraint is obtained for r_f and r_b, namely that $r_f/c_{hf} = r_b/c_{hb}$. Subsequently, the values for these two coefficients are determined as:

$$r_f = 2c_{hf}/(c_{hf} + c_{hb}) \text{ and } r_b = 2c_{hb}/(c_{hf} + c_{hb})$$

However, the double ellipsoidal heat source is described by five unknown parameters, which are the arc efficiency η, and the geometric parameters a_h, b_h, c_{hf} and c_{hb}. The arc efficiency (Figure 3.9) varies from 0.65 to 0.90 depending on the welding processes used, while the geometric parameters can be derived by experimental bead-on-plate procedure. Goldak [1] suggests that, after the experimental deposition of a welding bead on the base metal, measurements of the weld pool geometry can be used directly as an input to the parameters of the double ellipsoidal model. Radaj [2], accounting possible measurement errors and an overestimation of the weld pool shape, suggests that the geometric parameters of the model should be taken 10% less than those measured.
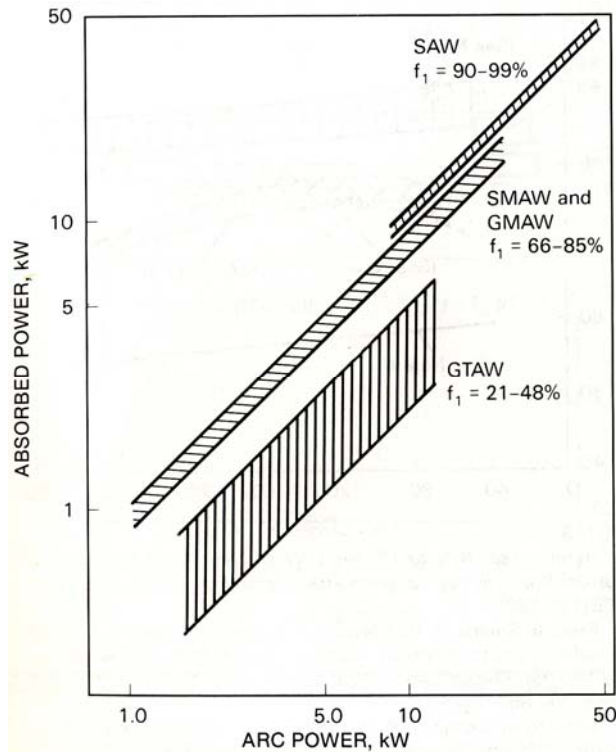
Figure 3.9 Arc efficiencies in SAW, GMAW, S<AW and GTAW [22,24]

The double ellipsoidal heat source model is the most complete heat source model until today. This is because all other heat source models can be derived from equations 3.2. Thus, Goldak's model encloses all other kind of heat source models and can be used with the appropriate simplifications, such as the consideration of a circle surface heat flux (Gaussian heat source model) instead of an ellipsoid.

3.3 Structural Analysis of Welding

The welding process affects the metals, to be welded, in many ways. The metals are subject to temperature fields that rapidly melt them (in the weld pool) and immediately cool them until they reach ambient temperature. During this thermal cycle, metallographic and material property changes occur, which along with other factors result into mechanical phenomena, such as residual stresses and distortion.

The formation of residual stresses during welding can be described by Figure 3.10, where a bead-on-plate weld is being deposited along line x-x.

The welding arc is moving at a velocity, v, and is presently located at the point O, as shown in Figure 3.10(A). In Figure 3.10(B) the temperature distributions, transverse to line x-x at locations A, B, C and D, are shown. Across section A-A, which is ahead of the welding arc, the temperature change, T, due to welding is essentially zero. However, the temperature distribution is very steep across section B-B, through the welding arc. At some distance behind the welding arc, along section C-C, the temperature distribution is much less severe. At a farther distance from the welding arc, the temperature across section D-D, has returned to a uniform temperature.
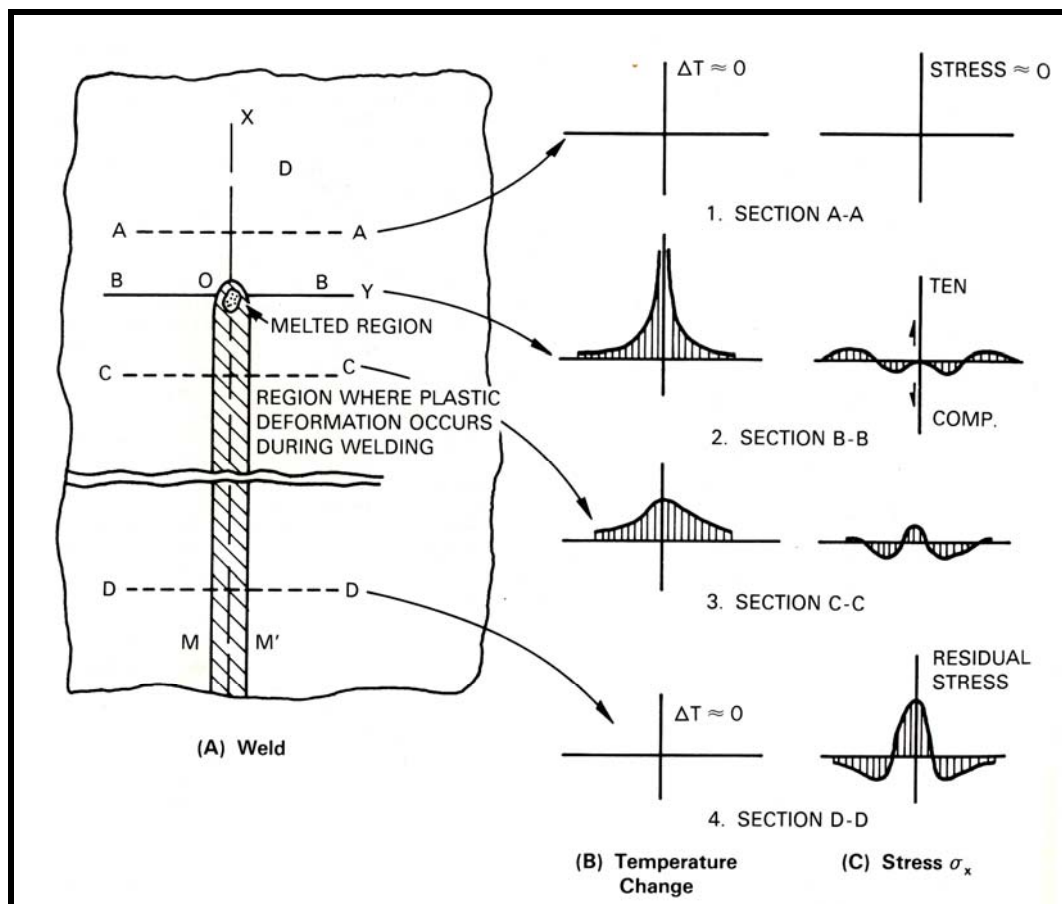
Figure 3.10 Distribution of temperature and stress during welding [22]

The distribution of stress σ_x, in the x-direction at sections A-A, B-B, C-C and D- is illustrated in Figure 3.10(C). Stress in the y-direction, σ_y, and shearing stress, τ_{xy}, also exist in a 2-dimensional stress field but are not shown here. At section A-A, thermal stresses due to welding are almost zero (Figure 3.10(C)-1). Stresses in regions below the weld pool at section B-B are nearly zero because the hot metal cannot support a load. Stresses in the heat-affected zones on both sides of the weld pool are compressive because the expansion of these areas is restrained by surrounding metal that is at lower temperatures. The metal temperature near the arc is high and the resulting yield strength is low. The compressive stresses will reach yield level at the temperature of the metal. The magnitude of compressive stress reaches a maximum with increasing distance from the weld. At some distance away from the weld pool, tensile stresses must balance with those compressive stresses in the heat-affected zones from equilibrium conditions. The instantaneous stress distribution along section B-B is shown in Figure 3.10(C)-2.

At section C-C, the weld metal and heat-affected zones have cooled. As they try to shrink, tensile stresses are balanced by compressive stresses in the cooler base metal. The stress distribution is illustrated in Figure 3.10(C)-3. The final condition of residual stresses is shown in section D-D. Along this section, high tensile stresses exist in the weld and heat-affected zones, while compressive stresses exist in base metal away from the weld (Figure 3.10(C)-4).

It is obvious that thermal stresses during welding are produced by a complex series of mechanisms that involve plastic deformation at a wide range of temperatures from ambient temperature to melting temperature.

Residual stresses are not necessarily created only during the welding process, but may have existed in the metal since its production. Within the fusion zone (FZ), the heat-affected zone (HAZ) and the adjacent parent metal, where the thermal softening and thermal strains caused by the heat flow from the weld are sufficient to cause yielding during welding, the residual stress field will be dominated by the weld-induced residual stresses. At greater distances from the weld, the residual stresses will be a function of the superposition of the weld-induced residual stresses and pre-existing residual stresses in the parts being joined. This superposition may be in the linear elastic or non-linear plastic, elastic-plastic or creep range, depending on the combined magnitude of the residual stresses and the mechanical properties of the parent metal [23].

Residual stresses before welding may be caused by thermal or mechanical processes during materials manufacturing or fabrication operations. Material- or product-manufacturing operations that cause significant residual stresses include casting, forging, rolling, heat treatments, quenching, straightening and carburization. Significant pre-welding fabrication processes include flame, plasma or laser-cutting, bending, machining, jigging and correction of misalignment.

In many material-manufacturing or fabrication operations, there is a rebalancing of the residual stresses during or after the application of the process and the magnitude of the final residual stresses is often less than half the yield strength of the material [23]. Some operations, such as heat treatment with slow cooling, may relax the stresses caused by previous operations. But processes, such as machining or rapid quenching which cause localized yielding at the surface, may leave yield magnitude stresses near the surface, possibly with enhanced yield strength due to wok hardening. The possibility of pre-existing residual stresses in welded structures should always be considered when the residual stresses in welded structures are being evaluated. But, as noted earlier, due to the high temperatures resulting in the weld pool and heat-affected zone areas, a re-distribution of the stress field occurs during welding. Thus, inside and near the weld seam the only residual stresses present are those resulting from the welding process.

Beside residual stresses, the welding process can cause distortional changes that affect the initial geometry of the structure. There are three fundamental dimensional changes resulting during welding [22,24]:

1. *Transverse shrinkage* that occurs perpendicular to the weld line
2. *Longitudinal shrinkage* that occurs parallel to the weld line, and
3. *Angular change* that consists of rotation around the weld line

These fundamental dimensional changes are responsible for the various types of distortion presented in Figure 3.11 are listed as:

1. Transverse shrinkage, which is shrinkage perpendicular to the weld line.
2. Angular change, resulting from uneven temperature distribution along the thickness direction.
3. Rotational distortion, namely angular distortion along the plate plane that is caused by thermal expansion.
4. Longitudinal shrinkage, which is shrinkage parallel to the weld line.
5. Longitudinal bending distortion, occurring on a plane which contains the weld line and it is perpendicular to the plate.
6. Buckling distortion that occurs in thin plates due to the presence of thermal compression stresses.
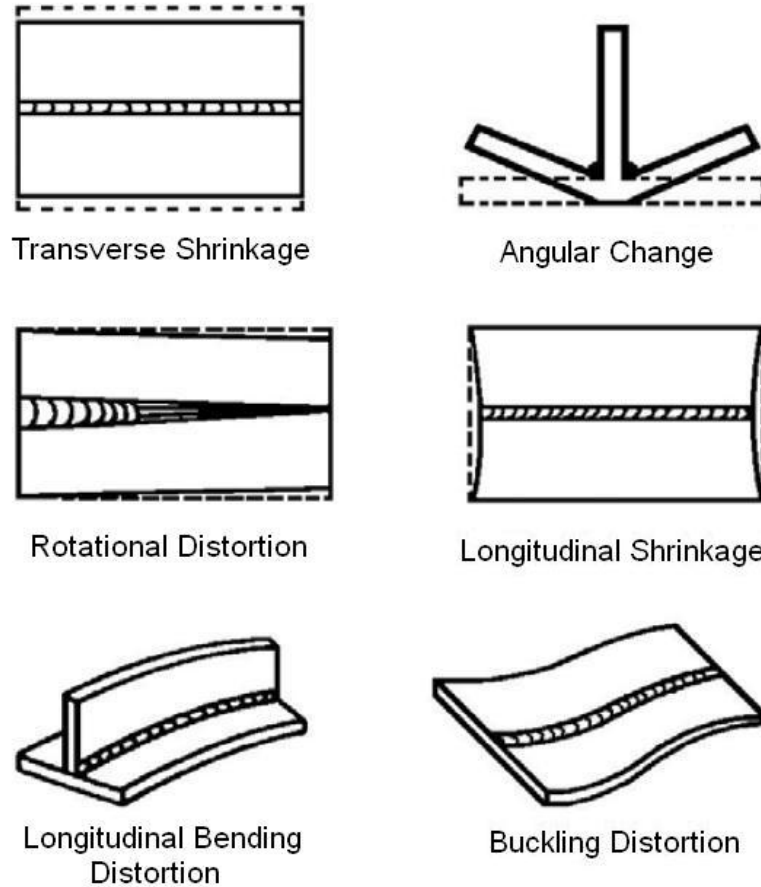
Figure 3.11 Typical types of distortion in welded structures

The basis of a structural analysis, which includes the prediction of residual stresses and distortion due to the welding process, is the temperature field simulated during the thermal analysis. The temperature change in solid bodies is associated with thermal strain. The total strain is determined by many factors, which are taken into account during a structural analysis. In the thermal-elastic-plastic constitutive models the total strain rate is decomposed into:

- The elastic, $\dot{\varepsilon}_{ij}^{e}$

- The plastic, $\dot{\varepsilon}_{ij}^{p}$, due to rate independent plasticity

- The thermal, $\dot{\varepsilon}_{ij}^{th}$, consisting of thermal expansion

- The creep strain rate, $\dot{\varepsilon}_{ij}^{c}$

- The strain rate volume, $\dot{\varepsilon}_{ij}^{TrV}$, associated with phase transformations

- The strain rate transformation plasticity, $\dot{\varepsilon}_{ij}^{TrP}$

The volume change associated with phase transformations is often included as part of the thermal strain by modifying the coefficient of thermal expansion [1].

The participation of all strain factors is necessary in analytical models and in the case of phase transformation effects during solidification and cooling [10-12]. However, when transformation phenomena are not present, or the fraction of the phase transformed is very small, simplifications can be made.

Similar to the thermal analysis, temperature-dependent mechanical properties of the material must be defined (Figures 3.12 and 3.13). This is due to the high temperatures and high thermal gradients that are present during welding and are used as the input load for the structural analysis. Hence, in order to perform a structural analysis and obtain results for the residual stresses and distortion the material properties required are the following:

- ✓ Thermal expansion coefficient, α [1/°C]
- ✓ Elastic modulus, E [N/mm²]
- ✓ Poisson's ratio, v [-]
- ✓ Yield limit, σ_y [N/mm²]
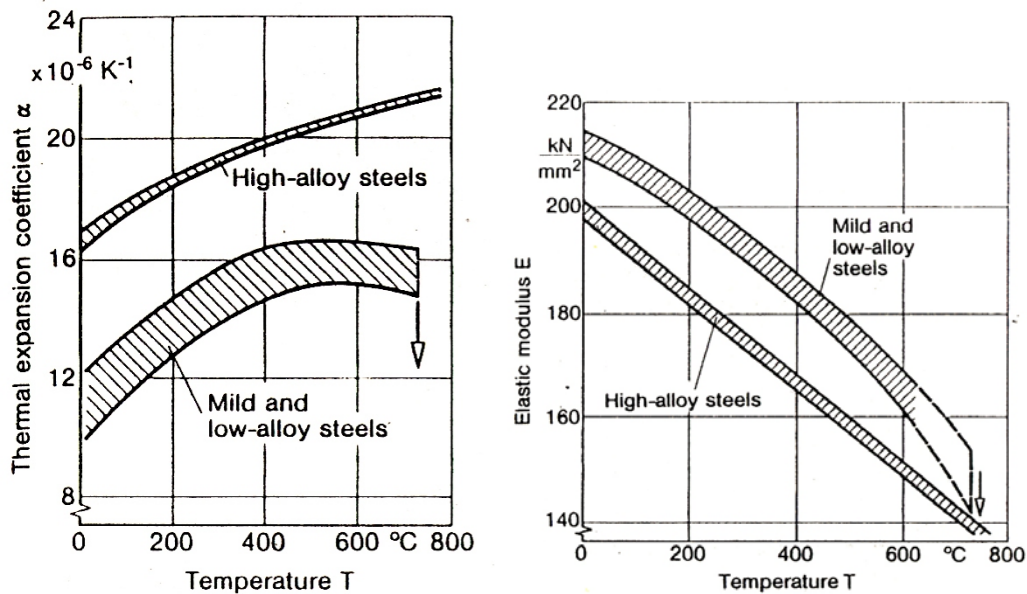
Figure 3.12 a) Thermal expansion coefficient and b) Elastic modulus [2]
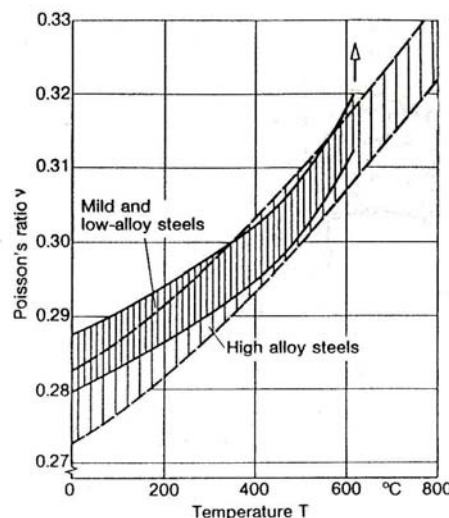
Figure 3.13 Poisson's ratio as a function of temperature [2]

In Figure 3.12, the temperature dependent mechanical properties of thermal expansion and elastic modulus are presented, while in Figure 3.13, Poisson's ratio is displayed as a function of temperature. It can be observed that the Elastic modulus decreases dramatically at high temperatures, while Poison's ration exhibits an increment of 20% with respect to its ambient temperature initial value. The thermal expansion coefficient, which is the main factor determining the distortion in welded structures, increases at high temperatures for the high-alloyed steels (mostly stainless steels).

3.4 2-D and 3-D finite element simulations

As noted earlier, the Finite Element Analysis was employed to help the research engineers simulate welding procedures and predict the residual stresses and distortion that result from these kinds of thermo-mechanical procedures. CMW are relying, for the past 30 years, on computers. The development of even more powerful computers during the past years allows simulations to become even more detailed and accurate. In the past years "heavy" models and simulations were forcing the researchers to simplify their models and lead them to admissions that constrained the simulation solution and accuracy.

This is why the first models built were two dimensional models (2D). With the 2D models, the welding procedure was, usually, examined in a cross sectional plane. The employment of plane elements was found useful and within the ability of the CPUs at that time. With time, the meshing of the finite element 2D models became thinner and large volumes of plane elements were applied to produce even more accurate solutions. Brickstad and Josefson [13] built several 2D models and ventured a parametric study on the multi-pass welding of austenitic stainless steels, elaborating several meshing techniques. They managed to model 36 passes on a 40 mm thick stainless steel pipe (Figure 3.14).
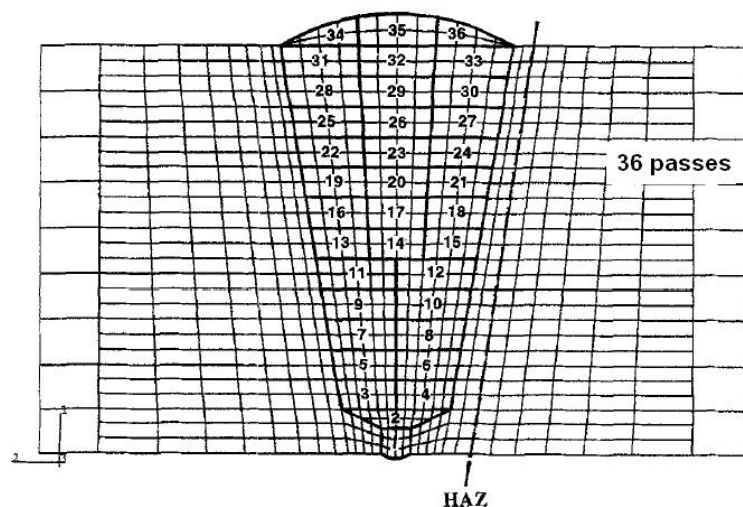

Figure 3.14 The 2D model of Brickstad and Josefson [13]

The need for three-dimensional models that would be able to provide the engineers with a spatial overlook of the welding procedure was the onset for techniques and methods that would be able to produce 3D models, but without increasing the CPU-time. Lindgren et al [14] employed an automatic remeshing technique for 3D models, which reduced the required CPU-time to solution and resulted in no loss in accuracy. This is the trend in welding simulation for the past years, since 3D simulations became a common task in CMW, namely how to reduce the time-to-solution without any loss of accuracy.

Despite the new model built-up techniques of FEA and the existence of even more powerful computers, the 2D models are still in use. Deng and Murakawa [15] constructed both 2D and 3D models for multi-pass welding of stainless steel pipes and used experimental results in order to evaluate them. They have shown that both 2D and 3D are accurate, despite the fact that 2D models are not able to provide detailed information; a lot of computational time can thus be saved. In addition, in the 2D models one can simulate the welding heat source, for the specific plane section, almost as an analytical function. This can be accomplished, since the mesh has the ability to become extremely thin, without costing in CPU-time, and the heat load can be applied almost as a continuous function. This was the case in the work of Taljat et al. [10], where a 2D model with a very thin mesh was built, in order to simulate a spot GTA weld and observe the phase transformations and residual stresses that resulted.

The application of an almost continuous function of the welding heat source in 3D models has not been completely accomplished yet. This is due to the very thin mesh requirement, in order to approach the continuous function of the welding source. The FE code SYSWELD® has developed an adaptive meshing technique (Figure 3.15), where a very thin mesh travels across the weld line with the welding heat source. This technique has been shown by Duranton et al. [16] using SYSWELD®, which is a closed code FE program and any modifications or additions from the users is not possible.
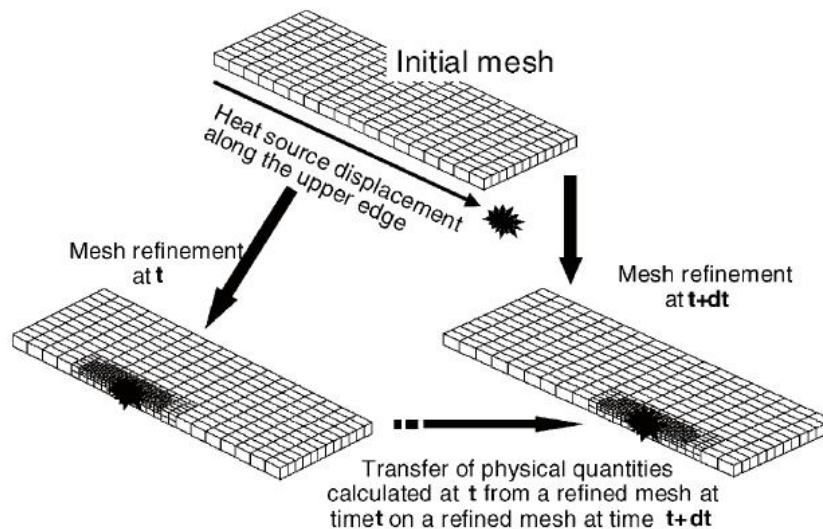

Figure 3.15 The adaptive meshing procedure of SYSWELD [16]

So far, during 3D welding simulations, the heat source is, usually, applied as a body force (Figure 3.16), in the form of heat flux, and sometimes a surface load resulting from the welding arc is also added [18,19]. Although this technique has no CPU-time cost, it is still not widely applied to 3D multi-pass welding simulations. The multi-pass welding simulations are still, mostly, performed by 2D FE analyses [11, 20] for two reasons. Firstly, the CPU-time cost for 3D analyses is considered to be high and secondly, the method that simulates the multi-pass weld metal addition still has flaws, which affect the accuracy of the prediction.
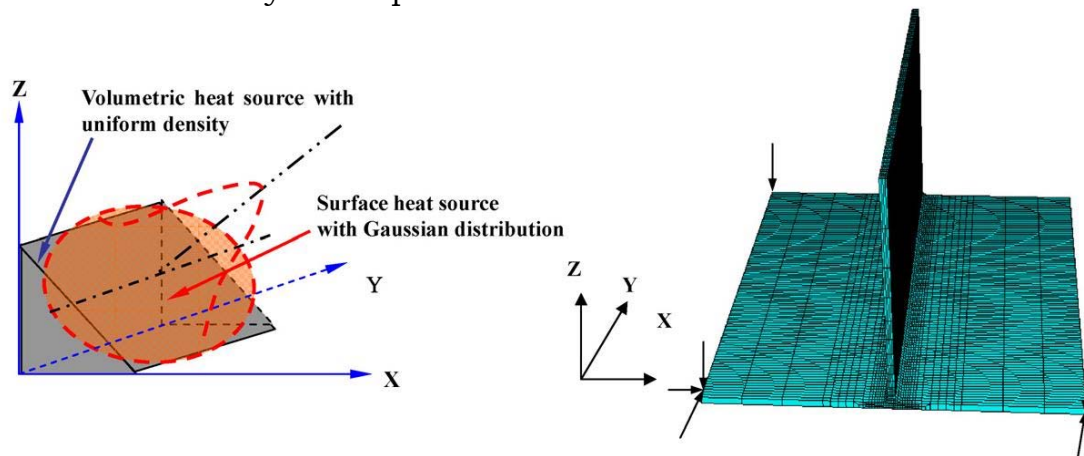
Figure 3.16 The application of a volume heat source as a body force combined with a surface load in single pass fillet weld [18]

Except multi-pass welding, there were other fields of interest that engineers attempted to simulate by the FE analysis. One of them is the welding process of large structures (e.g. stiffener sections). The case of section welding can be described as a summation of many welding processes together. The assumption made by some researchers to consider axisymmetry in this kind of welding simulations was entirely incorrect. The 3D simulation of sections must follow a specific welding sequence, which has no geometric symmetry and is an extreme time-depended phenomenon; otherwise the modeling of the mechanical phenomena will be completely erroneous. Finite element programs, such as ABAQUS® and ANSYS®, have incorporated subroutines and modules that can help the simulation engineers to perform this kind of analyses without increasing the total CPU-time cost. Lindgren [17], recapitulating the CMW efforts until the present date, ventured the numerical simulation of a section, using the ANSYS® code, and employing the module of sub-structuring. The exact same work was presented by Deng et al. [21], using the ABAQUS® code, and the exact same module. In their work, Deng et al, broke down the section to be welded and specified three groups of welded joints. After the separate simulation of each welded joint, the three models were used as input to the section simulation (Figure 3.17), which took account of the loads, boundary conditions and constrains of all three models and produced the

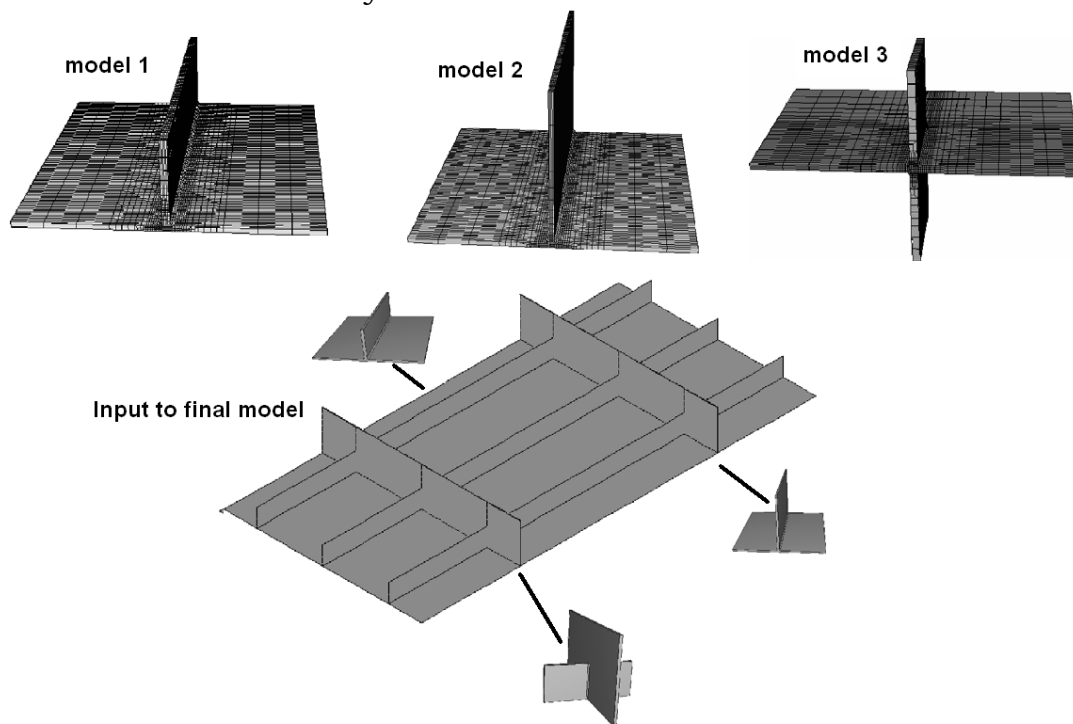welding residual stresses and deformation of the whole welded section with sufficient accuracy.

Figure 3.17 The three separate welding models and the addition with the sub-structuring technique to the final model of the welded section [21]

Hence, the sub-structuring module, employed by the finite element programs, can be used to solve several problems and then combine them in a final solution, where every problem interacts with the others. Thus, if a large section with a number of weld seams is to be simulated, the weld seams can be solved independently and then inputted to the final overall simulation, where the FE solver will consider all separate solutions and their interaction to each other and produce the final solution. This was considered, so far, one of the greatest innovations in the 3D model simulation in welded structures.

Chapter Bibliography

1. J. A. Goldak, M. Akhlaghi, 2005, *Computational Welding Mechanics*, Springer Science + Business Media, Inc.
2. D. Radaj, 1992, *Heat Effects of Welding – Temperature field, Residual Stress, Distortion*, Springer-Verlag
3. Sindo Kou, *Welding Metallurgy*, 2nd Edition 2003 John Wiley & Sons Inc.
4. D. Rosenthal, 1946, *The theory of moving sources of heat and its application to metal treatments*, Trans. ASME Vol. 68, pp. 849-865
5. R. R. Rykalin, 1974, *Energy sources for welding*, Welding in the World Vol. 12 No. 9/10, pp. 227-248
6. V. Pavelic, R. Tanbakuchi, O. A. Uyehara, P. S. Mayers, 1969, *Experimental and computed temperature histories in gas tungsten arc welding of thin plates*, Welding Journal 48(6), pp. 295s-305s
7. J. A. Goldak, A. Chakravarti, M. Bibby, 1984, *A finite element model for welding heat sources*, Metallurgical Transactions B, Vol. 15B, pp. 299-305
8. N. T. Nguyen, A. Ohta, K. Matsuoka, N. Suzuki, Y. Maeda, 1999, *Analytical Solutions for transient temperature of semi-infinite body subjected to 3-D moving heat sources*, Welding Journal, pp.265s-274s
9. N. T. Nguyen, Y. –W. Mai, S. Simpson, A. Ohta, 2004, Analytical approximate solution for double ellipsoidal heat source in finite thick plate, Welding Journal, pp.82s-93s
10. B. Tajlat, B. Radhakrishnan, T. Zacharia, 1998, Numerical analysis of GTA welding process with emphasis on post-solidification phase transformation effects on residual stresses, Materials Science and Engineering Vol.A246, pp.45-54
11. Dean Deng, Murakawa Hidekazu, 2006, *Prediction of welding residual stress in multi-pass butt-welded modified 9Cr-1Mo steel pipe considering phase transformation effects*, Computational Material Science Vol.37, pp. 209-219
12. Dean Deng, 2009, *FEM prediction of welding residual stress and distortion in carbon steel considering phase transformation effects*, Materials and Design Vol.30, pp. 359-366
13. B. Brickstad, B. L. Josefson, 1998, *A parametric study of residual stresses in multi-pass butt-welded stainless steel pipes*, International Journal of Pressure Vessels and Piping Vol.75, pp. 11-25
14. L.-E. Lindgren, H.-Å. Häggblad, J. M. J. McDill, A. S. Oddy, 1997, *Automatic remeshing for three-dimensional finite element simulation of welding*, Computational Methods in Applied Mechanics and Engineering Vol.147, pp. 401-409
15. Dean Deng, Hidekazu Murakawa, 2006, *Numerical simulation of temperature field and residual stress in multi-pass welds in stainless steel pipe and comparison with experimental results*, Computational Materials Science Vol.37, pp. 269-277
16. P. Duranton, J. Devaux, V. Robin, J. M. Bergheau, 2004, *3D modeling of multipass welding of a 316L stainless steel pipe*, Journal of Materials Processing Technology Vol.153-154, pp. 457-463
17. L.-E. Lindgren, 2006, *Numerical modeling of welding*, Computer Methods in Applied Mechanics and Engineering Vol.195, pp. 6710-6736
18. Dean Deng, Wei Liang, Hidekazu Murakawa, 2007, *Determination in fillet-welded joint by means of numerical simulation and comparison with*

experimental measurements, Journal of Materials Processing Technology Vol.183, pp. 219-225

19. G. A. Moraitis, G. N. Labeas, 2008, *Residual stress and distortion calculation of laser beam welding for aluminum lap joints*, Journal of Materials Processing Technology Vol.198, pp. 260-269

20. Dean Deng, Hidekazu Murakawa, Wei Liang, 2008, *Numerical and experimental investigations on welding residual stress in multi-pass butt-welded austenitic stainless steel pipe*, Computational Materials Science Vol.42, pp. 234-244

21. Dean Deng, Hidekazu Murakawa, Wei Liang, 2007, Computational Methods in Applied Mechanics and Engineering Vol.196, pp. 4613-4627

22. *Welding Handbook 8th Edition – Volume 1, Welding Technology*, 1998 - The American Welding Society

23. R. H. Leggatt, 2008, *Residual stresses in welded structures*, International Journal of Pressure Vessels and Piping Vol.85, pp. 144-151

24. V. J. Papazoglou, G. Papademetriou, 1994, *Welding Science and Technology (in Greek)*, Publications of NTUA

3D Numerical Modeling of Austenitic Stainless Steel 316L Multi-pass Butt Welding and Comparison with Experimental Results

4th Chapter

Numerical Simulation of Austenitic SS 316L

4. Numerical Simulation and Experiments of Austenitic Stainless Steel AISI 316L Butt Welding

In the present master thesis, numerical simulation of the butt welding of austenitic stainless steel plates Type AISI 316L is attempted, together with a comparison with experimental results. The selected material belongs to the austenitic L-grades (low carbon) stainless steels, to which its good resistance to corrosion is attributed. Fields of its application are mostly the petrochemical and marine industries, without restraining other services. The low carbon content, as noted in earlier chapters, ensures the avoidance of Cr-rich carbide ($M_{23}C_6$) precipitation in the heat-affected zone, even during multi-pass welding processes, where the constant re-heat, after every welding pass, would normally promote the carbide precipitation.

4.1 Experimental procedure and results

Experiments of multi-pass butt welding of austenitic stainless steel AISI 316L were carried out in the Shipbuilding Technology Laboratory, in the School of Naval Architecture and Marine Engineering at the National Technical University of Athens. Austenitic stainless steel 316L was selected, since it is a widely used material in the marine industry. During welding, 316L experiences almost no transformation and it can be considered as a single phase material.

4.1.1 Description of experimental equipment and procedure

The welding process used, was the Flux Cored Arc Welding (FCAW) method. The whole procedure was automated with the use of a welding robot (Figure 4.1) with 6 degrees of freedom, manufactured by IGM® Robotersysteme.

Figure 4.1 The welding robotic arm

A gas metal arc welding machine (Figure 4.2a), manufactured by Fronius®, attached to the robotic system was used to provide the welding current and voltage. The machine's nominal power is at 380 A, and for this reason a water-cooling gun is used, avoiding overheating. An automatic wire-feeder (Figure 4.2b), attached to the robotic arm, has lead the flux cored wire at a constant feeding-speed through the welding gun and into the weld pool.

Figure 4.2 a) The constant voltage GMAW machine and b) the wire-feeder attached to the robotic arm

During welding, an argon gas mixture was used to establish a shielding environment around the weld pool. The gas mixture used was Ar 82% + CO_2 18% (EN 439 – M21) and is led to the gas nozzle of the welding gun from a high pressure bottle (Figure 4.3). The gas flow was regulated at a constant value of 18 l/min.

Figure 4.3 The shielding gas regulators

The base and filler metal's compositions were similar and are presented in Table 4.1. The flux cored metal wire was manufactured by Böhler®, had a diameter of 1,2 mm and abides to the European standard EN 12073 - T 19 12 3 L R M (C) 3. The similar composition of the base and filler metal would ensure the formation of a single-phase austenitic stainless steel weld metal, with a small amount (max 10%) of retained δ-ferrite.

Table 4.1 Composition of base and filler metal for AISI 316L
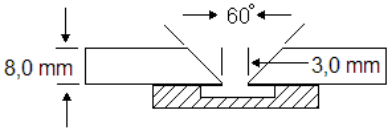
	C	Si	Mn	P	S	Cr	Mo	Ni	N	Cu	Fe
Base Metal	0.024	0.38	1.39	0.032	0.004	16.97	2.02	10.09	-	-	Bal
Filler Metal	0.029	0.78	1.38	0.022	0.008	19.07	2.60	11.94	0.024	0.17	Bal

Two series of experiments were carried out. The difference between them was the plate's length and width dimensions, while the plate thickness was in both cases 8 mm. The plates from the first series were 350x150 mm^2 (*Welding Samples A-series*) and the ones from the second series 700x300 mm^2 (*Welding Samples B-series*). In order to optimize the welding procedure, a series of bead-on-plate tests (Figure 4.4) were carried out, resulting in the selection of the optimum welding conditions, posted in Table 4.2. Due to the thickness dimension of the plates, a beveling treatment was performed, as shown in Table 4.2.

Figure 4.4 Bead-on-plate tests on scrap plates of AISI 316L

Table 4.2 Welding conditions and plate beveling

Voltage (V)	Welding Current (A)	Welding speed (cm/min)	Shielding gas flow (l/min)	Passes
24	160	30	18	3

The beveling treatment was conducted through the whole thickness dimension, creating a 60º angle groove, in order to obtain a

V shaped weld metal. The use of a ceramic back-strip was necessary, since, after tack welding with the SMAW method (Figure 4.5), a 3 mm root gap was created to establish a convex root shape. During welding of both the A- and B-series plates, clamps were used to constrain one plate of the welded joint, while the other plate had no constrains at all.

(a)   (b)

Figure 4.5 a) Tack welds with the SMAW method and b) tack welded plates for A-series experiment

The A-series of welding experiments was part of a diploma thesis [2] and the B-series part of a master thesis [1]. During the conduction of the A-series experiments, measurements of the welding thermal cycles were carried out with the use of type-K thermocouples (Figure 4.6).

Figure 4.6 Temperature measurements in A-series plates with the use of Type-K thermocouples

After the experimental determination of the thermal cycle, for all three welding passes, the welded plates were used for metallographic examination and micro-hardness tests. At the same time, with the use of the Finite Element program ANSYS®, a 3D model was constructed

to numerically simulate the thermal cycles of the A-series experiments. This model will be referred in the following sections as Model-A.

During the conduction of the B-series experiments, several transient phenomena were experimentally measured with a series of Spider8 ADCs (Figure 4.7) manufactures by HBM®. The thermal cycles, the deformation and distortion during the welding process were measured from the onset of the first welding pass until the complete cooling of the welded joint to ambient temperature. Similarly to the A-series measurements, Type-K thermocouples were used to determine the thermal cycles, while LVDTs and strain gauges were employed to measure the transient vertical deformation and the transient strains respectively. The setup of the measurement instruments on the B-series plates is presented in Figure 4.8.
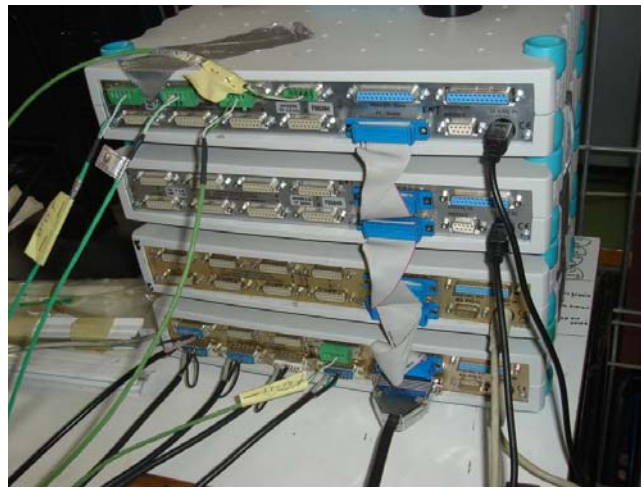
Figure 4.7 The 4-set of Spider8® ADCs
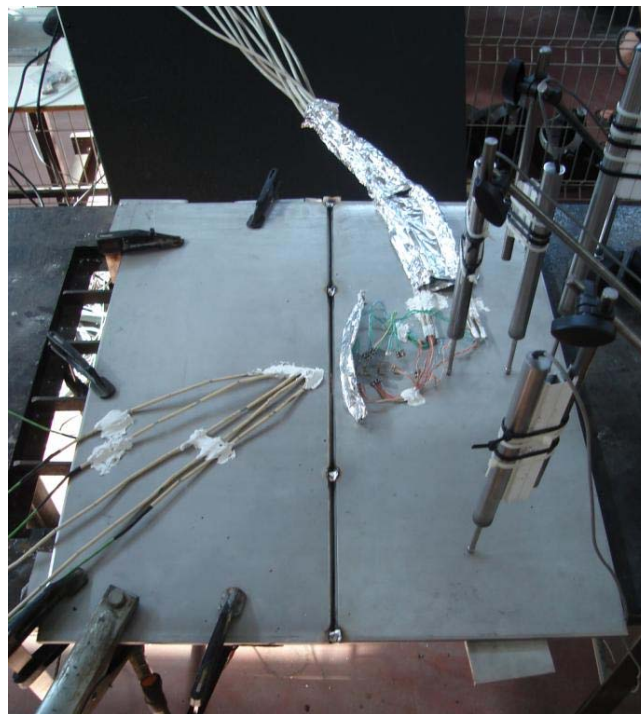
Figure 4.8 The experimental setup for the B-series experiments

The as-welded B-series austenitic stainless steel plates were used for the experimental measurement of the residual stresses that resulted from the welding procedure. The measurement method, to determine the residual stresses, used was the hole-drilling method of Mathar-Soete, with the application of rosette strain gauges (Figure 4.9) on the surface of the as-welded plates, connected to ADCs.
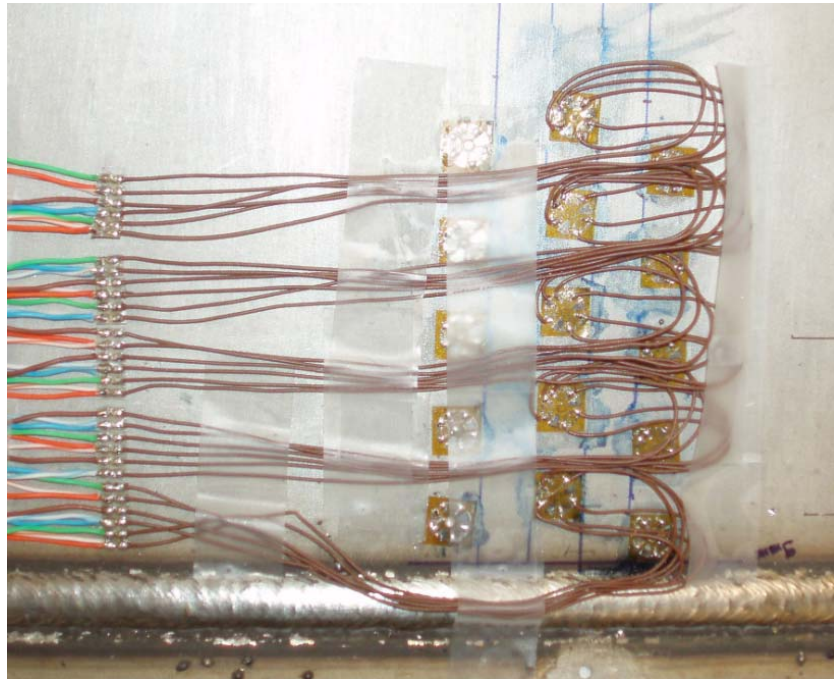
Figure 4.9 The setup of the rosette strain gauges

Similarly to the A-series experiments, a finite element model was constructed with the ANSYS® FE code, in order to perform a thermo-mechanical simulation of the B-series multi-pass welding procedure. This model will be referred in the following sections as Model-B.

4.1.2 Experimental results

Measurements of the thermal cycles during the 3-pass welding of austenitic stainless steels were carried out for the A-series plates. Five Type-K thermocouples were positioned, on the top surface of the A-series stainless steel plates, in 15, 25, 35, 55 and 75 mm distance from the weld line. The onset of the measurements was at the beginning of the first pass, while the end of the experiment was when the readings from all thermocouples was practically the same and have reached a certain barrier. The thermal cycles measured are shown in Figure 4.10. It is noted that the highest measured temperature, reaching approximately 332 °C, occurred during the deposition of the 2nd welding pass and the reading came from the thermocouple which was nearest to the weld pool. A new pass was commencing when the temperature reading of the 1st thermocouple (15 mm from the Weld Line) was below 100 °C.
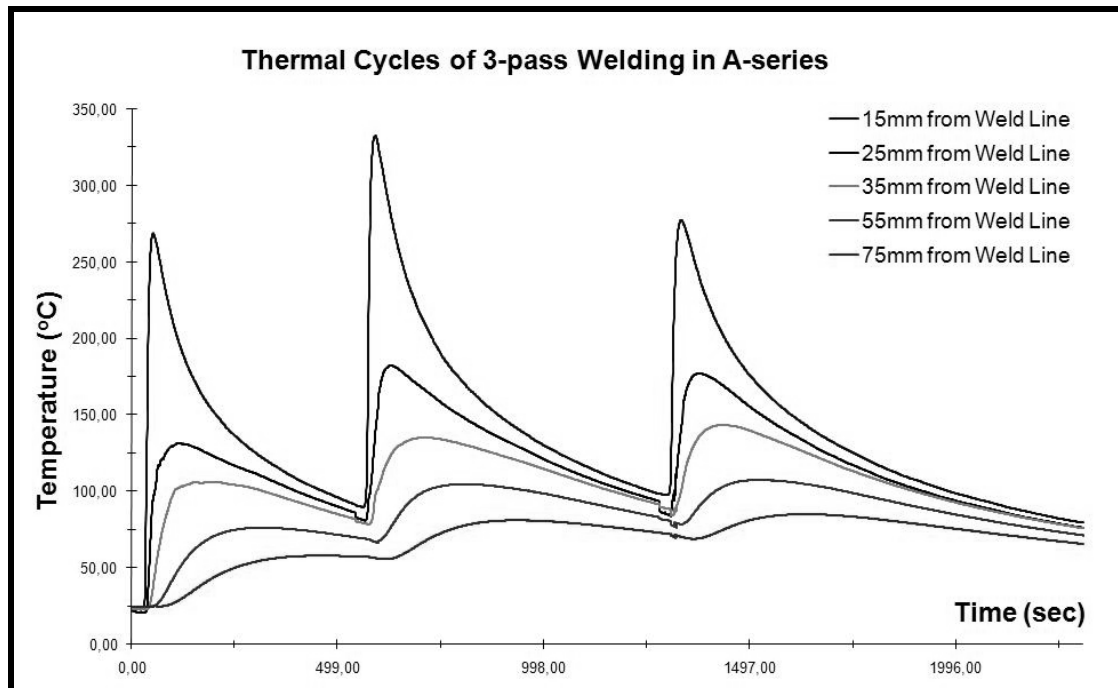
Figure 4.10 Thermal cycle measurements from the A-series experiment [2]

Similar to the A-series, the thermal cycles of the B-series multi-pass welded austenitic stainless steel plates were measured. Type-K thermocouples were positioned at the same distances from the weld line, as in the A-series experiment. The measured thermal cycles are shown in Figure 4.11.
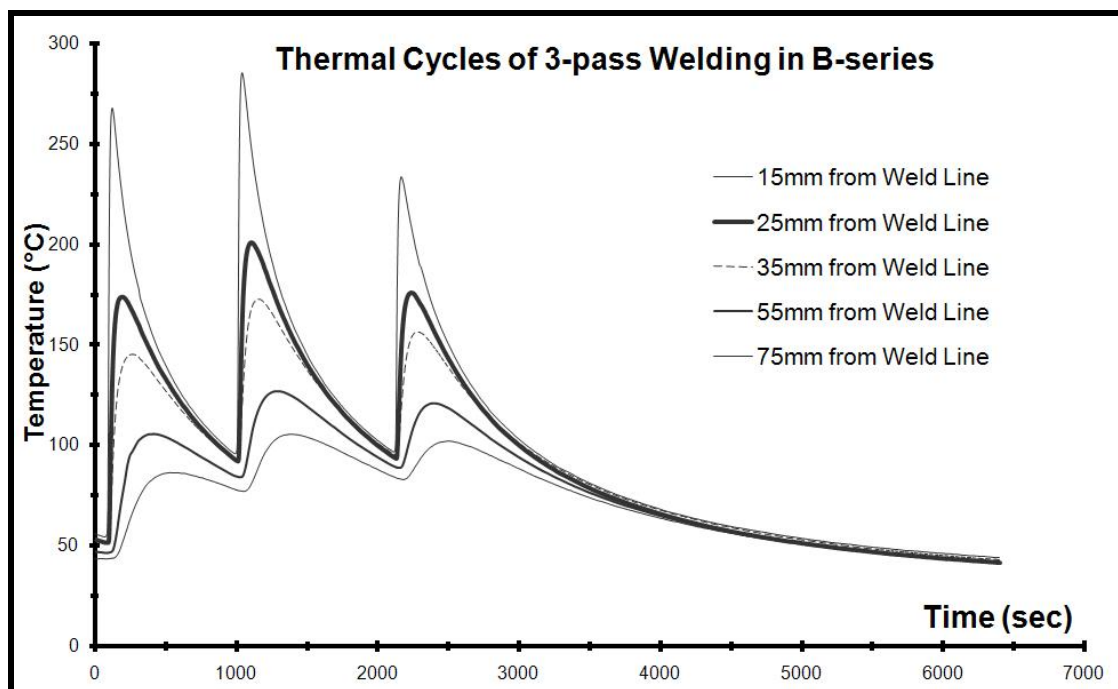

Figure 4.11 Thermal cycle measurements from the B-series experiment [1]

The highest measured temperature was again observed during the deposition of the 2nd weld pass from the thermocouple nearest to

the weld line (15 mm). The reading for that temperature was approximately 285 °C. Every new pass was deposited when the temperature reading of the 1ˢᵗ thermocouple was below 100 °C.

General remarks to the thermal cycle figures from the A- and B-series experiments would be the relatively low temperature readings, even from the thermocouple adjacent to the weld line, and the fast cooling rates. Both these remarks can be justified from the thermal properties of the austenitic stainless steel grades. The low thermal conductivity and the high thermal diffusity of the austenitic grades, in comparison to the other steel grades, are responsible for the relatively low temperatures and the fast cooling rates, respectively. Another reason for the above remarks would be the FCAW method used, which can produce fine welds at higher welding speeds than most other arc welding methods.

Comparing the thermal cycles from both series, it can be observed that the temperatures and cooling rates of the B-series are lower to that of the A-series. The reason for these differences is the dimensional dissimilarity between the two series. The B-series plates are two times larger, in both length and width, than the A-series plates. The dimensional dissimilarities, in association with the thermal properties of the 316L austenitic grade, are the reason of these differences.

Simultaneously with the thermal cycle measurements, four LVDTs, which were positioned on the top surface of the unconstrained plate, were measuring the vertical displacement of the plate during the multi-pass welding and upon cooling. Three of the LVDTs were positioned in the middle length of the plate and at 150, 200 and 250 mm distance from the weld line, while the fourth was set at 100 mm from the start end of the plate and at 150 mm away from the weld line, as shown in Figure 4.12.
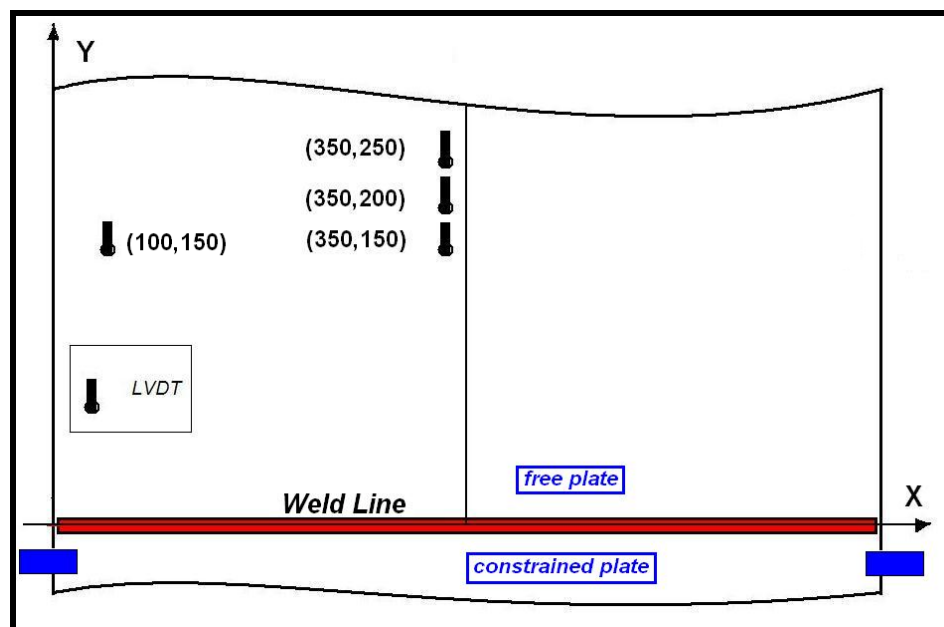
Figure 4.12 Schematic representation of the of the LVDT's positions on the free plate

The continuous measurements of the LVDTs are presented in Figure 4.13, where it can be readily noted that the farther the LVDT from the weld line is placed the higher the vertical displacement is. This behavior is expected, due to the angular change that occurs during butt welded joints.
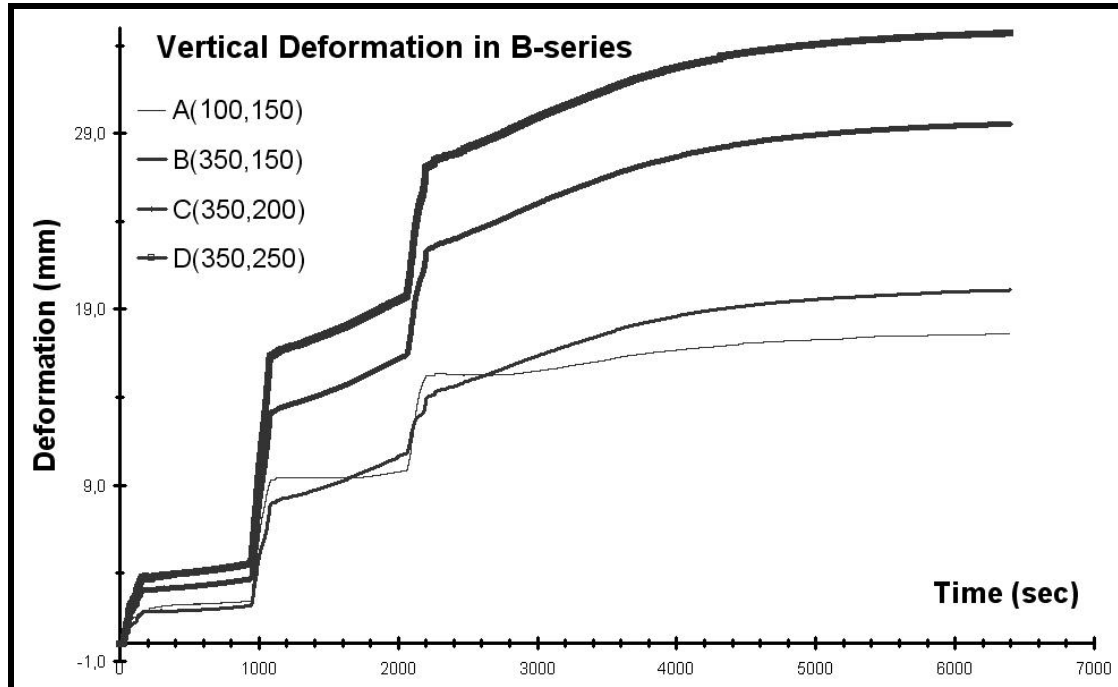

Figure 4.13 Vertical deformation of the free plate in B-series [1]

Another remark is that the deformation rate increases every time a new weld pass is deposited. This is due to the high temperature gradients that amplify the effect of the thermal expansion coefficient at that time. The A and B points, even if they are positioned at equal distances from the weld line, exhibit different deformation behavior. The reason for that is the different longitudinal position of the LVDTs. The A-point LVDT is positioned almost at the beginning of the plate's length, while the B-point LVDT at the middle. The longitudinal shrinkage of the butt welded joint results in this behavior and, hence, to a difference in the final vertical deformation. The constant overlapping of the A and B curve is observed every time a new pass is deposited. The response of the A-curve to high deformation rates from the welding passes occurs sooner because the welding arc, travelling along the weld line, crosses the x-coordinate of A-point first and the x-coordinate of the B-point after approximately 60 sec. As a result of this time interval, an overlapping of the two curves occurs.

Having the in-situ measurements fulfilled and processed, the plates of the B-series were subjected to residual stress measurements with the hole-drilling method, as shown in Figure 4.9. Due to the convex surface of the weld metal, the measurements start from the heat-affected zone region and range until 100 mm from the weld metal. In Figure 4.14 the residual stress measurements, in the principal x-direction, are presented.
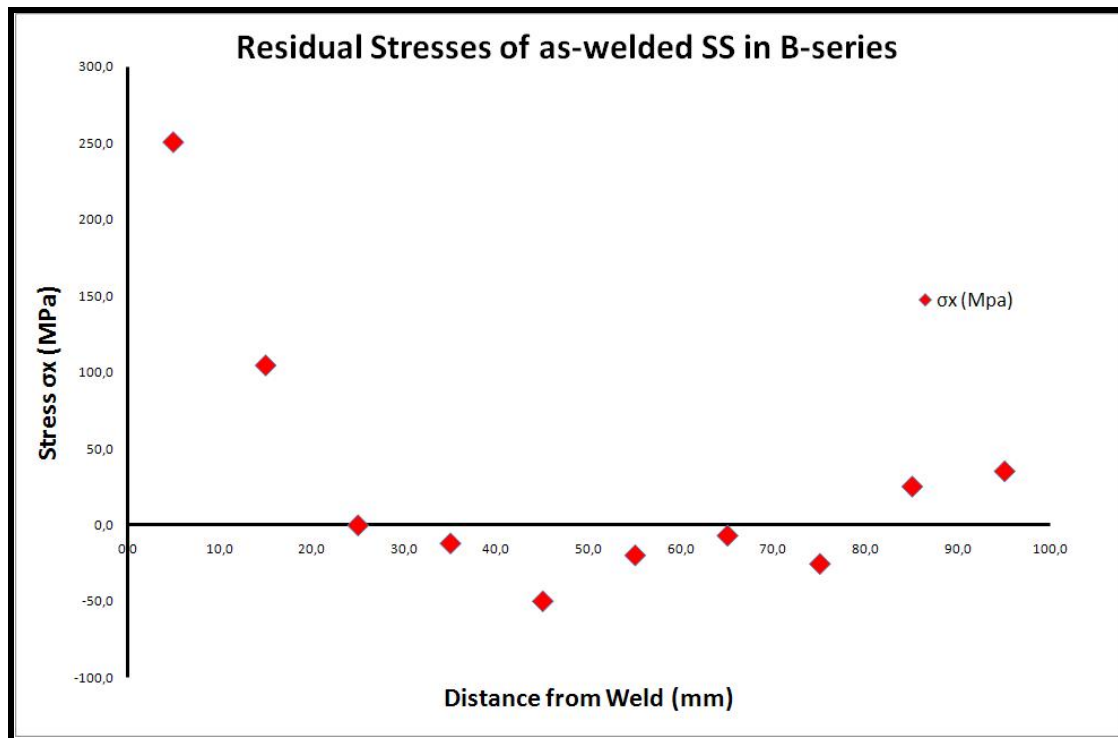
Figure 4.14 Residual stress measurements [1]

Near the fusion zone high tensile stresses are observed. These stresses tend to zero, as the distance from the weld line increases. At the distance of 25 mm, the tensile stresses are zero and at a farther distance transformed to compressive stresses, of moderate magnitude. As the distance increases, the compressive stresses are shifting to tensile stresses, of moderate magnitude.

The residual stresses transverse profile, presented in Figure 4.14, is considered to have the common form, described in the previous chapter. A significant characteristic of this profile would be the relatively wide range of the tensile stresses near the weld metal. This kind of profile is very common among the austenitic stainless steel grades.

4.2 Simulation Model built-up

As noted in the previous paragraph, two simulation 3D models were constructed, in order to perform thermo-mechanical analysis for the A- and B-series multi-pass welding experiments. The ANSYS® finite element code was used in both cases. The same philosophy in the construction of A and B models was used, since the only difference between them was the dimensions. All input files were practically the same, except the "parameter" file, in which the geometric parameters of the models were registered. Temperature dependent thermal and mechanical properties were employed in order to enhance accuracy to the model results, since the high temperatures and temperature gradients affect greatly the material properties and the material model behavior. The simulation of the welding arc was

performed with the use of a moving volumetric heat source. The filler metal addition was modeled with an ANSYS® module, known as the "element of birth and death".

4.2.1 Geometry of the Model

Models A and B were geometrically constructed in the same manner. Five different volume-groups were considered for each model. The first three volumes represented the welding pass deposits, while the other two groups represented the adjacent and remote volumes of the weld, respectively. The finest mesh was constructed in the weld metal region. In the adjacent weld area, representing the heat-affected zone, the mesh became coarser, while in the remote region the mesh ended up to be quite thick. The meshed models A and B are presented in Figure 4.15.

(a)

(b)
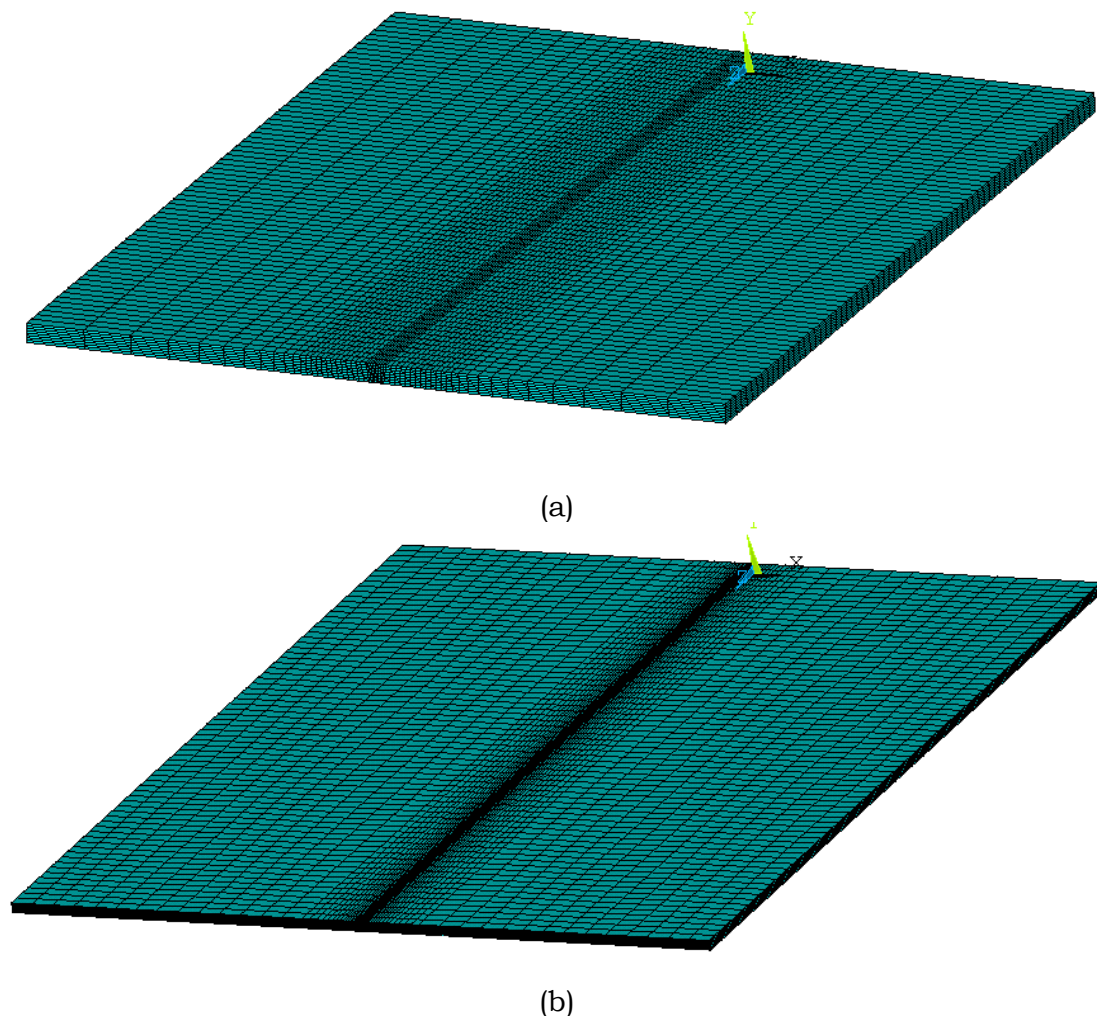
Figure 4.15 a) Meshed model-A, and b) meshed model-B

The element type, which was employed for the thermal analysis of both models, was the ANSYS® SOLID70 3D solid element (Figure

4.16a), which has a 3D thermal conduction capability. This element has eight nodes, with temperature being the only degree of freedom at each node and it can be applied to a 3D steady-state or transient analysis. For the structural analysis, following the thermal analysis, the element type had to be changed to the ANSYS® SOLID185 3D solid element (Figure 4.16b), which is used for 3D modeling of solid structures. It is defined by eight nodes having three degrees of freedom at each node, namely translations in the nodal x, y and z directions. The element has plasticity, hyper-plasticity, stress stiffening, creep, large deflection and large strain capabilities. It also has mixed formulation capability for simulating deformations of nearly incompressible elastoplastic materials and fully incompressible hyperelastic materials.

(a)

(b)
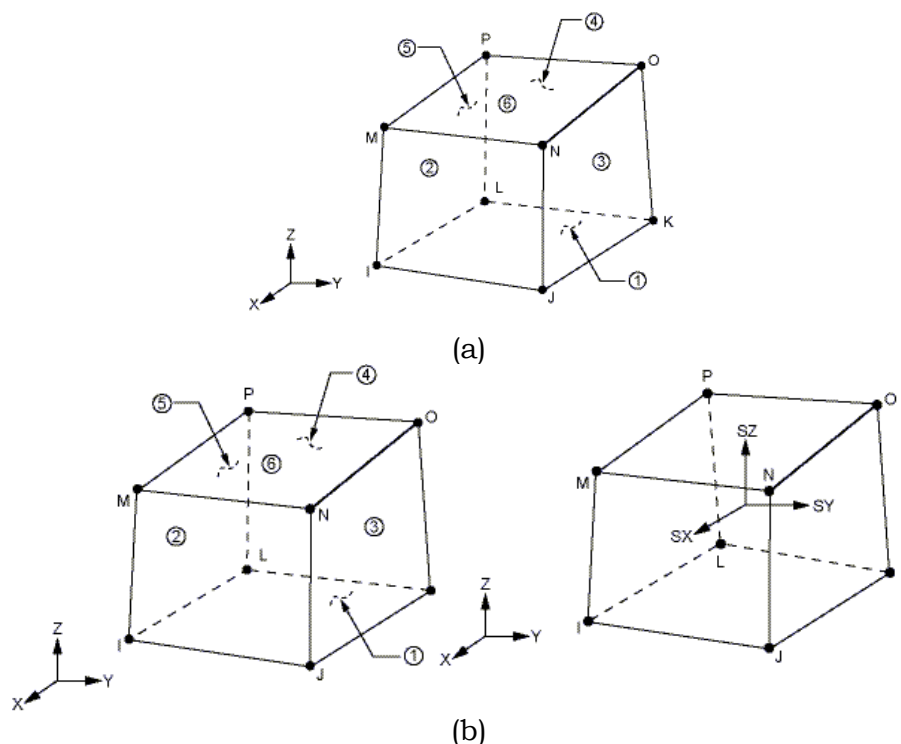
Figure 4.16 a) The SOLID70 element and b) the SOLID185 element

When a coupled field analysis is performed in ANSYS®, the elements used in the primary analysis field must be in good agreement with the elements used in the secondary analysis field. The element SOLID185 was chosen, due to the coupled structural-thermal analysis, as the corresponding element of the SOLID70 element.

The amount of nodes and elements for each model had no large variation, due to the employment of a parametric geometry. Hence, model-A had 31360 elements and 36423 nodes, while model-B had 35840 elements and 41535 nodes. The geometry and the mesh of the models during the transition from the thermal to the structural field had to be preserved.

4.2.2 Thermal Properties of Austenitic Stainless Steel 316L

As described in the previous chapter, in order to perform an accurate thermo-mechanical analysis in welding, the use of temperature dependent properties is necessary. The thermal properties required to conduct a thermal analysis are the thermal conductivity, the specific heat and the density of the material. These properties are presented in Figure 4.17.
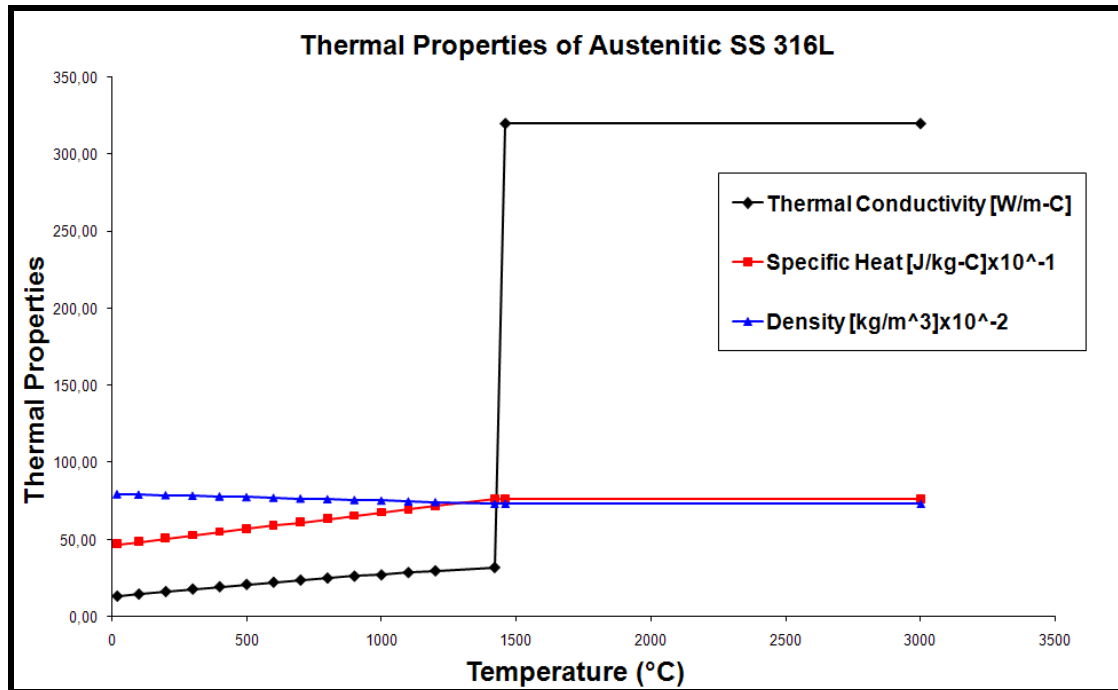
Figure 4.17 Thermal properties of stainless steel 316L [4]

In order to simulate the thermal interaction with the environment, a combined film coefficient, applied to all the free surfaces of the model, was used. The combined film coefficient compromises the heat convention and radiation of the material to the environment. The ambient temperature is considered to be 25 °C.
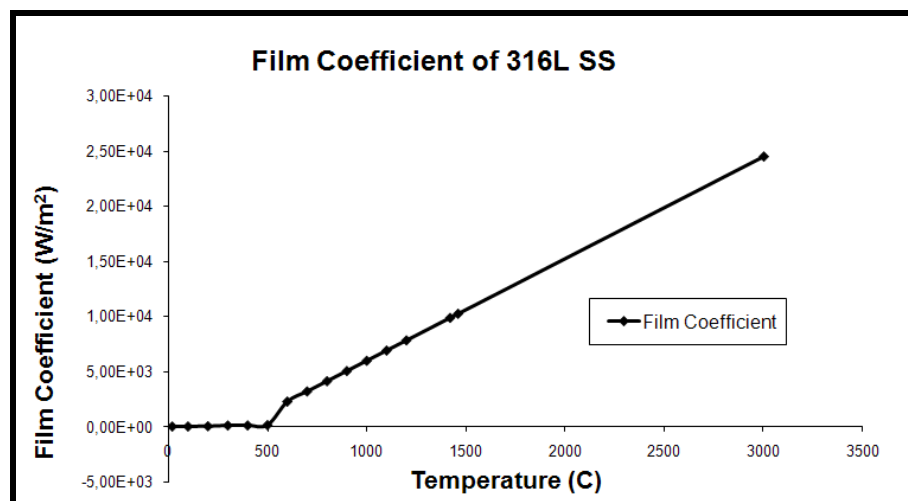
Figure 4.18 Combined film coefficient of 316L stainless steel [5]

4.2.3 Heat Source employment – Birth and Death module

The moving heat source was simulated based on the heat of the molten metal droplets. The heat flux of the molten metal was derived from the heat input equation for arc welding process (Equation 4.1).

$$\dot{Q}_w = \frac{\eta \cdot V \cdot I}{u}[J/m] \qquad [4.1]$$

Respecting the arc voltage, welding current, welding speed and the arc efficiency, varying from 0.6 to 0.9, a volumetric heat source model (Figure 4.19) was employed, simulating the metal addition and the heat input.
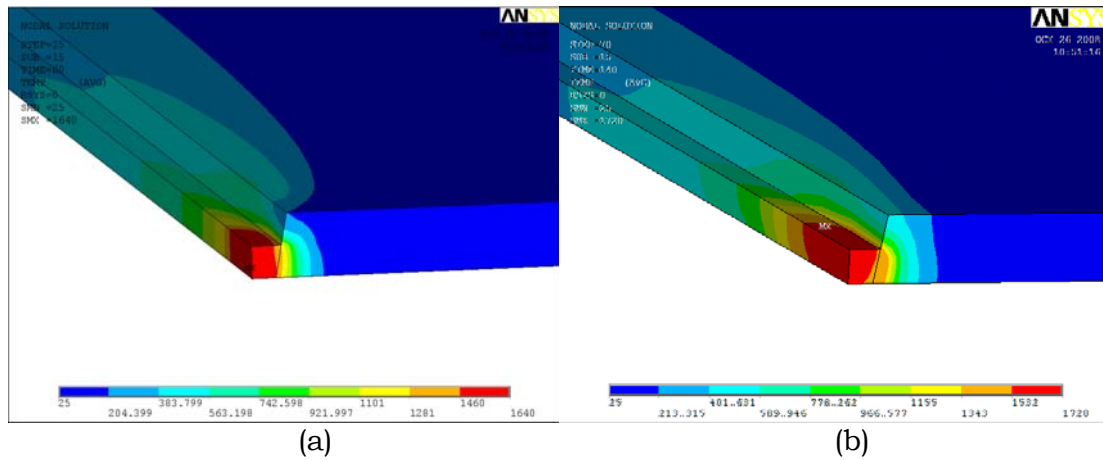
Figure 4.19 Moving heat source at the end of 1st pass a) Model-A b) Model-B [half section view]

The movement of the volumetric heat source model was based on the arc welding speed. The welding speed was 300 mm/min, thus the welding pass time for model-A was 70 sec and for model-B 140 sec. In order to capture the transient phenomenon of welding, a time-stepped transient analysis was carried out. A user subroutine was written to employ the heat load of the heat source in each step, resulting in the accurate representation of the welding procedure (Figure 4.20).
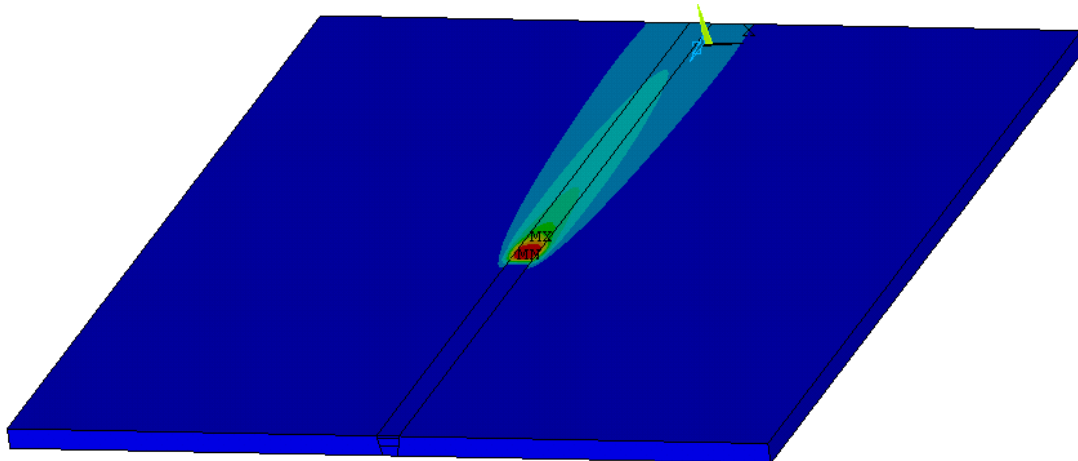
Figure 4.20 The moving heat source in model-A

105

The filler metal addition was simulated with the application of the "Element of Birth and Death" module. This module allows the user to "kill" and "live" several elements at each time step of an analysis. The application of this module does not mean that elements are deleted or created during an analysis; instead they become "inactive" or "active" through this module. The activation and deactivation of elements is done with the introduction of a "stiffness" coefficient, which has a value below 10^{-6} during deactivation and multiplies the stiffness matrix of the elements. Thus, the properties of those elements are practically neutralized and are not affecting the calculations during the solution.

In the present analysis of both models, initially, all elements that belong in the weld metal are "killed" (Figure 4.21), except from those representing the tack welds, which hold the two plates together.
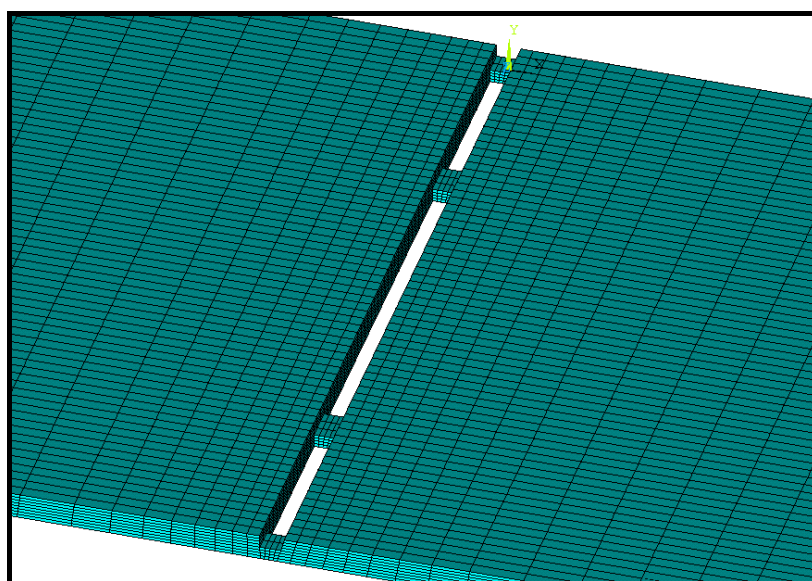
Figure 4.21 "Killed" elements in the weld metal region

The stepped "birth" of elements was performed along with the heat source movement, resulting in the complete activation of all elements by the end of the 3rd weld pass.

There are several remarks concerning the "birth and death" module, which is available not only in the ANSYS® environment but also in other FE programs, like ABAQUS®. Although the existence of this module makes the simulation of filler metal addition possible, the "birth and death" application in multi-pass welding lacks in accuracy in comparison with single-pass welding. This is because the "absence" of the "killed" weld metal from a subsequent weld-pass does not allow the top surface of the just deposited weld pass to interact with the environment. The "deactivated" elements of a subsequent weld pass may not respond to conduction, but they are an existing obstacle between the active weld pass and the environment. During single pass welding simulation this problem does not exist, because there are no previous or subsequent weld passes to deprive the interaction of the just deposited weld pass with the environment.

4.2.4 Structural Analysis

At the end of the thermal analysis, all nodal results, for every time-step, were written in the result file. The result file represents the temperature history of the model and it can be used from the structural analysis as the input load.

The structural analysis in coupled field simulations is dependent on the precedent thermal analysis. However, several important steps must be followed, in order to achieve a correct analysis:

1. The structural analysis adopts the same geometry and mesh from the thermal analysis, in order to obtain geometrical compatibility.
2. The element type used in thermal analysis must be changed to a corresponding element type for the structural analysis.
3. The input of mechanical temperature dependent properties and the optional deletion of the thermal properties, in order to discharge the solver from useless information.
4. The transient structural analysis must be identical with the transient thermal analysis, meaning that the exact number of time steps and time intervals must be used in order to avoid confusion and erroneous results.
5. For each time step of the structural analysis, the load is read and inputted from the thermal result file.
6. The elements that were "killed" and "birthed" in the thermal analysis must undergo the exact same procedure in the structural analysis.

The element type used in the current structural analysis is the ANSYS® SOLID185 element, while the mechanical properties of the material are presented in Figure 4.22 and the Stress-Strain curves in Figure 4.23.
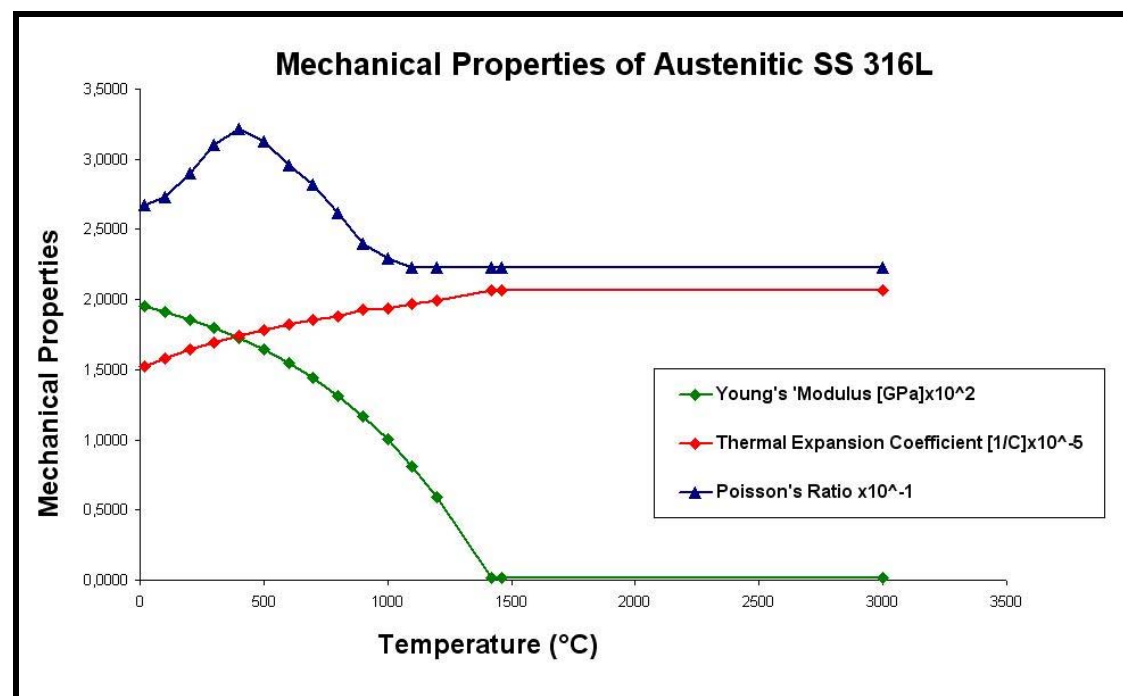

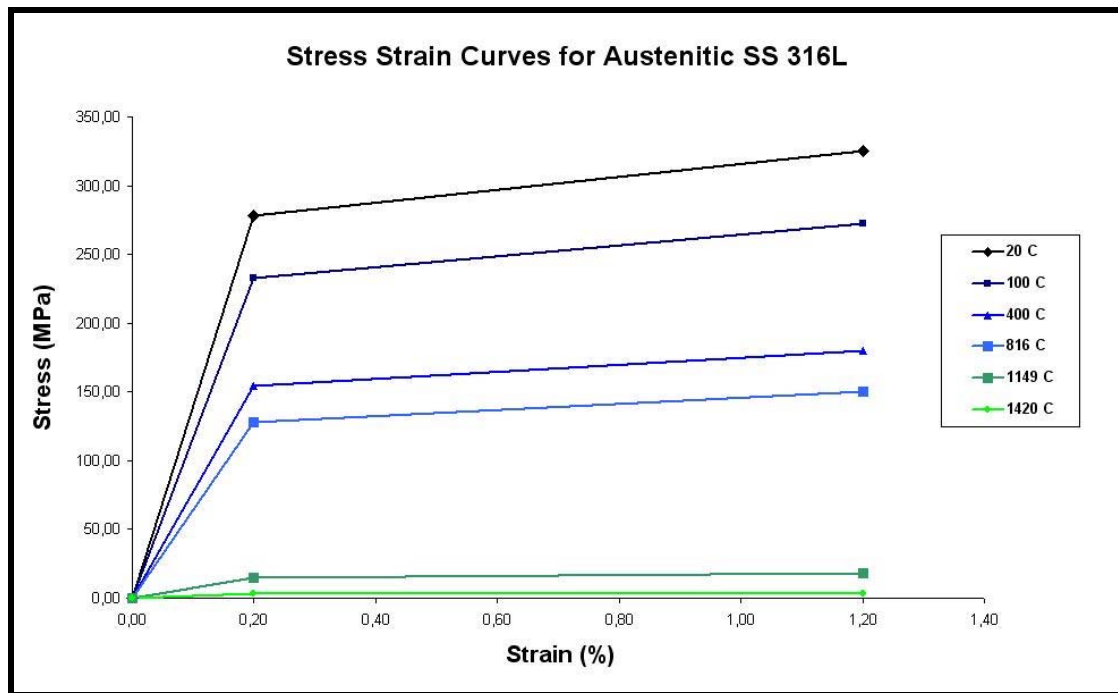**Figure 4.22** Mechanical properties of stainless steel 316L [4]

Figure 4.23 Stress-strain curves of stainless steel 316L [4]

4.3 Thermal Analysis results

During the thermal analysis and at each weld pass, the weld metal temperature was above the melting temperature of the material, as shown in Figure 4.24.
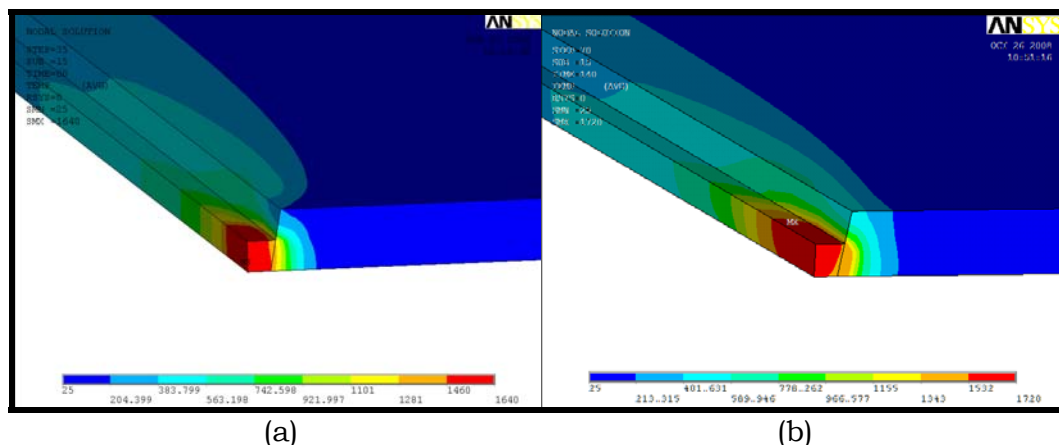

(a)   (b)

Figure 4.24 Temperature distribution of weld metal area at the end of 1st weld pass in a) model-A and b) model-B [half section view]

In order to compare the finite element analysis results with the experimental results, the nodal temperature results, of the node with the same coordinates as the ones of the 1st thermocouple, were used. In Figure 4.25 the finite element temperature results are plotted for node 9684 of model-A as a function of time, presenting the thermal cycle. While, in Figure 4.26 the temperature results of node 10077 of model-B as a function of time are presented.
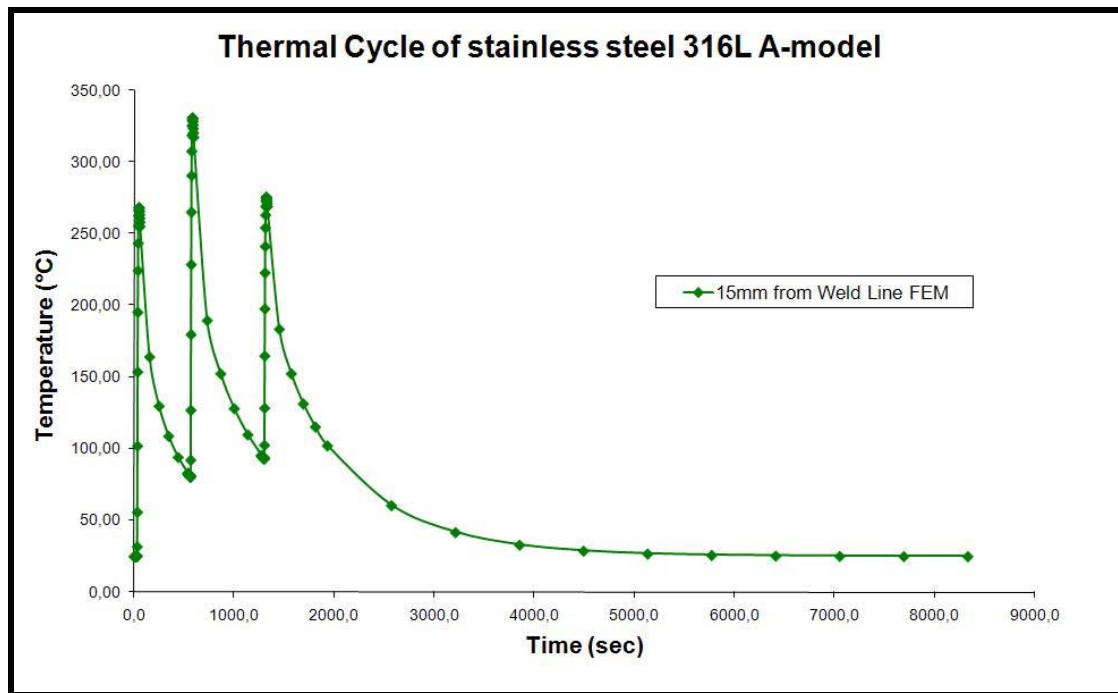
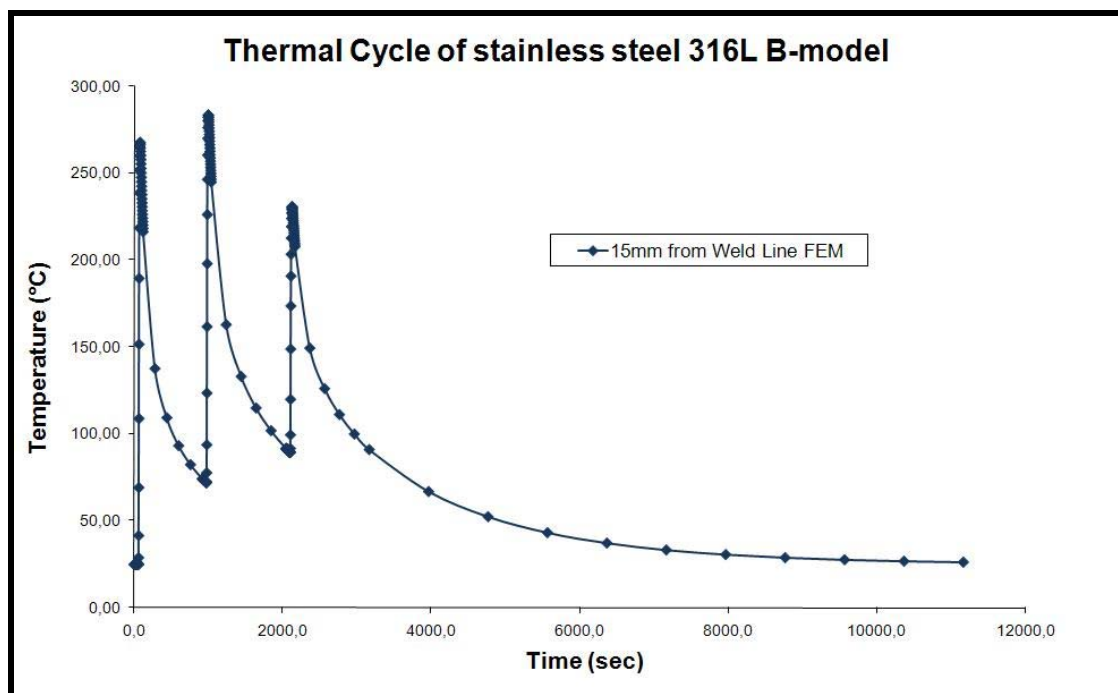**Figure 4.25** Nodal thermal cycle FE results o model-A

Figure 4.26 Nodal thermal cycle FE results o model-B

Comparing the above two figures, it can be noted that model-A exhibits higher temperatures and cooling rates than model-B, which is also exactly the case in the experimental results. This means that the essence of the thermal cycle behavior has been captured successfully. A comparison of both models with their corresponding experimental models would clear the degree of accuracy of the FE results.

4.4 Structural Analysis results

Though there are no experimental results to compare with the FE structural analysis of model-A, the presentation of the residual stresses and deformation of model-A can lead to some useful remarks. In Figure 4.26 the residual stress field and in Figure 4.27 the deformation of model-A are presented.
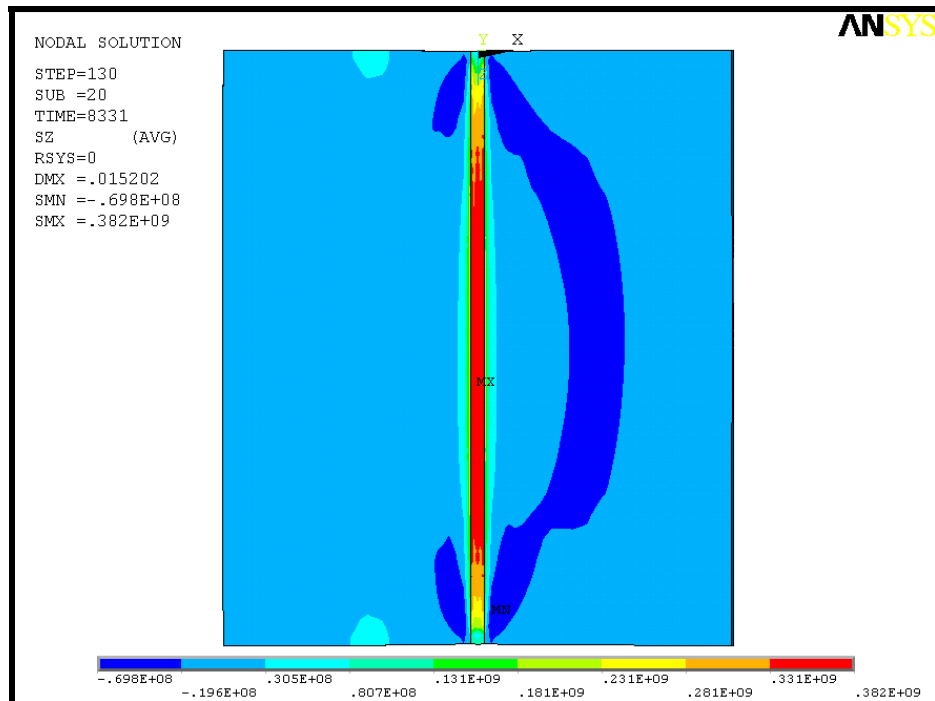

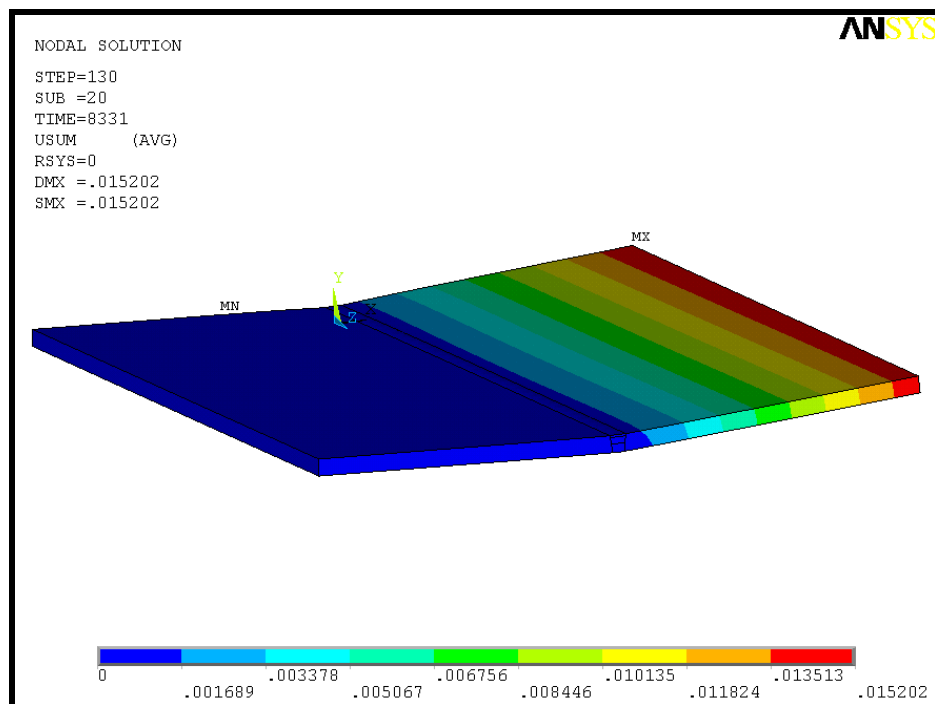**Figure 4.26** Residual stress field of model-A [top view]

Figure 4.27 Deformation of unconstrained plate of model-A

The residual stress field, presented in Figure 4.26, is similar to the one described during the presentation of the experimental results of model-B. High tensile stresses are present in the weld metal region and as the distance from the weld line increases they transform into compressive stresses. However, due to the different dimensions no result comparisons can be made. The deformation behavior of the unconstrained plate, in Figure 4.27, shows the lift-up of the plate and the angular change that was expected.

Similar to model-A, the FE results of model-B are presented in Figures 4.28 and 4.29.
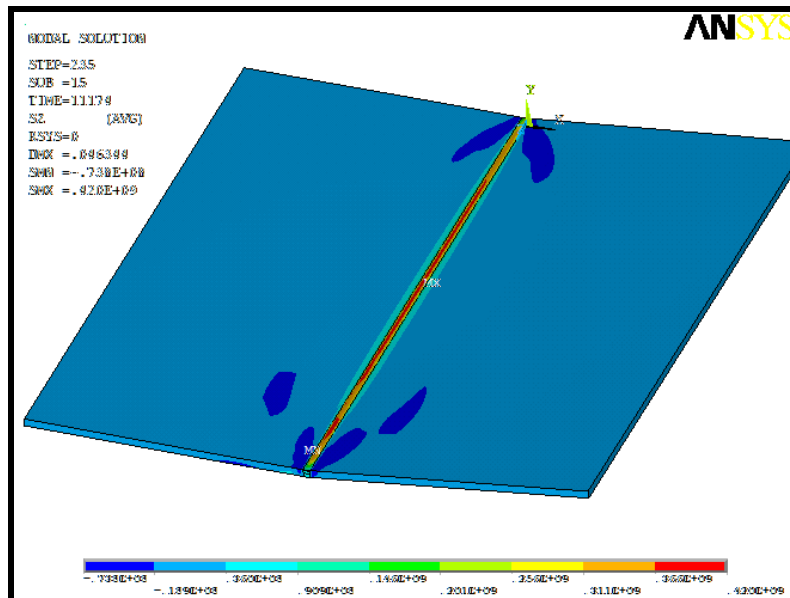

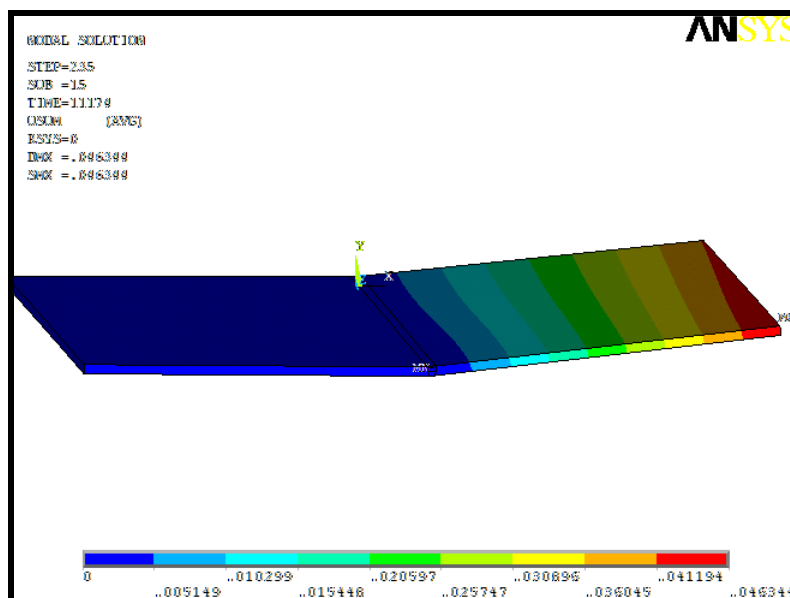**Figure 4.28** Residual stress field of model-B

Figure 4.29 Deformation of unconstrained plate of model-B

The angular change of model-B and the deformation of the unconstrained plate are similar to those of model-A, while the residual

stress field of model-B seems to be more homogenous than the one of model-A. However, high tensile stresses are present in the weld metal region and compressive stresses away from the weld line. The length of the plate has not allowed the existence of compressive iso-stress areas to connect the two ends of the weld line, as it occurred in model-A.

4.5 Comparison of FE Numerical and Experimental results

During the experimental procedure, thermocouples were attached to the stainless steels plates, in order to measure the welding thermal cycle. The measurements from the thermocouple, which was positioned at a distance of 15 mm from the weld line in both series of experiments, were selected to be compared with the FE results from models A and B. In Figure 4.30 the comparison of the measured and the modeled thermal cycle of model-A is presented.
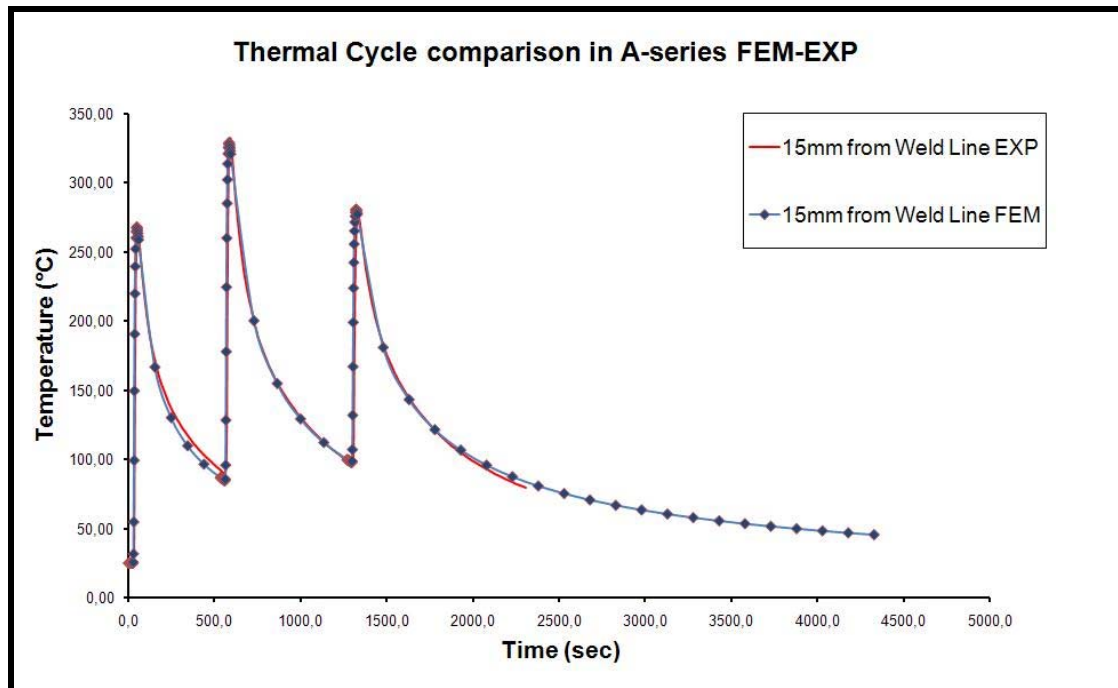

Figure 4.30 Comparison of thermal cycle's experimental and numerical results for model-A

It can be seen, that the experimental and FE results are in excellent agreement, exhibiting the same maximum temperatures at each welding pass and almost identical cooling rates.

In the case of model- and experimental series-B the comparison of the modeled and measured thermal cycle is presented in Figure 4.31.
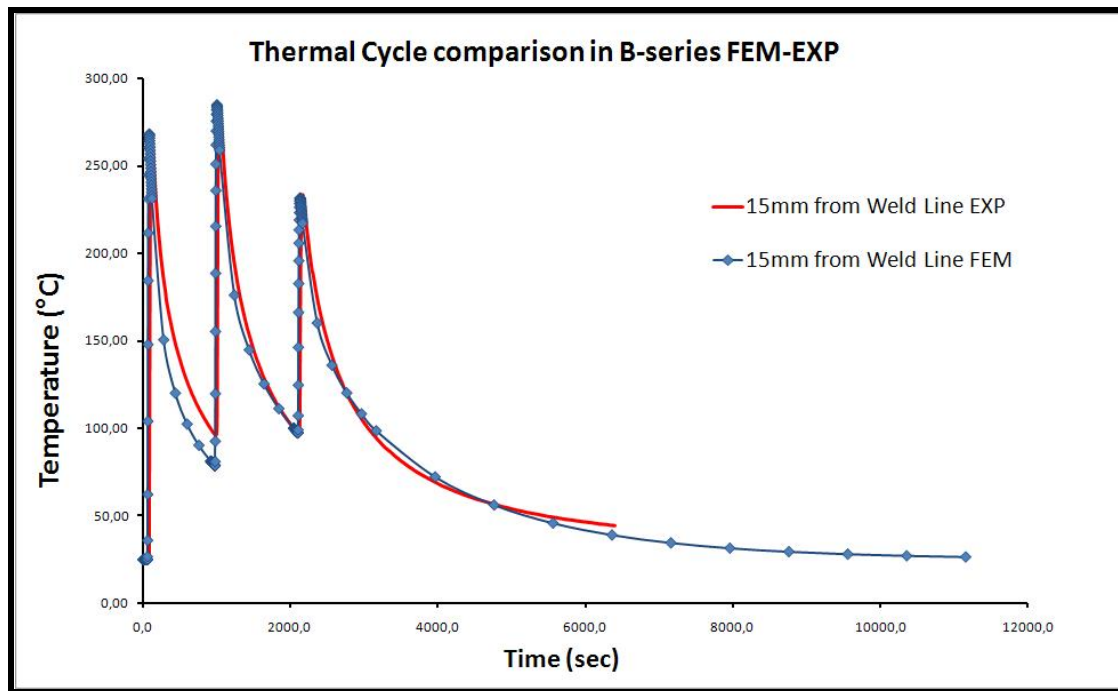
Figure 4.31 Comparison of thermal cycle's experimental and numerical results for model-B

The experimental and numerical results, of the B case, are in good agreement. The high weld pass temperatures are identical, while the cooling rates exhibit a negligible difference, which was not present in case A. The difference, observed mostly during the cooling of the 1st weld pass, can be attributed to the behavior of the "birth and death" module, which was discussed in a previous paragraph. However, the two curves, despite the small difference, are in good agreement with each other. In this case, the structural analysis results followed will be compared with the experimental results and if any difference exists it shall not be attributed to the thermal analysis preceded. Possible factors that may affect the structural analysis results may be the geometry of the model, especially that of the weld metal, the material properties and the thickness of the mesh.

The comparisons of the residual stress field and the vertical deformation results of the welded joint follow. The experimental measurements with the hole-drilling method were conducted on the unconstrained plate, in an area adjacent to the weld line covering a 100 mm width. The residual stress numerical results are presented on the entire width of the welded joint. Regarding the vertical deformation, resulting from the angular change during welding, the measurements of the LVDT-D were chosen to be compared with the numerical results of node 1294, which has the same coordinates with the LVDT's position. Figure 4.32 presents the comparison of the residual stress field between experimental and numerical results, while in Figure 4.33 the comparison of the vertical deformation is shown.
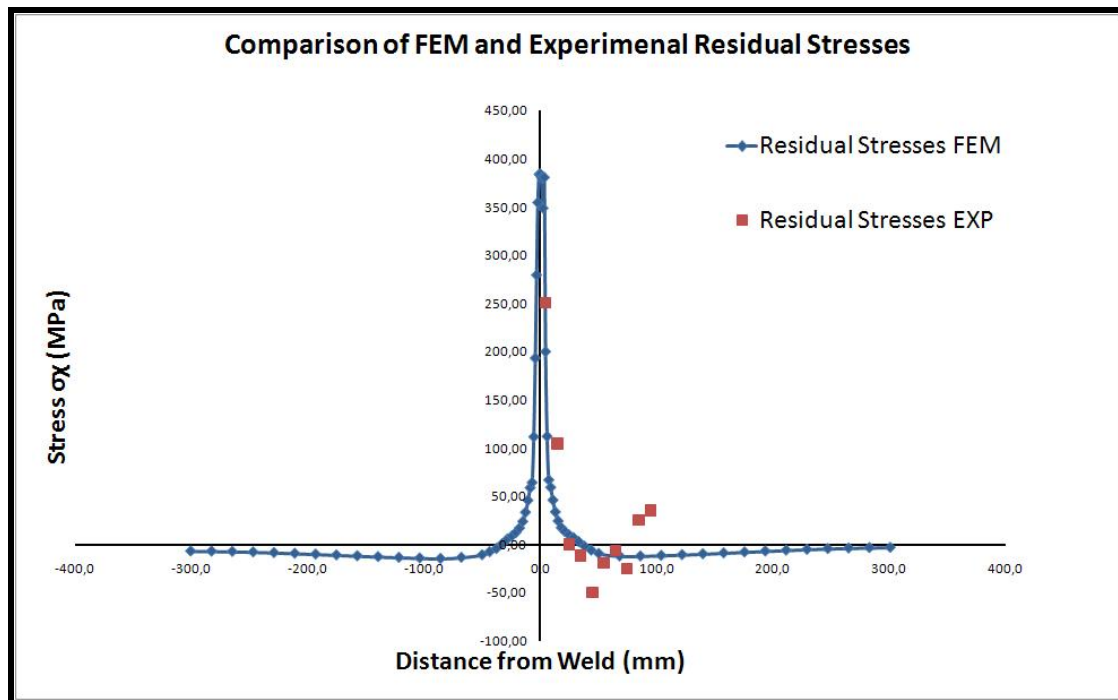
Figure 4.32 Comparison of residual stress field experimental and numerical results for model-B

A good agreement exists, in Figure 4.32, between measured and predicted residual stresses, mostly near the weld area. As the distance from the weld area increases, deviation is observed. This can be attributed to the stress condition of the plates prior to welding. The austenitic stainless steel plates are produced and delivered in the solution annealed condition, but have undergone during manufacturing many treatments, such as thermal rolling, which metallographically can be detected. The existence of residual stresses prior to welding, as discussed in the previous chapter, is a possible explanation to the presence of tensile stresses in that region. In the adjacent to the weld metal region, the high temperature, due to welding, lead to the elimination of any stresses and to the creation of a high tensile stress field. The FE prediction model considers a complete tension-free material prior to the analysis and produces the "ideal" residual stress field as a result.

However, the comparison of the experimental and numerical results is considered to be in good agreement, which indicates the accuracy of the prediction model.

In Figure 4.33, the vertical deformation curves of the LVDT and the numerical model, though not showing any proportionality, share the same characteristics and convergence. Both curves exhibit high deformation rates during a weld pass deposition, while their convergence difference is about 5%. The final deformation measured was approximately 35 mm, while the predicted, by the model, final deformation was 37 mm. During cooling the numerical model shows negligible deformation rates, which can be attributed to the poor number of steps that describe it.
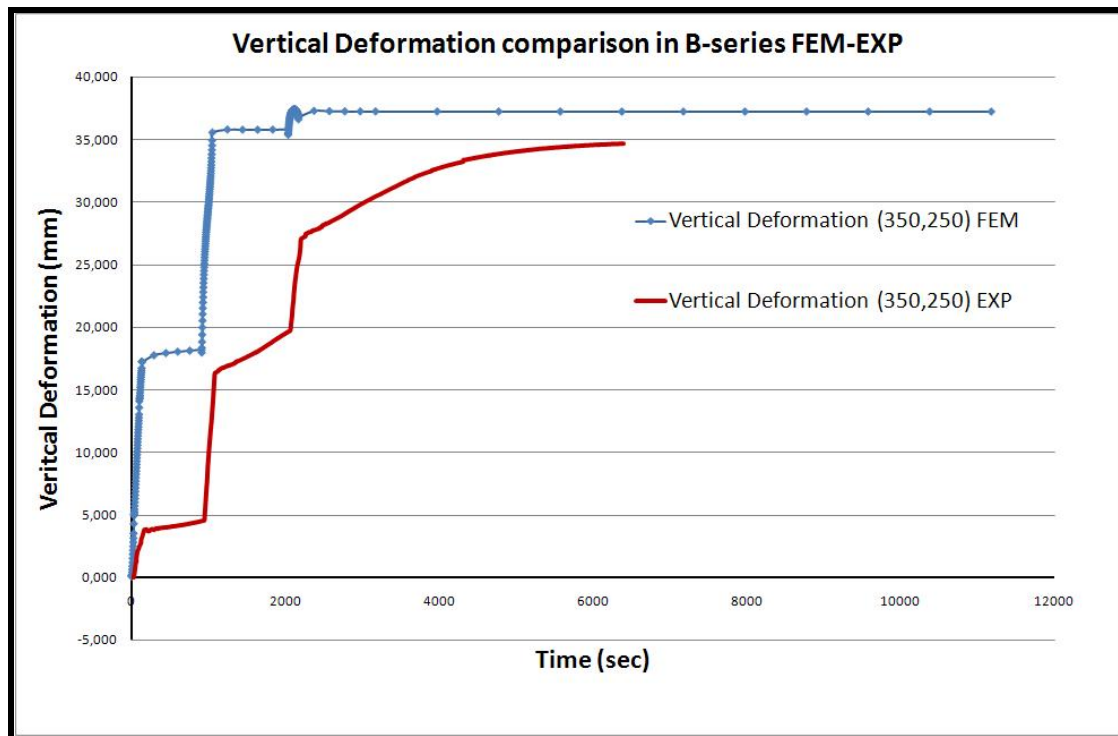
Figure 4.33 Comparison of vertical deformation of experimental and numerical results for model-B

The non-convergence of the two curves during the welding process is attributed to the model geometry of the weld metal. The geometry of the weld metal in the model is simulated with a trapezoidal shape, a departure from the actual complex shape of the multi-pass weld metal. The modeling of an accurate and complex shape of the weld metal would be intruding, but would cost on CPU-time, during the thermal load application. However, with the prediction of the final deformation varying from the experimental measurement only about 5%, the model accuracy is considered successful.

Chapter Bibliography

1. G. D. Papadopoulou, 2007, *"Μελέτη συγκολλήσεων τόξου ανοξείδωτων ωστενιτικών χαλύβων (τύπου 316L)"*, Μεταπτυχιακή εργασία στα πλαίσια του Δ.Π.Μ.Σ. «Επιστήμη και Τεχνολογία των Υλικών»
2. D. Kalaitzoglou, 2008, *"Μελέτη συγκολλήσεων τόξου με παραγεμισμένα ηλεκτρόδια ανοξείδωτων ωστενιτικών χαλύβων τύπου 316L"*, Διπλωματική εργασία Σχολής Ναυπηγών Μηχανολόγων Μηχανικών του ΕΜΠ – in Press
3. V. J. Papazoglou, G. Papademetriou, 1994, *Welding Science and Technology (in Greek)*, Publications of NTUA
4. P. Dong, 2001, *Residual stresses analyses of a multi-pass girth weld: 3-D special shell versus axisymetric models*, Journal of Pressure Vessels Technology Vol.123, pp. 207-213
5. Dean Deng, Hidekazu Murakawa, 2006, *Numerical simulation of temperature field and residual stress in multi-pass in stainless steel pipe and comparison with experimental measurements*, Computational Material Science Vol.37, pp. 269-277

5th Chapter

Conclusions and Future Work

5. Conclusions and Future Work

Two series of experimental multi-pass butt welds of austenitic stainless steels 316L were conducted in the Shipbuilding Technology laboratory of the School of Naval Architecture and Marine Engineering at the National Technical University of Athens. The welding process used was the Flux Cored Arc Welding (FCAW) method. The austenitic stainless steel plates were 8 mm thick. The two series varied in the plate's length and width dimensions. Series A plates were 350x150 mm², while series B were 700x300 mm². The butt welding of both series was made with three welding passes.

For each of the experimental welding series, a finite element numerical model was built, in order to model the thermal cycle of the welding procedure and predict the resulting residual stresses and deformation. The models were built and solved with the finite element program ANSYS®.

For both models 3D transient thermo-mechanical analyses were carried out. A volumetric heat source model, along with the module of "element birth and death", was employed to simulate the filler metal addition and the arc heat input. The thermal results from the thermal analyses were used as input to the structural analyses.

The thermal cycles and the results of the structural analyses were compared with the experimental measurement of each series. In both cases the thermal cycles measured and modeled were in excellent agreement, exhibiting a minor deflection of the cooling rates in the case of model-B. The specific deflection is attributed to the module of "birth and death", which cannot handle entirely correctly the case of multi-pass welding.

The structural analysis results were available for comparison only in case B, because no residual stress and deformation measurements were conducted for the A-series plates. The measured and predicted residual stress fields were in good agreement, mostly in the area adjacent to the weld. Far from the weld experimental measurements showed the presence of tensile stresses, which existed probably prior to welding from the manufacturing process of the plates. The model was unable to predict such stresses, because it considers a stress-less material at the beginning of the simulation.

The vertical deformation, due to angular change, was evaluated. The measured, with LVDTs, of the final deformation varied from the model prediction by approximately 5%. However, the continuous deformation curves could not match. A major factor for this was the weld metal model geometry, which had a plane trapezoidal shape and not the actual complex weld metal shape. If a complex weld metal shape was used in the simulation, the time-to-solution would increase dramatically.

The model predictions are considered to be quite accurate and solutions can be reached in a reasonable time period. The simulation of a single-pass welding procedure is recommended for future work, in

order to achieve a better evaluation of the "birth and death" module. Simultaneously, a 2D analysis with a more complex and geometrically accurate shape can be attempted to study the effect of geometry on the plate behavior during welding.

Based on the above proposals, two series of experiments are going to be carried out in the Shipbuilding Technology laboratory in the near future. The first series concerns the single-pass butt welding of austenitic stainless steel, 4 mm thick, plates, while the second series deals with the multi-pass butt welding of austenitic stainless steel, 12 mm thick, plates. Based on both series, several simulation models, in the ANSYS® environment, are going to be built. Regarding the single-pass welding experiment and model, the evaluation of the "birth and death" module shall be discussed, as proposed. The multi-pass butt welding of 12 mm thick stainless steel plates shall be simulated in several ways to ensure the decrease of the time-to-solution, without any loss of accuracy.